

ABSTRACT

HUANG, LIANGLIANG. Computational Study of Toxic Gas Removal by Reactive Adsorption. (Under the direction of Professor Keith E. Gubbins).

Growing concerns about the environment and terrorist attacks prompt a search for effective adsorbents for removal of small molecule toxic gases, such as ammonia and hydrogen sulfide, under ambient conditions in the presence of moisture, where physical adsorption is not adequate. We use graphene oxide and CuBTC metal-organic framework as the adsorbents to explore toxic gas removal by reactive adsorption. Using *ab initio* density functional theory, atomistic reactive molecular dynamics and Monte Carlo simulation strategies, theoretical understanding of the underlying reaction and adsorption mechanisms of ammonia and hydrogen sulfide on graphene oxide and CuBTC metal-organic framework have been gained.

The *ab initio* calculation results show that ammonia and hydrogen sulfide decompose on carboxyl and epoxy functional groups and vacancy defects of graphene oxide. The existence of water molecules substantially reduces the adsorption/dissociation of ammonia or hydrogen sulfide on graphene oxide because the water molecules either form hydrogen bonds with the functional groups or adsorb more easily on the vacancy defects. Reactive molecular dynamics calculations by the ReaxFF method have been performed to propose realistic graphene oxide models for theoretical calculations. We also use reactive molecular dynamics simulation to study the thermal and hydrostatic stabilities of the CuBTC metal-organic framework and its application for ammonia removal. We predict the collapse temperature for

CuBTC crystal structure and observe the partial collapse of CuBTC at lower temperatures upon ammonia adsorption. The results agree well with experiment data and provide insights on the reaction mechanism involved in such an ammonia removal process.

The research in this thesis can provide fundamental understanding, at the electronic and atomistic levels, of the roles of surface defects and functionalities for reactive adsorption of toxic gas molecules. In addition to developing experimental and theoretical algorithms to design effective adsorbents, the results are expected to find applications in air cleaning, energy storage, fuel cell technology and other scientific challenges where the separation of reactive molecules is involved.

© Copyright 2012 by Liangliang Huang

All Rights Reserved

Computational Study of Toxic Gas Removal by Reactive Adsorption

by
Liangliang Huang

A dissertation submitted to the Graduate Faculty of
North Carolina State University
in partial fulfillment of the
requirements for the degree of
Doctor of Philosophy

Chemical Engineering

Raleigh, North Carolina

2012

APPROVED BY:

Keith E. Gubbins
Committee Chair

Carol K. Hall

Phillip R. Westmoreland
Committee Co-Chair

Donald W. Brenner

DEDICATION

To my beloved daughters Grace, Emmy and my beautiful wife Peng.

BIOGRAPHY

Liangliang Huang

DOB: May 9th, 1981.

Address: 3113B, Kings court, Raleigh, NC, 27606.

Contact Information: (919) 744 6282, lhuang4@ncsu.edu

Education:

B.Sc. Chemical Engineering (major), Computer Science (minor), Nanjing University of Technology, Nanjing, China, 2003.

M.Sc. Chemical Engineering, Nanjing University of Technology, Nanjing, China, 2007.

Thesis title: The investigation of confined fluids in carbon nanotubes by computer simulations.

Work & Research experience:

Internship, BASF-YPC Company Limited, Jiangsu, China, March ~ April 2003.

- Learn the state-of-the-art technologies and BASF's concept to maintain cost efficiency and minimize environmental impact.

Research Assistant, Nanjing University of Technology, China, September 2003 ~ July 2007.

- Work in Professor Xiaohua Lu group;
- Research topics: the behavior of confined water, ethanol and ionic liquids, the adsorption and separation of methane/carbon dioxide mixtures;
- Collaborate with industrial partners to optimize the thermodynamic conditions for titanium oxide synthesis; to seek a fundamental understanding of the surface functionalization for membrane separation process; propose possible models for carbon dioxide geological sequestration;

Visiting Researcher, California Institute of Technology, Pasadena, California, January 2011.

- Work in Professor William A. Goddard III group;
- Learn ReaxFF method, and develop new parameters for ammonia;

Visiting Researcher, Pennsylvania State University, University Park, Pennsylvania, March 2011.

- Work in Professor Adri van Duin group;
- Re-train ReaxFF parameters for CuBTC, NH₃/CuBTC, H₂O/NH₃/CuBTC systems;

Research Assistant, North Carolina State University, Raleigh, NC, August 2007 ~ Present.

- Work in Professor Keith E. Gubbins group;
- Build theoretical models of amorphous carbon materials, carbon/metal organic framework nano-composites, and other surface structures that are of general interest to adsorption, diffusion and chemical reaction;
- Collaborate with experimental scientists to design materials for toxic gas removal and optimize the experimental conditions of temperature, pressure and concentration;
- Train other students in the group to use computational softwares;

Teaching Assistant, North Carolina State University, Raleigh, NC, August 2007 ~ Present.

Graduate Course: Multi-Scale Modeling of Matter (Spring 2012)

Graduate Course: Advanced Thermodynamics (Fall 2008 ~ 2011)

Undergraduate Course: Thermodynamics of Chemical and Phase Equilibria (2008, 2010)

Undergraduate Course: Chemical Process Thermodynamics (Spring 2009, Fall 2007)

- Help to prepare lecture notes, home work assignments, quiz and exam problems;
- Deliver classes and exam review lectures when the instructor is out of town;
- Hold office hours to clarify course concepts and assist on homework assignments;
- Grade homework assignments, quizzes and exams, and maintain the course website.

ACKNOWLEDGMENTS

I would like to express my deepest appreciation to Professor Keith E. Gubbins for his supervision, guidance and support for the past five years at NC State University. His insights and constant encouragement to pursue creative ideas and fundamental understandings have made my doctoral study an enjoyable experience. I am very grateful to his kindness and support to my professional career development. He always encourages me to attend conferences, meetings, and workshops in our research field, and creates opportunities for me to visit other research groups in pursuing my scientific interest. I have been also benefiting from the teaching assistant experience with Keith. I am deeply touched by his enthusiasm and carefulness in teaching. I am a leaf of his academic tree, and continue to grow under his guidance.

I would also like to thank my committee members, Professor Carlo K. Hall, Professor Phillip R. Westmoreland and Professor Donald W. Brenner for their patience and insightful comments on the examinations and my research projects.

Many thanks go to Professor William A Goddard III at California Institute of Technology and his group members, Dr. Andres Jaramillo-Botero, Dr. Jonathan E. Mueller, Qi An, Hai Xiao, Lianchi Liu and Tingting Zhou. I have enjoyed my two-week stay at Caltech in January 2011, and have learnt a lot about ReaxFF method.

I am grateful to Professor Adri C.T. van Duin at Pennsylvania State University and his group members Dr. Kaushik L. Joshi, Dr. Michael F. Russo Jr., and Sriram G. Srinivasan for sharing ReaxFF parameters and scripts, and the collaborations with me for my research projects.

I want to thank Professor Teresa J. Bandosz at The City College of New York for the collaborative project and her encouragement and help on my manuscripts. I also want to

thank Professor Małgorzata M. Śliwinska-Bartkowiak for introducing the exciting experimental results of molecules under confinement and the publications we have put together. The encouragement from Professor Xiaohua Lu and Professor Xin Feng at Nanjing University of Technology, China, is greatly appreciated.

I thank past and present members of the Gubbins group: Dr. Erik Santiso and Dr. Liping Huang for Density Functional Theory method; Dr. Joshua D. Moore for molecular dynamics simulation, especially the mean square displacement calculation, Linux shell scripts, supercomputer usage and many others; Dr. Jeremy C. Palmer for Monte Carlo method, the adsorption isotherm calculation, and the discussion for surface functionalization; Katherine A. Phillips, Yun Long and Cody K. Addington for interesting discussions.

I want to thank June McKoy, Sandra Bailey, Diane Harper, Saundra Doby and other staff at CBE for supporting and helping, and making my stay at NC State University a pleasant and comfortable one.

Finally, I want to thank my parents and my parents-in-law for their unconditional support. I love you!

The work presented in this thesis is supported by grants from the National Science Foundation (Grant No. CBET-0754979, CBET-1133066 and CHE-1012780). I am grateful for grants of supercomputer time through Teragrid resources provided under NSF grant number TG-CHE080046N, and the Office of Information Technology at NC State University for the High Performance Computing services.

TABLE OF CONTENTS

LIST OF TABLES	x
LIST OF FIGURES	xii
CHAPTER 1	1
Introduction.....	1
1.1. Toxic Gas Removal.....	1
1.2. Ammonia and Hydrogen Sulfide	2
1.3. The Removal of Ammonia and Hydrogen Sulfide	3
1.4. Graphene, Graphite Oxide and Metal-Organic Framework	5
1.5. Research Approach	8
CHAPTER 2	10
Computational Methods.....	10
2.1. Density Functional Theory	10
2.2. Reactive Force Field Method.....	16
2.3. Classical Atomistic Molecular Modeling	20
CHAPTER 3	24
Adsorption and Dissociation of Hydrogen Sulfide on Graphene Single Vacancy	24
3.1. Introduction.....	24
3.2. The sv-graphene Model and Computational Method	26
3.3. Results and Discussion	30
3.4. Conclusions.....	45
CHAPTER 4	48
Adsorption and Dissociation of Ammonia on Graphite Oxide.....	48
4.1. Introduction.....	48
4.2. The GO Model and Computational Method	53
4.3. Results and Discussion	55
4.4. Conclusions.....	65
CHAPTER 5	67

Realistic Graphene Oxide Models by Reactive Molecular Dynamics Simulations	67
5.1. Introduction.....	67
5.2. Computational Details	69
5.3. Results and Discussion	73
5.4. Conclusions.....	83
CHAPTER 6	84
Thermal Stability of CuBTC MOF: Reactive Molecular Dynamics Simulations	84
6.1. Introduction.....	84
6.2. Computational Details	86
6.3. Results and Discussion	88
6.4. Conclusions.....	99
CHAPTER 7	101
Ammonia Adsorption on CuBTC: Molecular Simulation and Experimental Study	101
7.1. Introduction.....	101
7.2. Molecular Modeling and Experimental Setup	103
7.3. Results and Discussion	108
7.4. Conclusions.....	114
CHAPTER 8	116
Reactive Adsorption of Ammonia on CuBTC: a ReaxFF Molecular Dynamics Simulation	116
8.1. Introduction.....	116
8.2. Computational Methods.....	118
8.3. Results and Discussion	122
8.4. Conclusions.....	133
CHAPTER 9	134
Conclusions and Outlook.....	134
9.1. Conclusions.....	134
9.2. Future research plans	137
REFERENCES	142
APPENDICES	165

APPENDIX A.....	166
Installing the parallel version of LAMMPS package	166
APPENDIX B.....	170
An example of the temperature-programmed RMD by LAMMPS	170
B.1. Control file, “in.reaxff”	170
B.2. A list of ReaxFF parameter explanations	172
B.3. ReaxFF parameters for C, H and O elements of graphene oxide.....	175

LIST OF TABLES

Table 3-1. Typical accuracy for <i>ab initio</i> DFT calculations with BLYP functional.[63].....	30
Table 3-2. The structural properties of H ₂ S, HS and Graphene.....	32
Table 3-3. The optimized structural parameters for the H ₂ S molecule, which is placed initially 2.5 Å from the sv-graphene surface. “D*” represents the optimized distance between the sv-graphene and the atom (in bracket) of the H ₂ S molecule.	34
Table 3-4. The adsorption characteristics of the H ₂ S molecule on the sv-graphene surfaces: adsorption energy (E_{ads}), H ₂ S-Surface distance ($d_{S-Surface}$) and the structural properties of H ₂ S (d_{S-H} for thw two H-S bonds). The calculated structural properties of the gas-phase, H ₂ S (g), are provided for reference. The H ₂ S molecule is placed initially 2.5 Å from the sv-graphene surface. The distance is measured between the lowest atom of H ₂ S and the surface.	35
Table 3-5. H ₂ S adsorption on different surfaces: the optimized H ₂ S-Surface distance, adsorption site and the adsorption energy.....	36
Table 3-6. The optimized structural parameters for the H ₂ S molecule, which is placed initially 1.5 Å from the sv-graphene surface. “D*” represents the optimized distance between the sv-graphene and the atom (in bracket) of the H ₂ S molecule.	37
Table 4-1. 14 investigated GO models. “COOH”, “OH”, “SO ₃ H”, “H” and “C” stand for carboxyl, hydroxyl, sulfonic groups, hydrogen atoms used to saturate the functionalized benzene hexagon, and the carbon atoms on which the epoxy groups are formed.	56
Table 4-2. The hydrogen bond information between the H ₂ O molecule and the functional groups: “O _{HC} ”, “O _C ”, “O _H ” represent the oxygen atom from carboxyl single-bonded oxygen, carboxyl double-bonded oxygen and hydroxyl oxygen, respectively. “HB” stands for the existence of hydrogen bond.....	58
Table 5-1. A summary of the 12 systems with the number of molecules.....	80
Table 7-1. The Lennard-Jones parameters: σ - the finite distance at which the interparticle potential equals zero, ϵ - the minimum potential, and atomic charges of atoms for	

CuBTC and NH ₃ (q). M is a pseudo site of the 5-site NH ₃ TraPPE model, where the negative charge is placed.	105
Table 7-2. The binding energy (kJ/mol) of NH ₃ on different sites of CuBTC.	109
Table A-1. The parameters in the bond order functions.	172
Table A-2. The parameters in the 1-body energy.	173
Table A-3. The parameters in the E_{bond}	173
Table A-4 The parameters in the 3-body energy.	174
Table A5. The parameters in the 4-body energy.....	174
Table A-6. The parameters in the hydrogen bonding energy.	174
Table A-7. The parameters in the non-covalent energy.....	175
Table A-8. EEM parameters.	175
Table A-9. Bond order parameters.....	175
Table A-10. Bond order correction parameters.	176
Table A-11. Bond energy parameters.	176
Table A-12. Lone pair energy parameters.	176
Table A-13. Overcoordination parameters.	176
Table A-14. Undercoordination parameters.	177
Table A-15. Valence angle parameters, part I.	177
Table A-16. Valence angle parameters, part II.	178
Table A-17. Penalty energy and 3-body conjugation parameters.....	179
Table A-18. Torsion angle and 4-body conjugation parameters, part I.	179
Table A-19. Torsion angle and 4-body conjugation parameters, part II.....	180
Table A-20. van der Waals interaction parameters.....	180
Table A-21. Coulomb interaction parameters.....	180
Table A-22. Hydrogen bond parameters.....	180
Table A-23. Taper correction parameters.	181

LIST OF FIGURES

Figure 3.1. The sv-graphene model, created by removing one carbon atom from a 48-carbon rectangle graphene. Three different sites, namely, on top of a carbon atom (T), the center of a carbon hexagon (C), and the center of a carbon-carbon bond (B) have been investigated for possible adsorption and/or dissociation of H ₂ S.	27
Figure 3.2. Four different initial H ₂ S orientations, indexed as V shape, planar shape, vertical shape and Λ shape. D is the adjustable parameter to describe the distance between H ₂ S and the sv-graphene surface.	28
Figure 3.3. The 2-D electron density profile for the sv-graphene surface.	28
Figure 3.4. The dissociation of H ₂ S on the sv-graphene surface: the optimized final structure, corresponding to the two dissociation states in Table (3-6).	38
Figure 3.5. Intermediate states for H ₂ S dissociation on the sv-graphene surface. Rows from left are: intermediate states from Ref.; top view, lateral view and side view of the intermediate states in this work, where (a) is the initial state; (h) is the final state; the S atom occupies the vacancy site on the surface and hydrogen is pushed away from the surface; (b) to (e) are intermediate states corresponding to the ones in Ref.[169]. The formation energy is provided in the last row.	40
Figure 3.6. The reaction energy barrier for H ₂ S dissociation along “a \rightarrow e \rightarrow p” pathway: “Initial”, “IM(e)”, “TS” and “Product” represent the initial state (a), global energy minimum state (e), transition state along the reaction pathway and final state (p), respectively.	43
Figure 3.7. The reaction energy barriers for H ₂ S dissociation reactions along: “a \rightarrow b \rightarrow p”, “a \rightarrow c \rightarrow p”, “a \rightarrow d \rightarrow p”, “a \rightarrow g \rightarrow p” and “a \rightarrow h \rightarrow p” pathways, where “a”, “b”, “c”, “d”, “g” and “h” are corresponding to the stable intermediate states described in Figure 3.5.	44
Figure 3.8. The reaction energy barriers: a comparison for H ₂ S dissociation along different reaction pathways.	45
Figure 3.9. NH ₃ dissociation on the sv-graphene model.	47

Figure 4.1. A summary of several lattice structural GO models: Hofmann (in 1939);[183] Ruess (in 1946);[184] Scholz-Boehm (in 1969);[185] Nakajima-Matsuo (in 1988).[179] Adapted from Ref.[182].....	50
Figure 4.2. Lerf-Klinowski GO models[46]: (top) with carboxylic groups on the basal plane; (bottom) without any carboxylic group on the basal plane.....	51
Figure 4.3. The GO model: C ₁ , C ₂ , C ₃ , and C ₄ are four sites where functional groups are attached. The system is periodic for both X and Y directions.	54
Figure 4.4. The optimized structures for the GO models: (a) Model 3; (b) Model 6; (c) Model 12; (d) Model 13.	57
Figure 4.5. The final configuration for the NH ₃ /GO reaction: (top) NH ₃ with the carboxyl group on Model 3; (middle) NH ₃ with the carboxyl on Model 12; (bottom) NH ₃ with the epoxy group on Model 13. The rows from left to right are the top, side and schematic views of the final configuration.	61
Figure 4.6. Activation energy barrier for the NH ₃ dissociation on: (a) Model 3, GO with the carboxyl group; (b) Model 12, GO with the carboxyl and hydroxyl groups; (c) Model 13, GO with the epoxy group.....	63
Figure 4.7. NH ₃ dissociation on the epoxy group of GO: the reaction mechanism proposed in Ref.[13].....	65
Figure 5.1. The front view (Left) and top view (Right) of a 4.3 nm × 4 nm × 2.5nm simulation box. The initial GO structure 30%-(1:1), where 30% of the basal carbon atoms are functionalized by the hydroxyl and epoxy groups in the ratio of 1:1, is placed in the center of the simulation box. Periodic boundary conditions are applied along X, Y and Z directions.....	71
Figure 5.2. The annealing protocol of GO structure in RMD: “I” and “F” are the initial and final GO configurations, respectively. “A”, “B”, “C” and “D” are the intermediate GO configurations along the path. A time step of 0.25 fs is used throughout the calculations.....	72
Figure 5.3. Configurations of GO structures with the functional groups and local defects: (a), (b) and (c) are the final configurations of GO where 10%, 20% and 30% of the basal carbon atoms are functionalized by the hydroxyl and epoxy groups in the ratio of 1:1,	

respectively. Functional groups and carbon arrangements formed in the configurations of (a): a pair of meta-epoxy groups (a-1), a pair of carbonyls (a-2), an epoxy group (a-3), a hydroxyl group (a-4); (b): a single vacancy and a pair of carbonyls (b-1), a large carbon ring (b-2), an aldehyde group (b-3); (c): a carboxyl group (c-1), a preferential alignment of epoxy groups along the zigzag direction (c-2), a furan (c-3). The color codes are: carbon-grey, oxygen-red, hydrogen-white.....76

Figure 5.4. Population analysis of the GO structures: the number of molecules along the cook-off path (A to B) and high temperature relaxation path (B to C) for different functional group concentrations: 10% (black line); 20% (blue line); 30% (red line). T_r is the temperature when we start to observe the release of reaction products. The black dashed line is the targeted temperature of the RMD calculation.77

Figure 5.5. The population analysis of H₂S chemisorption and dissociation on the 30%-(1:1) GO structure. The color codes are: temperature (K)-red, HS-black, chemisorb H₂S-geen, CO-blue, CO₂-magenta, H₂O-purple. The box contains 100 H₂S molecules at the beginning of the calculation.79

Figure 5.6. Population analysis for H₂S (left axis) and H₂O (right axis) chemisorption on GO structures: (a) 10%-(1:1); (b) 20%-(1:1); (c) 30%-(1:1). For the 10%-(1:1) case, the green and blue lines coincide at $n_{H_2S}=0$82

Figure 6.1. The volume evolution of CuBTC framework at: (a) T=300, 400, 550, and 600 K; (b) T = 565, 570, 580, 590 and 600 K.....90

Figure 6.2. The volume evolution of CuBTC at the investigated high temperatures: T = 600, 700, 800, 900, 1000, and 1100 K.92

Figure 6.3. Structure snapshot of CuBTC framework at 700 K: image (a) and image (b) represent the two configurations at t=75 ps and 110 ps, respectively. Color codes are: yellow-Copper, grey-Carbon, red-Oxygen, and white-Hydrogen.92

(a) T=800 K94

(b) T=1100 K94

Figure 6.4. Population analysis of major species released from CuBTC framework: (a) T= 800 K; (b) T=1100 K.94

Figure 6.5. (a) Typical pairs of Cu dimer in the CuBTC framework. ‘Cu₂’ stands for the Cu dimer. Color codes are: yellow-Copper, grey-Carbon, red-Oxygen, and white-Hydrogen; (b) Cu-Cu , distribution function $g(r)$ and coordination number distribution $n(r)$ of CuBTC framework at 300 K, 700 K and 1100 K. The colored number at each peak represents the distance between the Cu dimers, the ones with the same color as in (a). .97

Figure 6.6. Contour plots of the evolution of the Cu-Cu RDF at (a) 300K; (b) 700K; (c) 1100K. The color scale represents the peak height of the Cu-Cu RDF.99

Figure 7.1. The supercell of CuBTC structure, where A, B, C, D, E correspond to different NH₃ adsorption sites: A - along the Cu-Cu bond; B - close to the benzene ring; C - center of the main channel; D - center of the tetrahedral pore; E - perpendicular to the Cu-Cu bond. The color codes are: blue – copper; red – oxygen; grey - carbon. Hydrogen atoms are not shown for clarity. The lattice is shown in dashed line.104

Figure 7.2. The atomic notations for CuBTC model in the GCMC calculation.106

Figure 7.3. Adsorption isotherms for NH₃ adsorption on CuBTC: the comparison of GCMC results (open points) and experimental data (filled points). Temperatures are 301 K, 318 K and 348 K.112

Figure 7.4. Final configuration of the CuBTC structure with adsorbed NH₃ molecules at copper sites and in the micropores (T = 348 K, P = 120 kPa). The color codes are: dark blue – copper; red – oxygen; grey – carbon; light blue – nitrogen; white - hydrogen...113

Figure 8.1. (a) A comparison of simulated and experimental adsorption isotherms of NH₃ on dehydrated CuBTC framework at 301, 318, and 348 K;[228] (b) A snapshot of the CuBTC framework with 63 NH₃ molecules at 348 K; periodic boundary conditions are applied in the x, y and z directions. Color codes are: yellow-Copper, grey-Carbon, red-Oxygen, white-Hydrogen, and blue-Nitrogen.121

Figure 8.2. (a) A sketch of typical Cu-Cu distances of a CuBTC framework. Right hand figures (b) to (e) show the evolution of Cu-Cu radial distribution function for: (b) a pristine dehydrated CuBTC at 301 K; (c) 12 H₂O in a dehydrated CuBTC at 301 K; (d) 12 H₂O in a dehydrated CuBTC at 389 K; (e) 192 H₂O in a dehydrated CuBTC at 389 K.124

Figure 8.3. Cu-Cu radial distribution function evolution at 348 K: (a) pristine dehydrated CuBTC framework; (b) dehydrated CuBTC framework with 63 NH ₃ molecules.....	125
Figure 8.4. Evolution of radial distribution function for the 63-NH ₃ /CuBTC system at 348 K: (a) O-N; (b) Cu-N.	127
Figure 8.5. Reactive adsorption of NH ₃ on dehydrated CuBTC at 348 K. The distribution of molecules is monitored as a function of simulation time.	128
Figure 8.6. Reactive adsorption of H ₂ O/NH ₃ mixtures on dehydrated CuBTC at 301 K. The distribution of molecules is monitored as a function of simulation time: (a) 24 H ₂ O/120 NH ₃ ; (b) 96 H ₂ O/120 NH ₃ . Arrows are added to guide the reading of numbers in accordance with the axis.	130
Figure 8.7. Evolution of radial distribution functions: (a) Cu-Cu RDF for the 24 H ₂ O/120 NH ₃ /CuBTC system; (b) Cu-Cu RDF for the 96 H ₂ O/120 NH ₃ /CuBTC system; (c) Cu-N RDF for the 24 H ₂ O/120 NH ₃ /CuBTC system; (d) Cu-N RDF for the 96 H ₂ O/120 NH ₃ /CuBTC system.....	132
Figure 9.1. The tree of thesis outline with the color codes: black - the toxic gas investigated; blue - the computational method; red - the chapter number; white - the keyword for the topic.....	134
Figure 9.2. A schematic model for graphite oxide material: gray-carbon, red-oxygen, and white-hydrogen.	138
Figure 9.3. The RMD simulation model to study the interactions between H ₂ S molecules and the graphene with the single vacancy defects (red circles), and Stone-Wales defects (blue rectangles).....	139
Figure 9.4. A schematic model of the GO/CuBTC composite: the contribution for NH ₃ (yellow spheres) adsorption comes from the physisorption in the pores/channels, the chemisorption on the Copper sites of CuBTC, and the reaction with the functional groups of GO. [257].....	140
Figure 9.5. Schematic models for the nanocomposite: (Left) Graphite-CuBTC; (Right) GO-CuBTC. The CuBTC MOF crystal is cleaved along the [100] face; four layers of	

carbons are used to represent the graphite or GO. The color codes are: Carbon (Grey), Oxygen (Red), Hydrogen (White), and Copper (Light Salmon).141

CHAPTER 1

Introduction

1.1. Toxic Gas Removal

Toxic gas chemicals, if released, have the potential to form a poison gas cloud and spread over large areas. Those exposed to such a toxic gas cloud may be severely injured. For example, the Department of Homeland Security estimates that a major chlorine gas spill in an urban area can kill 17500 people.[1] Research data also point out that, although toxic gases account for only 0.3 percent of rail carloads, they carry enormous risks and potential liabilities.[2] According to an insurance study, a major chlorine rail spill in an urban area could cause 10200 fatalities and over \$7 billion in damages.[3] Because of the lethal potential and the related economic, environmental and national security concerns, many federal regulatory agencies have been imposing stricter policies towards toxic gases.[4-7] On the other hand, it is apparently impossible to prevent all toxic gas leakages. The challenge is then transformed into: how can we deal with the crisis of toxic gases leakages, or more specifically, what material can be used to effectively remove toxic gases, turning the toxic gases into non-toxic species? In order to answer that emergency call, we here choose ammonia (NH_3) and hydrogen sulfide (H_2S) as the simplest toxic gas representatives, and carry out computational studies to study the properties of the two toxic gases, to search for effective materials for the removal purpose, and to understand from the electronic/atomic levels how the toxic gases can be removed. Those molecular level understandings can shed

light on the fundamental mechanisms of toxic gas removal, and provide useful information for material design and process control.

1.2. Ammonia and Hydrogen Sulfide

Ammonia is one of the most highly produced inorganic chemicals and contributes significantly to the nutritional needs of terrestrial organisms by serving as a precursor to food and fertilizers. As of 2004, approximately 83% of ammonia was used as fertilizers either as its salts or as the solutions.[8] Although in wide use, ammonia is caustic and hazardous. Ammonia vapor has a sharp, irritating, pungent odour that acts as a warning of potentially dangerous exposure.[9] The average odour threshold is 5 ppm, and the exposure to very high concentrations of gaseous ammonia can result in lung damage and even death. The U.S. Occupational Safety and Health Administration (OSHA) has set a 15-minute exposure limit for gaseous ammonia of 35 ppm by volume in the environmental air, and an 8-hour exposure limit of 25 ppm by volume.[9, 10] The National Institute for Occupational Safety and Health (NIOSH) defines the IDLH (Immediately Dangerous to Life and Health) value of NH_3 to be 300, where the IDLH is the level to which a healthy worker can be exposed for 30 minutes without suffering irreversible health effects.[9, 11]

Hydrogen sulfide occurs naturally in crude petroleum, natural gas, volcanic gases, and hot springs. It is a highly toxic and flammable gas (flammable range: 4.3 ~ 46%). Being heavier than air, H_2S tends to accumulate at the bottom of poorly ventilated spaces. When hydrogen sulfide enters the environment, it remains in the atmosphere for about 18 hours.[12] Although very pungent at first, it quickly deadens the sense of smell, and potential victims

may be unaware of its presence until it is too late. H₂S is considered to be a broad-spectrum poison, which means that hydrogen sulfide can poison several different systems in the body, whereas the nervous system is most affected. Exposure to low concentrations of H₂S can cause irritation to the eyes, nose, or throat. It may also cause difficulty in breathing for some asthmatics. A brief exposure to high concentrations of hydrogen sulfide (greater than 500 ppm) can cause a loss of consciousness and possibly death. OSHA has set an acceptable ceiling limit for hydrogen sulfide of 20 ppm by volume in the workplace.[12] NIOSH recommends a 10-minute ceiling limit of 10 ppm by volume in the workplace.[12]

1.3. The Removal of Ammonia and Hydrogen Sulfide

The removal of NH₃ and H₂S requires an understanding of the combined effects of adsorption, diffusion and chemical reaction. In such a process, the toxic gas molecule is first adsorbed on the adsorbent. Chemical reaction then occurs, transforming the toxic compounds into non-toxic species, or species that are strongly adsorbed/bonded on the surface. The fast diffusion of the species, which is not directly involved in the adsorption/reaction, is in favor of the removal process. However, it is challenging to remove ammonia and hydrogen sulfide at ambient conditions (where most leakages happen) due to two facts: (a) weak physical adsorption at the room temperature; (b) water at ambient conditions, which competes with the toxic gases for the adsorption sites of the adsorbents.[13]

Researchers have been testing different adsorbents, such as carbonaceous materials,[14, 15] zeolites,[16, 17] silica,[18-20] alumina[21-23] and metal-organic frameworks (MOFs),[24-27] to remove ammonia and hydrogen sulfide. The results have

shown that the performance of hydrophilic materials, such as zeolites, silica and alumina, are significantly affected by the existence of water at ambient conditions. Water molecules have strong interactions with hydrophilic materials and can easily occupy the adsorption sites. A pre-treatment is usually required to remove water and this substantially increases the cost and hinders the application of those materials for heavy-duty removal of NH_3 or H_2S .

Carbonaceous materials are considered to be good adsorbents for many applications.[28, 29] By their nature, however, they are not ideal candidates for toxic gas removal. Taking activated carbons, the most widely used carbonaceous adsorbent, as an example, they are known to have large surface areas and pore volumes. Their hydrophobic surface is made up of randomly oriented graphene layers, and the surface properties can be modified by oxidation, introduction of nitrogen, halogens, or impregnation with various redox chemicals or metals. However, it is very difficult to produce active carbons with uniform surface properties. Also, activated carbons have an average pore size from 10 to 20 Å, which is much larger than the molecule size of NH_3 or H_2S , and thus the physical interactions between the toxic molecules and activated carbons are not strong enough to retain the adsorbates in the pores, especially at ambient conditions. Depending on the operating conditions, activated carbons exhibit adsorption capacities on the order of 10 mg/g for ammonia[30] and hydrogen sulfide.[31, 32]

As mentioned, there are two ways to improve the performance of activated carbons for the removal purpose of NH_3 or H_2S . The first is to modify the surface chemistry by oxidation, adding both functional groups and defects to the surface to enhance the adsorption/reaction of the adsorbate. The method, however, has the disadvantage that the oxidation can greatly

reduce the physical strength of activated carbons, and thus compromise the potential industrial application. The second way is to combine the favorable features of activated carbons (e.g. large surface area) and other adsorbents (e.g. MOFs) that provide strong interactions with NH_3 and H_2S . Those composites are expected to have good adsorption and diffusion properties (via activated carbons) and allow for chemical reactions to decompose NH_3 or H_2S (via the metal sites of MOFs). Dr. T. J. Bandosz group at The City College of New York has been following the latter route. They use graphite oxide (GO) and metal-organic frameworks to synthesize the GO/MOF nanocomposites to remove toxic gases. The GO, MOFs, and the GO/MOF nanocomposites from their experiments have demonstrated very promising results for NH_3 and H_2S removal.[33-37] Here in this thesis, we use similar adsorbents to study the fundamental mechanisms of toxic gas removal.

1.4. Graphene, Graphite Oxide and Metal-Organic Framework

Graphene, a monolayer of graphite, is a two-dimensional material that is considered to be an ideal surface model for theoretical investigation of adsorption, reaction and surface modification. It is accepted that the reactivity of graphene is much lower than that of single-walled carbon nanotubes.[38] Because it does not have the local strain due to the curvature-induced pyramidalization or the misalignment of the π orbitals of carbon atoms, which are used to explain the chemical activities of carbon nanotubes. Ever since the discovery of graphene, molecular doping and surface functionalization have been studied to control the electronic structure and surface chemistry of graphene. By adding charged groups to the surface, graphene is reported to be able to adsorb various gas molecules, including NH_3 , [39]

H₂O[40] and NO₂. [41, 42] The ability of adsorbing those molecules at a low concentration has allowed the successful application of the surface-modified graphene as chemical sensors.[43-45]

On the other hand, graphite oxide (GO), also known as graphene oxide, depending on whether graphite or graphene is used as the base material, has recently attracted the research attention due to its promising applications as an adsorbent material. Formed by treating graphite with very strong oxidizing agents (e.g., KClO₃/HNO₃), GO has a layered structure and a non-stoichiometric chemical composition, which depends on the level of oxidation. Recent advances in synthesis and experimental characterization of GO provide the possibility to control the structure and surface chemistry of the GO materials, leading to a renewed interest in using them particularly as reactive adsorbents. As a result of various levels of oxidation, the graphene layers of GO lose their polyaromatic character due to the incorporation of various oxygen-containing functional groups. Although the exact assignment of those groups is still controversial, it is generally accepted that the graphene layers have epoxy (1,2-ether), carboxyl and hydroxyl groups attached to carbon atoms.[46] The graphene layers are considered to be flat, with a slightly distorted tetrahedral configuration of carbons attached to hydroxyl groups. It is also proposed that carboxylic groups are located at the edges of the graphene layers. Although GO has been tested as adsorbents in the retention of NO, NO₂ and NH₃, [42] we still lack fundamental understanding, at the electronic and atomic levels, of the surface chemistry and reactive adsorption/intercalation mechanisms of those toxic gases on GO materials. This is probably due to the amorphous of GO materials, where a

uniform atomic model is impossible, and the challenge to study theoretically the chemical reactions in combination with adsorption and diffusion.

Metal-organic frameworks (MOFs) are inorganic-organic porous crystalline structures and can be synthesised by using a wide range of metal ions and organic ligands.[47, 48] The ability to tune the properties of MOFs via alteration of the organic ligands and metal clusters, along with the potential for high porosity with accessible, uniform pores, makes MOFs promising hybrid materials in the fields of gas adsorption, separation, catalysis, drug delivery and chemical sensors. Recently, the design of MOFs for catalytic applications has emerged as an important research field. There have been increasing efforts to tune the pore surface chemistry by functionalizing the pores, using groups such as -OH, -NH₂, -CH₃, -SH, -COOH and many others.[49, 50] The presence of the active metal sites is a valuable feature for reactive adsorption. By accepting electron pairs from the reactants, the open metal ions are reactive in homogeneous Lewis acid-base and oxidation catalysis. The metal sites also play an important role to determine the structure and the stability of the MOF materials.

Most studies on MOFs with unsaturated metal sites have been carried out to investigate CuBTC (copper(II) benzene 1,3,5-tricarboxylate, also known as HKUST-1) and M₂(dhtp) MOFs (M = Mg²⁺, Mn²⁺, Co²⁺, and Zn²⁺; dhtp = 2,5-dihydroxyterephthalic acid). As one of the first industrialized MOFs,[51] CuBTC has an open structure with easy access to the open metal copper sites inside the large pores. The Lewis acid properties of the Cu sites were first studied for cyanosilylation reactions,[52, 53] followed by other organic isomerization reactions[54] with good selectivities to the desired products. CuBTC has been shown to be a very good candidate to remove sulfur-containing molecules, such as

tetrahydrothiophene and thiophene, from natural gas, gasoline and diesel oil.[55, 56] It has also proved to be effective for the capture of other small molecules, such as ethylene oxide[57] and ammonia.[36]

1.5. Research Approach

Despite the urgent need to remove toxic gases and the experimental efforts of testing different adsorbents for the removal purpose, fundamental understanding of the removal mechanism is far from complete. From the view of computational studies, the challenge comes from the fact that the removal is a process correlated with adsorption, diffusion and chemical reactions, and thus requires multi-scale computational efforts. In this thesis, we use graphene/graphene oxide and CuBTC as the adsorbents to study, and employ multi-scale modeling techniques to investigate the fundamental mechanisms of the adsorption, diffusion and chemical reactions of NH_3 and H_2S on the adsorbents. The thesis is organized as follows: In Chapter 2, we briefly review the computational methods used in this thesis, from *ab initio* density functional theory (DFT), reactive force field (ReaxFF) method, to the classical molecular dynamics (MD) and Grand Canonical Monte Carlo (GCMC) calculations. Chapter 3 provides the DFT study of H_2S dissociation on a single vacancy defect of the graphene. Chapter 4 applies DFT calculations to study the adsorption and dissociation of NH_3 on a functionalized graphene surface. The role of different functional groups, including the epoxy (1,2-ether), carboxyl and hydroxyl groups, has been investigated. In Chapter 5, we combine the results from Chapter 3 (for the graphene vacancy defect) and Chapter 4 (for the graphene functional groups) to propose a new computational process to generate realistic atomic

models for graphene oxide. H₂S dissociation is investigated using those models at ambient conditions. Chapters 6, 7 and 8 present the computational efforts to use CuBTC as the adsorbent for the reactive adsorption of NH₃ and H₂S. In Chapter 6, the thermal stability of CuBTC is firstly investigated by ReaxFF molecular dynamics (RMD) calculations. Those calculations are served as a validation to use CuBTC at room temperatures. It is necessary to use a flexible CuBTC model and reactive force fields to study NH₃ adsorption on CuBTC. As discussed in Chapter 7, we perform DFT calculation to study the NH₃/CuBTC interactions, and classical GCMC simulation to calculate NH₃ adsorption isotherms on CuBTC. The results are also compared with the experimental data. Chapter 8 contains the RMD calculations of the reactive adsorption of NH₃ on CuBTC. We also study the NH₃/H₂O mixtures for the competitive adsorption. Finally, Chapter 9 offers a summary of the calculation results we have obtained, and discusses future research plans for toxic gas removal.

CHAPTER 2

Computational Methods

2.1. Density Functional Theory

Density Functional Theory (DFT) is one of the most widely used quantum mechanical approaches for *ab initio* calculations of the properties of atoms, molecules, crystals, surfaces. Over the past decades, we also see an increasing number of DFT calculations in modeling complex systems such as those in biology engineering and material sciences. DFT is based on a rigid conceptual framework, that the ground state energy of a system with n electrons, E , can be defined as a functional of its electron probability density, $\rho(\mathbf{r})$, where \mathbf{r} represents a particular point in the real space.[58] For any system, according to DFT formalism, there exists a one-to-one correspondence between the system energy and its electron density, that is, $E = E[\rho(\mathbf{r})]$.[59]

Here we give a brief introduction to the basic principles associated with the DFT methodology. It starts with a brief description of the Born-Oppenheimer approximation, followed by the Hohenberg-Kohn theorem and the Kohn-Sham formalism, and then the discussion of the exchange-correlation energy and various approximations. The application and limitation of DFT method is also discussed at the end. More details of the DFT formalism and other advanced features of the DFT method can be found from published books[60-63] or review articles.[64-70]

2.1.1. Born-Oppenheimer Approximation

Consider a system of M interacting particles in a container of volume V . The many-body Hamiltonian is a Hilbert space operator that governs the dynamics of both the electrons and the nuclei of the system:

$$\hat{H} = -\frac{\hbar^2}{2m_e} \sum_i \nabla_i^2 - \sum_{i,I} \frac{Z_I e^2}{|r_i - R_I|} + \frac{1}{2} \sum_{i \neq j} \frac{e^2}{|r_i - r_j|} - \sum_I \frac{\hbar^2}{2M_I} \nabla_I^2 + \frac{1}{2} \sum_{I \neq J} \frac{Z_I Z_J e^2}{|R_I - R_J|} \quad (2-1)$$

where electrons are denoted by lower case subscripts, and nuclei with charge Z_I and mass M_I are denoted by upper case subscripts. Although it is essential to include the many-body terms, namely the electron-electron Coulomb interactions, and the nuclei orientations that are affected by the electron interactions, the many-body hamiltonian can be simplified according to the fact that the inverse mass of the nuclei, $1/M_I$, is a small quantity, $M_I/m_e \approx 10^3 \sim 10^5$, so that the electrons respond almost instantaneously to the changes of nuclei positions, and thus the kinetic energy of the nuclei can be ignored. This is known as the Born-Oppenheimer approximation[71] and it works excellently for many applications, e.g. the band structure calculations of crystals, the nuclear vibration mode calculations of solids, and the electrical transport calculations for metals.[60, 61]

Using the Born-Oppenheimer approximation, the many-body Hamiltonian can be written as:

$$\hat{H} = \hat{T} + \hat{V}_{ext} + \hat{V}_{int} + E_{II} \quad (2-2)$$

where, in Hartree units,[72]

$$\hat{T} = \sum_i -\frac{1}{2} \nabla_i^2, \text{ the kinetic energy operator of the electrons;}$$

$\hat{V}_{ext} = \sum_{i,I} V_I(|r_i - R_I|)$, the potential acting on the electrons due to the nuclei;

$\hat{V}_{int} = \frac{1}{2} \sum_{i \neq j} \frac{1}{|r_i - r_j|}$, the potential energy operator of the electron-electron interactions;

E_{II} , the potential energy operator of the nuclei interactions, including the contributions from the external fields. The Hamiltonian can be used to determine the ground state. The ground state and its energy satisfy the eigenvalue equation $H\Psi_0 = E_0\Psi_0$, while the excited states have their energies $E_n > E_0$.

2.1.2. Hohenberg-Kohn Theorem

The concept of density functional theory firstly emerged in the work of Fermi and Thomas in the late 1920s, introducing the idea of expressing the energy of a system as a function of the total electron density.[65, 73] Later in 1951, Salter applied the same idea to the development of the Hartree-Fock-Slater method, which is now considered to be the predecessor theory of DFT.[74] However, it was not until 1964 that Hohenberg and Kohn finished the formal proof,[58] which is known as the Hohenberg-Kohn theorem, demonstrating that: (1) the electron density of a nondegenerate* electronic system uniquely defines the ground-state energy and the corresponding electronic properties; (2) if the exact functional is used, a trial electron density must give an energy greater than or equal to the true ground energy. The

* The Hohenberg-Kohn theorem is originally proved only for nondegenerate ground states, but has been shown to be valid for degenerate ground states too, see Ref. 60.

Hohenberg-Kohn theorem sits at the heart of DFT, but it does not provide the exact form of the density functional.

2.1.3. Kohn-Sham Method

The Hohenberg-Kohn theorem provides a theoretical guideline of finding the ground energy state by minimizing energy with respect to the electron density. Unfortunately, the relating kinetic energy to density is not known with a satisfactory level of accuracy, though the kinetic energy itself can be easily calculated from the wave function. For that reason, Kohn and Sham proposed an ingenious method in 1965, of combining the electron density and the wave functions.[59] They used a non-interacting reference system and repartitioned the total energy functional into the following form:

$$E[\rho] = T_0[\rho] + \int [\hat{V}_{ext}(r) + \hat{V}_{int}(r)]\rho(r)dr + E_{xc}[\rho] \quad (2-3)$$

where $T_0[\rho]$ is the kinetic energy of the electrons of the non-interacting reference system which has the same electron density ρ as the real system. Here the term “non-interacting” means that there is no electron-electron interaction, but the electrons interact with the nuclei.

$\hat{V}_{ext}(r)$ is the external potential, that is, the potential from the nuclei:

$$\hat{V}_{ext}(r) = \sum_I \frac{-Z_I}{|R_I - r|} \quad (2-4)$$

$\hat{V}_{int}(r)$ is a classical Coulomb interaction between the electrons. It includes the electron self-interaction explicitly and represents the interaction of ρ with itself.

$$\hat{V}_{\text{int}}(r) = \int \frac{\rho(r')}{|r' - r|} dr' \quad (2-5)$$

$$E_{\text{int}}[\rho] = \iint \frac{\rho(r')\rho(r)}{|r' - r|} dr dr' \quad (2-6)$$

The last functional, $E_{\text{xc}}[\rho]$ is the exchange-correlation energy. It includes all the energy contributions that have not been accounted for by the previous three terms:

- (1) The electron exchange;
- (2) The electron correlation;
- (3) A portion of the kinetic energy which is necessary to correct $T_0[\rho]$ to obtain the kinetic energy of the real system $T_e[\rho]$;
- (4) The correction of the self-interaction introduced by the classical Coulomb interactions for the electrons.

The philosophy is to put the energy contributions, which are difficult to obtain, into the $E_{\text{xc}}[\rho]$ functional, and hope that a reasonable approximation, which is till the biggest challenge of DFT, can be constructed for $E_{\text{xc}}[\rho]$.

2.1.4. Exchange-Correlation Functional

The exchange-correlation functional $E_{\text{xc}}[\rho]$ is generally divided into two separate parts, an exchange term $E_x[\rho]$ and a correlation term $E_c[\rho]$, although the legitimacy of such separation has been the subject of doubts:

$$E_{xc}[\rho] = E_x[\rho] + E_c[\rho] \quad (2-7)$$

The exchange term is normally associated with the interactions between the electrons of the same spin, whereas the correlation term accounts for those between the electrons of opposite spins. Both terms can be of two distinct types: the local functional, depending only on the electron density ρ at the local position \mathbf{r} , and the gradient corrected functional, which depends on both the electron density $\rho(\mathbf{r})$ and its gradient $\Delta\rho$. Despite the efforts and progress in the field, the approximate nature of the exchange-correlation functional is still the main source of the inaccuracy of DFT. A detailed description of different exchange-correlation functionals can be found elsewhere.[75-78]

2.1.5. Application and Limitation of DFT

Many different types of DFT applications have been developed in the past decade. DFT is now considered to be a routine tool to solve problems in atomic and molecular physics, such as the calculation of ionization and vibration spectra,[79-81] the structure of biomolecules,[82] polymers,[83-86] macromolecules, transition metal complexes,[67] the nature of active sites in catalysts,[87-90] and the study of chemical reactions, including the activation energy barrier, the reaction mechanism of the reaction pathway and the reaction kinetics.[91-95] Furthermore, DFT has made possible the development of *ab initio* molecular dynamics calculation where the forces are evaluated quantum mechanically “on the fly” to forward the dynamic evolution of the system in real time space.[96] Despite the popularity and success of DFT, its application still suffers from the following limitations:

- (a) The underestimation of the barriers of chemical reactions, the band gaps of materials, the energies of dissociating molecular ions, and the charge transfer excitation energies;
- (b) The overestimation of the binding energies of charge transfer complexes, the cohesive energies, bulk moduli and the response to an external electric field;
- (c) The difficulty in describing strongly correlated systems, degenerate and near-degenerate states;
- (d) The neglect of van der Waals interactions;

Further discussion about the limitation and challenges for DFT can be found from recent review papers.[\[97-101\]](#)

2.2. Reactive Force Field Method

2.2.1. ReaxFF method

Despite the fact that quantum calculations using DFT method can accurately describe the bulk and surface properties as well as the reaction mechanism, the expensive computational costs restrict the DFT applications to a few thousand atoms, and a few picoseconds of simulation time for *ab initio* MD. For many real-life problems, such length scale and time scale are not sufficient to observe the phenomena of interest. In contrast, empirical force fields employ harmonic equations to describe the bonds, angles, dihedrals and other structural properties. Algorithms have been also implemented to account for the long-range electrostatics and van der Waals interactions. These classical force fields have an advantage over DFT calculations since larger time-scale and length-scale are now accessible for

classical MD simulations. But the disadvantage is that they do not allow for bond breaking or forming, and thus are incapable of describing chemical reactions.

In 2001, van Duin *et al.*[102] used the bond-order concept, firstly introduced by Tersoff,[103] to develop a reactive empirical force field (ReaxFF) to study hydrocarbon systems. The assumption of ReaxFF is that the bond order BO'_{ij} for a pair of atoms can be obtained directly from the interatomic distance r_{ij} , as illustrated in Eq. (2-8):

$$\begin{aligned} BO'_{ij} &= BO'_{ij}{}^{\sigma} + BO'_{ij}{}^{\pi} + BO'_{ij}{}^{\pi\pi} \\ &= \exp\left[p_{bo1} \cdot \left(\frac{r_{ij}}{r_o^{\sigma}} \right)^{p_{bo2}} \right] + \exp\left[p_{bo3} \cdot \left(\frac{r_{ij}}{r_o^{\pi}} \right)^{p_{bo4}} \right] + \exp\left[p_{bo5} \cdot \left(\frac{r_{ij}}{r_o^{\pi\pi}} \right)^{p_{bo6}} \right] \end{aligned} \quad (2-8)$$

where the three sets of parameters (p_{bo1}, p_{bo2}) , (p_{bo3}, p_{bo4}) and (p_{bo5}, p_{bo6}) are used to describe the σ bond, the π bond and the $\pi\pi$ bond, respectively. Eq. (2-8) is defined so that the value of the three exponentials is unity below a threshold interatomic distance and zero at longer distances.

The nature of the bond orders BO'_{ij} concept allows the spontaneous bond breaking or forming, while keeping the energy and force continuous. The bond order values are updated at each MD step to determine the energy of the system. Eq. (2-9) describes the total energy from the ReaxFF formalism:

$$\begin{aligned} E_{tot} &= E_{bond} + E_{lp} + E_{over} + E_{under} + E_{val} + E_{pen} + E_{coa} + E_{C2} \\ &\quad + E_{triple} + E_{tors} + E_{conj} + E_{H-bond} + E_{vdWaals} + E_{Coulomb} \end{aligned} \quad (2-9)$$

For example, the bond energy E_{bond} is calculated from the bond order BO'_{ij} as:

$$E_{bond} = -D_e^{\sigma} \cdot BO'_{ij}{}^{\sigma} \cdot \exp\left[p_{be1} \left(1 - BO'_{ij}{}^{\sigma} \right)^{p_{be2}} \right] - D_e^{\pi} \cdot BO'_{ij}{}^{\pi} - D_e^{\pi\pi} \cdot BO'_{ij}{}^{\pi\pi} \quad (2-10)$$

where D_e^σ , D_e^π , $D_e^{\pi\pi}$, p_{be1} and p_{be2} are the bond parameters, BO_{ij}^σ , BO_{ij}^π and $BO_{ij}^{\pi\pi}$ are the corrected bond orders for σ bond, π bond and $\pi\pi$ bond, respectively. The nonbonded van der Waals and Coulomb interactions are calculated between every atom pair at each MD step, to describe the connectivity. To account for the polarization effects, the electronegativity equalization method (EEM)[104] is applied to dynamically derive the atomic charges. A detailed description of energy terms in Eq. (2-10) and the algorithms for the nonbonded calculation can be found from the ReaxFF manual[105] and publications.[51, 102, 106] It is worthwhile to note that upon the dissociation of a bond, its bond order and the energy terms for the bond, the angle and the dihedral angle where such bond is involved, are zero. This characteristic ensures a smooth transition of the energy and the force for the ReaxFF calculations.

2.2.2. ReaxFF code implementation

The first ReaxFF implementation came from the original serial FORTRAN code of van Duin et al. in 2001, with the release of ReaxFF parameters for hydrocarbons.[102] The source code integrated parameter optimization and molecular dynamics (MD) calculation engine. Although not optimized for CPU or memory usage, and can efficiently handle a system with less than a few thousand atoms, it is still the only code that can develop new ReaxFF parameters from scratch or retrain the existing ReaxFF parameters for new applications. In 2003, the San Diego Supercomputer Center (SDSC), in conjunction with the Computer Science and Engineering department at the University of California, San Diego (UCSD), released the Grid Assessment Probes (GRASP) software package, which is designed to give

system architects and applications developers a simple and easy-to-use set of probes for gaining insight into the performance and reliability of grid computing platforms.[107] Thompson *et al.* implemented the first parallel version of ReaxFF in the GRASP package, and later in a more popular parallel package, LAMMPS (Large-scale Atomic/Molecular Massively Parallel Simulator).[108] GRASP is a C++ code, and it calls the optimized version of the original FORTRAN routines to calculate the bond orders and the corresponding energies, and thus exactly matches the results from the serial FORTRAN code. There are two different implementations of ReaxFF in LAMMPS. One is from the original FORTRAN code: similar to the implementation in GRASP; the FORTRAN routines are included directly as libraries files into the main C++ calculation engine. The charge equilibration calculation in LAMMPS uses a standard parallel conjugate gradient algorithm for sparse linear system, which is different from the original FORTRAN code, where the electrostatic interactions are modeled as shielded interactions with Taper corrections. The other ReaxFF implementation in LAMMPS is from the PuReMD (Purdue Reactive Molecular Dynamics) code, developed by Aktulga *et al.*[109-111] The PuReMD code is also written in C++. It uses dynamics memory allocation and has incorporated other optimizations to extend the simulation capability to larger systems (total number of atoms $\sim 10^7$).

Recently ReaxFF has also been incorporated into commercial simulation packages. Scientific Computing & Modeling (SCM) has implemented and parallelized ReaxFF in the ADF® (Amsterdam Density Functional software).[112] The implementation has significantly optimized the original FORTRAN code, removing the memory bottlenecks, and integrated a Graphic User Interface (GUI) for the on-the-fly analysis of calculation results.

Since the version 4.0, GULP (General Utility Lattice Program), a program for performing a variety of types of simulation on materials, has added ReaxFF into its force field libraries.[113] GULP has been incorporated into Materials Studio® software,[114] an integrated multi-scale modeling environment that delivers a complete range of simulation methods. Since the recent version 6.0, users can perform ReaxFF MD calculations from the GULP module of the Materials Studio® software.

2.3. Classical Atomistic Molecular Modeling

2.3.1. Molecular Dynamics Simulation

Classical Molecular Dynamics (MD) simulation describes the evolution of a system by integrations over time and space. For each discrete time step, the positions and velocities of the atoms are calculated based on Newton's equation of motion. The time step, normally on the order of femtoseconds, needs to be smaller than the vibrational frequencies of the atoms to include all energy contributions. The accuracy of the simulation depends highly on the quality of the force field used. AMBER,[32] CHARMM,[115] GROMOS,[116] COMPASS[117] and OPLS[118] are among the most widely used classic force fields.

Forces and potentials governing the motion of atoms can be classified as bonded, short-range and long-range interactions. Bonds, valence angles interactions and dihedral (torsion) interactions are the most common bonded interactions, and take place typically within a few angstroms and constitute a very small portion (1~5%) of the computational complexity of an MD calculation. Short-range and long-range interactions are referred as non-bonded interactions and their computation may account for up to 99% of the total

computation time. Short-range potentials (such as van der Waals interactions) decay faster and can be appropriately truncated for a desired level of accuracy. Long-range forces (such as electrostatic interactions), on the other hand, do not decay as rapidly as short-range interactions, which require either expensive computations or algorithmic techniques for reducing the complexity. In general, the size of the simulation system is only limited by the accessible computer memory. Using massively parallel computing platforms and highly optimized MD simulation packages (DLPOLY,[119] GROMACS,[120] LAMMPS,[108] NAMD[121] *et al.*), it is possible to carry out microsecond long simulations for systems with tens of thousands of atoms.

Ensemble describes how the simulated system is coupled to the physical environment, and is an important parameter to MD calculations. Under the microcanonical ensemble (NVE), the number of particles (N), the volume (V) and the total energy (E) are held constant, imitating a system inside an insulated, rigid container. The isochoric-isothermal canonical ensemble (NVT) maintains constant temperature (T) by placing the system in contact with a thermal reservoir. A variety of thermostat methods are available to add or remove energy from the boundaries of an MD system, approximating the canonical ensemble. Popular techniques to control temperature include velocity rescaling, the Nosé-Hoover thermostat,[122, 123] the Berendsen thermostat[124] and the Langevin dynamics method.[125, 126] As for the isobaric-isothermal canonical ensemble (NPT), the volume of the system is allowed to vary in order to maintain a constant pressure (P). Different barostats such as the Nosé-Hoover, Berendsen and Parrinello-Rahman[127, 128] can be used for this purpose.

2.3.2. Grand Canonical Monte Carlo Simulation

The Grand canonical Monte Carlo (GCMC) simulation method is considered to be the standard molecular simulation tool to calculate adsorption properties. It relies also on classical force fields to describe the interactions and to calculate the energies. In standard GCMC simulations, a rigid framework is usually assumed, that is, the adsorbent is treated as frozen. The advantage of such assumption is that the simulation requires only the host-guest and guest-guest interactions, which can substantially reduce the computational cost, and also make the force field parameterization easier. It has proved to be a good approximation for a large number of nanoporous materials, in particular zeolites.[129, 130]

However, the rigid model does not work for all adsorbents. People have been reporting the breathing effects of MOFs on the adsorption of confined fluids,[131-135] and developing two approaches to study the adsorption in flexible porous materials. The first approach is based on the argument that although the adsorption process can affect the structure of the adsorbent, the deformation can still be treated locally, and in a reasonable range of temperature and pressure, the overall volume change of the adsorbent is negligible. Therefore, we can use the grand canonical ensemble by keeping the unit cell fixed and allowing the atoms of the adsorbent to move around their equilibrium positions. The second approach allows changes of the unit cell parameters. This can be achieved by performing the Monte Carlo calculation in the osmotic ensemble, where the typical moves are: molecular insertion or deletion, molecular moves (translation, rotation, internal conformation change, etc.), and changes of the unit cell parameters. More details about the GCMC method[136,

137] and the osmotic ensemble of describing flexible adsorbents[138-142] can be found elsewhere.

CHAPTER 3

Adsorption and Dissociation of Hydrogen Sulfide on Graphene Single Vacancy

3.1. Introduction

Known as a good adsorbent, graphene is an ideal surface model for theoretical investigations of the combined effects of adsorption, reaction and surface modification. Pristine graphene sheets are inert to chemical reactions. There are several ways to control the surface properties of graphene, among which defects are widely used. A defect on the graphene surface can change the topology, roughness and electronic properties of the surface, and thus affects not only the adsorption and diffusion by which gas molecules travel from the bulk phase to the surface, but also the adsorbate-adsorbent interactions. Defects such as adatoms, pentagon-heptagon carbon pairs (also known as the Stone-Wales defect), mono- and multi-vacancies, have been observed from experiments and theoretical molecular simulations. For example, tight-binding molecular dynamic simulations have confirmed that the single vacancy is stable on the graphene surface, and the recombination of single vacancy defects will involve a large energy barrier that entails heating the graphene surface to above 3000 K.

Ab initio DFT calculations from our group have shown that graphene with metastable defects has potential application as a catalyst due to the presence of carbon atoms with unsaturated valence in the structure. Water is found to dissociate over the defective sites on graphene. The dissociation follows many possible reaction pathways, some of which have

activation barriers lower than half of the energy barrier for bulk water dissociation. Methane is also found to dissociate over the defective carbon atoms, making the hydrogen production a continuous process.

Being the simplest sulfur-containing molecule, H₂S and its adsorption and dissociation properties are of interest to many applications, not limited to the benefits of toxic gas removal. H₂S can be used as a benchmark model to study the adsorption of methanethiol (HSCH₃) and the growth mechanism of self-assembled monolayers (SAMs) on metal surfaces.[143] It is also a common impurity in fossil fuel feed streams that are widely used nowadays for hydrogen production.[144] H₂S can provoke at ppm level the poisoning of catalysts, due to the formation of S overlayers from H₂S dissociation.[145] The adsorption and dissociation of H₂S has been studied by *ab initio* DFT calculations on different systems, including noble metals,[145-148] transition metals,[149] metal oxides[150] and other catalytic surfaces.[151, 152] Hydrogen sulfide adsorption on a defective graphene has also been reported recently.[153] The *ab initio* DFT calculations showed that the energy favorable configuration is the one with the sulfur atom heading to the center of the vacancy. The conductivity of the defective graphene changed upon H₂S chemisorption. However, the calculation mainly focused on the density of states (DOS) of the defective graphene, and did not discuss the H₂S adsorption on different sites or the dissociation mechanism of H₂S on the vacancy defect.

In this chapter, we describe *ab initio* DFT calculations to study the dissociation of H₂S on graphene with a single vacancy (sv-graphene). The adsorption geometries and energies for the molecular and dissociative states of H₂S are calculated. We also investigate

the reaction pathways and the corresponding energy barriers for H₂S dissociations on the vacancy defect. The chapter is organized as follows: Section 3.2 summarizes the model and the method used in the calculations; Section 3.3 contains the results of the calculations, from the adsorption to the dissociation of H₂S on the sv-graphene; Section 3.4 summarizes the conclusions.

3.2. The sv-graphene Model and Computational Method

The graphene with a single vacancy (sv-graphene) is modeled by removing one carbon atom from a 48-carbon rectangle graphene sheet. In order to avoid the image interactions, we use the slab geometry with a 15-Å vacuum. Periodic boundary conditions are employed in the plane of the sv-graphene. One H₂S molecule is studied for the adsorption. Three sites on the sv-graphene surface are investigated, namely, on top of a carbon atom (T), the center of a carbon hexagon (C), and the center of a carbon-carbon bond (B), as shown in Figure 3.1. For each investigated site, four different orientations of the H₂S molecule, demonstrated in Figure 3.2 as the “V”, “Λ”, planar and vertical shapes, are employed to set up the initial adsorption configuration. All sites around the vacancy (C₁ to C₁₂) are examined in the calculation. The 2-D electron density profile is provided in Figure 3.3. The sites with lower density are likely to favor the adsorption/dissociation by accepting the electrons from H₂S or its decomposed species (-HS, -S or -H).

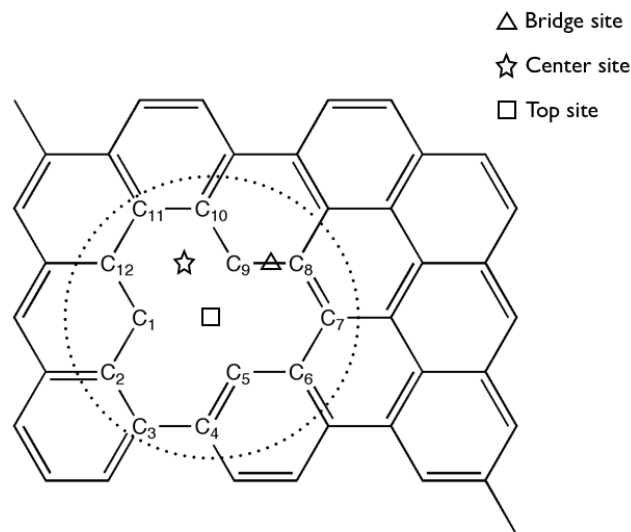


Figure 3.1. The sv-graphene model, created by removing one carbon atom from a 48-carbon rectangle graphene. Three different sites, namely, on top of a carbon atom (T), the center of a carbon hexagon (C), and the center of a carbon-carbon bond (B) have been investigated for possible adsorption and/or dissociation of H₂S.

The results presented in this chapter are obtained using plane-wave pseudopotential *ab initio* DFT calculations.[62, 95] Becke-Lee-Yang-Parr (BLYP) exchange-correlation functionals are employed.[78, 154] Typical accuracy for BLYP functionals[63] is provided in Table (3-1).The structure is relaxed by the CPMD code (version 3.13)[155] for H₂S and carbon atoms of the sv-graphene. The force convergence criteria of 0.02 eV/Å is used. The planewave cutoff of 40 Ry and the density cutoff of 320 Ry have been tested and found to be adequate for the ultrasoft pseudopotentials.[156] Reaction pathways, energy barriers and transition states are obtained using the nudged elastic band method[157] with the climbing image modification[158] (CI-NEB), as implemented in the Quantum-Espresso package (version 4.12).[159]

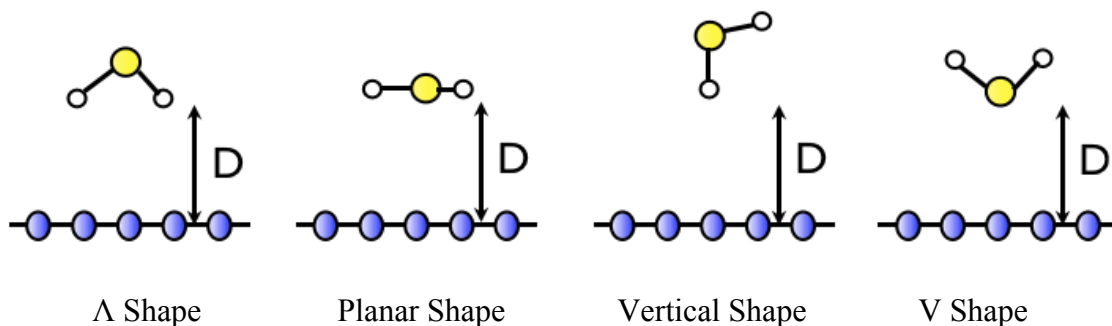


Figure 3.2. Four different initial H₂S orientations, indexed as V shape, planar shape, vertical shape and Λ shape. D is the adjustable parameter to describe the distance between H₂S and the sv-graphene surface.

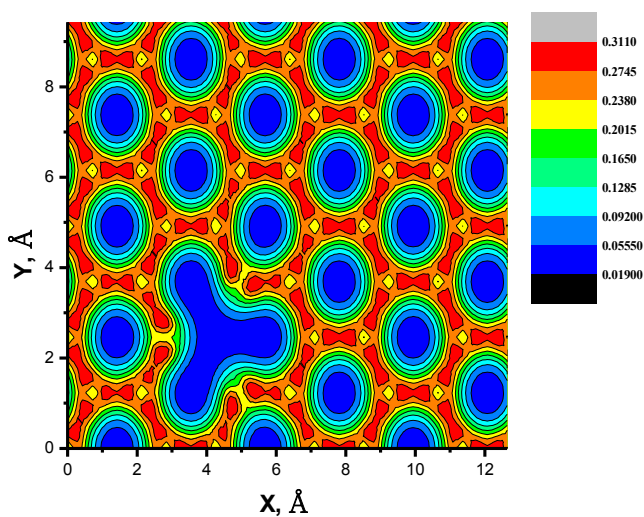


Figure 3.3. The 2-D electron density profile for the sv-graphene surface.

The adsorption energy (E_{ads}) is defined as the difference between the energy of the H₂S adsorbed graphene surface ($E_{H_2S-Surface}$) and the sum of the energies for the relaxed pristine surface ($E_{Surface}$) and the gas-phase H₂S molecule (E_{H_2S}), see equation (3-1). A negative value of E_{ads} indicates an exothermic process.

$$E_{ads} = E_{H_2S-Surface} - \{E_{Surface} + E_{H_2S}\} \quad (3-1)$$

The minimum energy pathway for each dissociative reaction is mapped out by the CI-NEB method. NEB is a method to identify the saddle points and determine minimum energy paths between known reactants and products. The method works by optimizing a number of intermediate images along the reaction path. Each image finds the lowest energy and maintains equal spacing to neighboring images. The constrained optimization adds spring forces along the band between images and projects out the component of the force that is perpendicular to the band. The climbing image is a small modification to the NEB method in which the highest energy image is driven up to the saddle point. This image does not ‘feel’ the spring forces along the band. Instead, the true force at this image along the tangent is inverted. In this way, the image tries to maximize its energy along the band, and minimize in all other directions. When this image converges, it will be at the exact saddle point. Because the highest image is moved to the saddle point and it does not ‘feel’ the spring forces, the spacing of images on either side of this image will be different. It is useful to do a minimization with the regular NEB method before the ‘climbing’ flag is turned on, to have a good estimation of the reaction coordinate around the saddle point. If the maximum image is initially very far from the saddle point, and the climbing image is used from the outset, the path would develop very different spacing on either side of the saddle point. In this chapter, 7 images are used in the search for the saddle point of each dissociative reaction. The transition state of the optimized reaction coordinate is approximated by the image of highest energy. The overall reaction energy ΔE_{rxn} is calculated by equation (3-2).

$$\Delta E_{rxn} = \sum E_{prod} - \sum E_{react} \quad (3-2)$$

Where $\sum E_{prod}$ and $\sum E_{react}$ are the sum of energies of the products and reactants, respectively. A negative ΔE_{rxn} indicates an exothermic reaction. The formation energy is calculated by equation (3-3), where E_{H_2S} , $E_{Surface}$ and $E_{H_2S-Surface}$ are the energies for the H₂S molecule, the sv-graphene surface and the relaxed H₂S-graphene system, respectively.

$$E_{formation} = \{E_{H_2S} + E_{Surface}\} - E_{H_2S-Surface} \quad (3-3)$$

Table 3-1. Typical accuracy for *ab initio* DFT calculations with BLYP functional.[63]

Physical property	Typical mean absolute error
Bond length	0.01 Å
Bond angle	1°
Barrier height	3~4 kcal/mol
Atomization energies	1~2 kcal/mol 10~20 kcal/mol for metal dimers
Binding energies	5~10 kcal/mol
Heats of formation	5~20 kcal/mol
Hydrogen bond strengths	0.5~1 kcal/mol

3.3. Results and Discussion

3.3.1. The accuracy of *ab initio* DFT calculation

It is important to recognize the accuracy of the DFT method before running a calculation. The accuracy for DFT calculations depends not only on the pseudopotentials and functionals

used, but also on the system and the properties calculated. In order to report DFT results, one need to pay close attention to the following principles:

- a. Accurately define the mathematical problem by specifying the employed exchange-correlation functional;
- b. Spepcify the numerical details used in performing the calculations;
- c. Run the calculation with great caution when you need to compare the results from calculations with different numerical approximations;
- d. Always try the unambiguous comparison between the calculation results and experimental observations.

3.3.2. Adsorption of H₂S on the sv-graphene surface, D = 2.5 Å

Before calculating the adsorption of H₂S on the sv-graphene surface, the pseudopotentials are tested for bulk properties of H₂S and graphene. The calculated bond length and angle for H₂S, HS species and the pristine graphene are summarized in Table (3-2). The structural properties are in good agreement with experimental data and other calculation results.

Table 3-2. The structural properties of H₂S, HS and Graphene.

	Bond length, Å			Bond angle, degree				
	This work	Exp.	Cal.	This work	Exp.	Calc.		
H ₂ S	1.353	1.328 ^[160]	1.349 ^[161]	1.346 ^[150]	92.0	92.2 ^[162]	91.6 ^[161]	91.7 ^[150]
HS	1.352	1.345 ^[162]	1.354 ^[161]	1.352 ^[150]				
Graphene	1.420	1.420 ^[163]	1.423 ^[164]		120.0	120.0 ^[163]		

When the H₂S molecule is approaching the sv-graphene surface, it first encounters the weak van der Waals interaction. The H₂S molecule could be physisorbed on the sv-graphene surface if it loses energy upon interaction with the surface. Furthermore, H₂S can rearrange its electronic configuration to get chemisorbed. Depending on the distance to the surface and the kinetic energy, the H₂S molecule can move closer to the surface, where it has a stronger repulsion interaction with the surface. If the H₂S molecule could respond by changing its electron structure to favour the interaction with the surface (to bring down the total energy), it can become decomposed into species (-HS/-H or -S/-H). We first study an initial distance $D = 2.5 \text{ \AA}$ to find out the possible chemisorbed or dissociation states for H₂S. As illustrated in Figure 3.2, all possible H₂S orientations are investigated on different sites (B, C or T) of the sv-graphene surface.

The results demonstrate that, if initially placed 2.5 \AA from the sv-graphene surface, H₂S gets chemisorbed to the sv-graphene surface. From the structural parameters provided in Table (3-3), the final distance between H₂S and the sv-graphene surface depends on both the

adsorption site (B, C or T) and the starting orientation of H₂S. The final orientation of H₂S is the same as the initial value. This implies a weak interaction between H₂S and the sv-graphene surface, where H₂S does not need to adjust its orientation to overcome the adsorption energy barrier. Such a weak interaction is also reported by a recent *ab initio* DFT calculation.[153] The nature of *ab initio* DFT (zero K calculation) determines that H₂S does not have the kinetic energy to spontaneously overcome the energy barrier and move from the chemisorption state to decompose on the sv-graphene surface. Further calculations (e.g. reactive MD calculations in Chapter 5) are needed to investigate whether at a certain temperature H₂S would have enough kinetic energy to behave spontaneously from the chemisorption to dissociate on the sv-graphene surface.

The interaction between H₂S and the sv-graphene surface is weaker than that for H₂S-metal surface interactions. H₂S is reported to be adsorbed about 2.5~2.8 Å above Au (111) and Cu (111) surfaces.[145] The adsorption energies are summarized in Table (3-4) for different H₂S orientations on different sites. The “Top”, “Bridge” and “Center” sites are demonstrated in Figure 3.2. E_{ads} is the adsorption energy for one H₂S molecule. $d_{S-Surface}$ is the distance between the S atom of H₂S and the sv-graphene surface. According to the definition of H₂S orientation in Figure 3-2, the initial $d_{S-Surface}$ values are different. d_{S-H} represents the S-H bond length of H₂S, and $\angle HSH$ is the bond angle for H₂S. The calculated structural properties of a gas-phase H₂S molecule are also provided for reference.

Table 3-3. The optimized structural parameters for the H₂S molecule, which is placed initially 2.5 Å from the sv-graphene surface. “D^{*}” represents the optimized distance between the sv-graphene and the atom (in bracket) of the H₂S molecule.

		The two H-S bonds, Å		H-S-H, degree	D [*] , Å
Bridge	Λ	1.361	1.352	92.1	2.93 (H)
	V	1.353	1.353	92.2	4.81 (S)
	Planar	1.353	1.358	92.0	3.26 (H)
	Vertical	1.353	1.358	92.2	3.17 (H)
Center	Λ	1.353	1.359	92.1	3.20 (H)
	V	1.353	1.353	92.1	4.05 (S)
	Planar	1.353	1.353	91.9	3.25 (H)
	Vertical	1.353	1.361	92.2	3.02 (H)
Top	Λ	1.353	1.359	92.1	3.22 (H)
	V	1.353	1.353	92.3	4.46 (S)
	Planar	1.353	1.362	92.2	2.91 (H)
	Vertical	1.353	1.365	92.2	2.84 (H)

Table 3-4. The adsorption characteristics of the H₂S molecule on the sv-graphene surfaces: adsorption energy (E_{ads}), H₂S-Surface distance ($d_{S-Surface}$) and the structural properties of H₂S (d_{S-H} for the two H-S bonds). The calculated structural properties of the gas-phase, H₂S (g), are provided for reference. The H₂S molecule is placed initially 2.5 Å from the sv-graphene surface.

The distance is measured between the lowest atom of H₂S and the surface.

H ₂ S Orientation	Site	E_{ads} (kcal/mol)	$d_{S-Surface}$ (Å)	d_{S-H} (Å)	$\angle HSH$ (°)
Planar	Top	-8.532	2.50 → 4.19	1.352/1.361	92.2
	Bridge	-8.424	2.50 → 4.53	1.353/1.358	92.0
	Center	-7.834	2.50 → 4.19	1.353/1.353	91.9
V-shape	Top	-7.861	2.50 → 4.82	1.353/1.353	92.3
	Bridge	-7.734	2.50 → 4.81	1.353/1.353	92.2
	Center	-7.429	2.50 → 4.04	1.353/1.353	92.1
Λ-shape	Top	-8.447	3.21 → 4.51	1.353/1.359	92.1
	Bridge	-8.274	3.21 → 4.10	1.352/1.361	92.1
	Center	-8.300	3.21 → 4.44	1.353/1.359	92.1
Vertical	Top	-8.671	3.52 → 4.10	1.353/1.365	92.2
	Bridge	-8.480	3.52 → 4.38	1.353/1.358	92.2
	Center	-8.343	3.52 → 4.28	1.352/1.361	92.2
H ₂ S (g)				1.353	92.0

The small adsorption energies from Table (3-4) confirm the weak interaction between H₂S and the sv-graphene surface. The orientation of the H₂S molecule has a negligible effect on the adsorption energy. H₂S is pushed away from the surface in all calculated systems and the internal structure of H₂S is slightly deformed with respect to its gas-phase counterpart.

The bond length of adsorbed H₂S structures varies between 1.352 and 1.365 Å, and the angle changes from 91.9° to 92.3°. We also find that, no matter which site it is initially placed above, H₂S is relaxed to the top site (T). The orientation also changes so that for the final chemisorption state, the sulfur atom is closest to the surface. The favorable adsorption site and the adsorption energy on other metal surfaces are listed in Table (3-5).

Table 3-5. H₂S adsorption on different surfaces: the optimized H₂S-Surface distance, adsorption site and the adsorption energy.

Surface	d _{S-Surface} (Å)	Favorable site	E_{ads} (kcal/mol)
Ag (111)[165]	2.82	Top	-3.92
Au (111)[166]	2.62	Top	-6.23
Cu (111)[167]	2.40	Top	-6.00
Fe (100)[146]	3.00	Top	-10.61
Pd (111)[168]	2.34	Top	-12.00
This work	4.10	Top	-8.67

3.3.3. Adsorption of H₂S on the sv-graphene surface, D = 1.5 Å

The results from Table (3-6) show that, if the H₂S molecule is initially placed closer to the sv-graphene surface, it can dissociate into HS and H species on the single vacancy; see also Figure 3.4 for the final structure of such a dissociation. It is interesting to notice that only two initial configurations lead to the dissociation of H₂S: the planar configurations on the bridge and top carbon sites. This is probably due to the fact that for the planar orientation, all three

atoms can interact with the surface, so the electrons can easily be adjusted to allow for the dissociation. The H₂S molecule, with the initial “V” orientation, forms a new C-S bond on the top site of the surface. This agrees with the previous *ab initio* DFT calculation that the top site of the single vacancy is more active for H₂S dissociation. The results from Table (3-6) also imply that the distance of 1.5 Å between H₂S and the sv-graphene surface does not guarantee the dissociation of H₂S on the single vacancy.

Table 3-6. The optimized structural parameters for the H₂S molecule, which is placed initially 1.5 Å from the sv-graphene surface. “D*” represents the optimized distance between the sv-graphene and the atom (in bracket) of the H₂S molecule.

		The two H-S bonds, Å		H-S-H, degree	D*, Å
Bridge	Λ	1.353	1.353	91.8	3.06 (H)
	V	1.444	1.454	83.0	1.30 (S)
	Planar	Dissociated into HS and H, see Figure 3.4			
	Vertical	1.353	1.353	91.8	4.14 (H)
Center	Λ	1.353	1.354	92.0	3.06 (H)
	V	1.353	1.353	92.0	4.20 (S)
	Planar	1.353	1.353	92.0	3.16 (H)
	Vertical	1.353	1.354	92.1	3.10 (H)
Top	Λ	1.353	1.353	92.0	4.95 (H)
	V	1.445	1.454	83.0	1.28 (S)
	Planar	Dissociated into HS and H, see Figure 3.4			
	Vertical	1.353	1.353	92.0	4.04 (H)

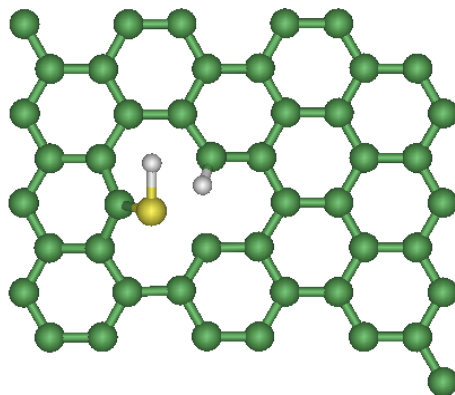


Figure 3.4. The dissociation of H₂S on the sv-graphene surface: the optimized final structure, corresponding to the two dissociation states in Table (3-6).

3.3.4. Dissociation of H₂S on the sv-graphene surface, D = 0.5 Å

In order to observe more dissociative reactions of H₂S, we place it closer to the surface, D = 0.5 Å. The dissociations of H₂S on the sv-graphene surface are observed for all investigated cases. The full understanding of H₂S dissociation on the single vacancy requires a knowledge of all the stable states, transition states and reaction pathways. However, the potential energy surface for such a system is complicated due to the dangling bonds introduced by the single vacancy. While H₂S and H₂O are similar in both their molecular geometry and chemical properties, we here identify all the intermediates states for H₂S dissociation, and compare the results with the previous *ab initio* DFT calculations of H₂O dissociation on the same single vacancy model. The results are shown in Figure 3.5.

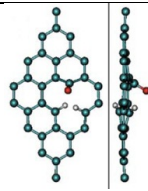
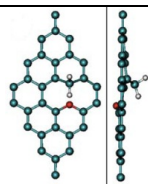
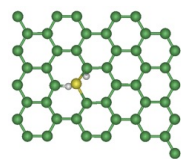
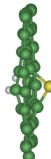
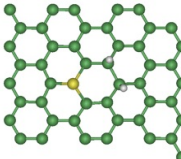
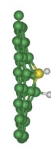
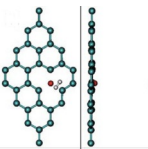
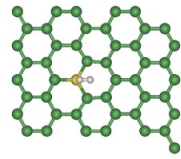
The results show that H₂S has similar intermediate states as those of H₂O on the sv-graphene surface.^[169] This is due to the fact that S and O are in the same row of the periodic table of the elements. They have the same arrangement of the electrons on the outermost orbital, which in turn determines that the S/O atoms and H₂S/H₂O molecules have similar

reaction activities. The dissociation of H₂S, however, is not identical to that of H₂O molecule. The intermediate state (f), which is observed for H₂O dissociation on the sv-graphene surface, is not stable for H₂S dissociation. Instead a new intermediate state (h) is identified where the sulfur atom occupies the middle site of the single vacancy and is bonded to three neighboring carbon atoms. The S-C bond lengths are 1.763 Å, 1.764 Å and 1.765 Å, respectively. It is worth noting that H₂S dissociates only on the C₁, C₅ and C₉ sites of the single vacancy.

Not all investigated initial configurations lead to different H₂S dissociations. Some configurations will be relaxed to the same final structure but with different adsorption energies. The positive formation energies from Figure 3.5 imply that the adsorption and dissociation of H₂S on the sv-graphene surface is energy favorable. We compare the formation energies and use the most favorable configuration (the one with largest formation energy) for the following CI-NEB calculations to identify the reaction pathways and reaction energy barriers

Figure 3.5. Intermediate states for H₂S dissociation on the sv-graphene surface. Rows from left are: intermediate states from Ref.; top view, lateral view and side view of the intermediate states in this work, where (a) is the initial state; (h) is the final state; the S atom occupies the vacancy site on the surface and hydrogen is pushed away from the surface; (b) to (e) are intermediate states corresponding to the ones in Ref.[169]. The formation energy is provided in the last row.

	H ₂ O dissociation, from Ref.[169]	Top view	Side view	E _{formation} (kcal/mol)
(a)				8.67
(b)				63.20
(c)				40.36
(d)				35.97
(e)				75.13

(f)		-	-	-
(g)				56.01
(h)	-			70.13
(p)				72.09

3.3.5. Reaction mechanism of H₂S dissociation on the sv-graphene surface

The reaction pathways of H₂S dissociation on the sv-graphene surface are explored by CI-NEB calculations. Similar to the previous calculations of H₂O dissociation, the study of H₂S dissociation over the single vacancy requires knowledge of all possible stable states, transition states and reaction energy barriers. As discussed in Figure 3.5, H₂S has similar intermediate states as those of H₂O for the dissociation reaction on the sv-graphene surface. Being the global minimum state of the potential energy surface for H₂O dissociation, image (e) is also the global potential energy minimum state for H₂S dissociation on the sv-graphene surface.

The CI-NEB method requires that the initial reactants and the final products be defined beforehand. The relaxed configuration where H₂S is adsorbed on the sv-graphene surface (image (a) in Figure 3.5) is chosen as the reactant and also as the energy reference for other pathway calculations. Image (p) in Figure 3.5, where the sulfur atom occupies the vacancy site on the surface and hydrogen is released from the surface, is the final production state for the H₂S dissociation reaction. We calculate all the possible reaction pathways by connecting the initial state (a), an intermediate state (b to h), and the final state (p). All dissociations of H₂S along the investigated pathways are exothermic. The activation energy barrier for the reaction pathway “a → e → p” is shown in Figure 3.6, where “Initial”, “IM(e)”, “TS” and “Product” represent the initial state (a), global energy minimum state (e), transition state along the reaction pathway and final state (p), respectively.

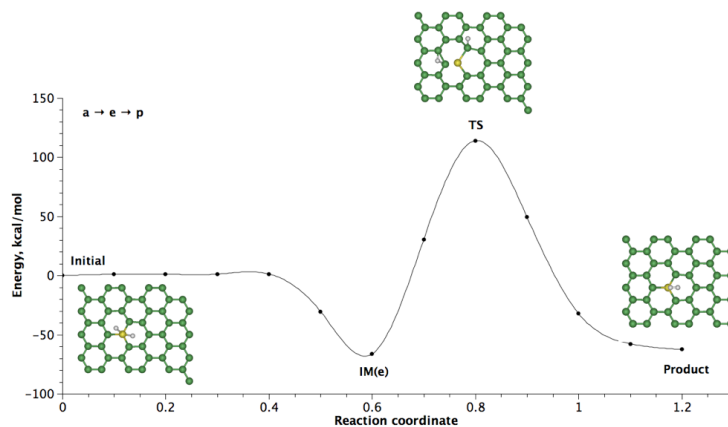


Figure 3.6. The reaction energy barrier for H₂S dissociation along “a → e → p” pathway: “Initial”, “IM(e)”, “TS” and “Product” represent the initial state (a), global energy minimum state (e), transition state along the reaction pathway and final state (p), respectively.

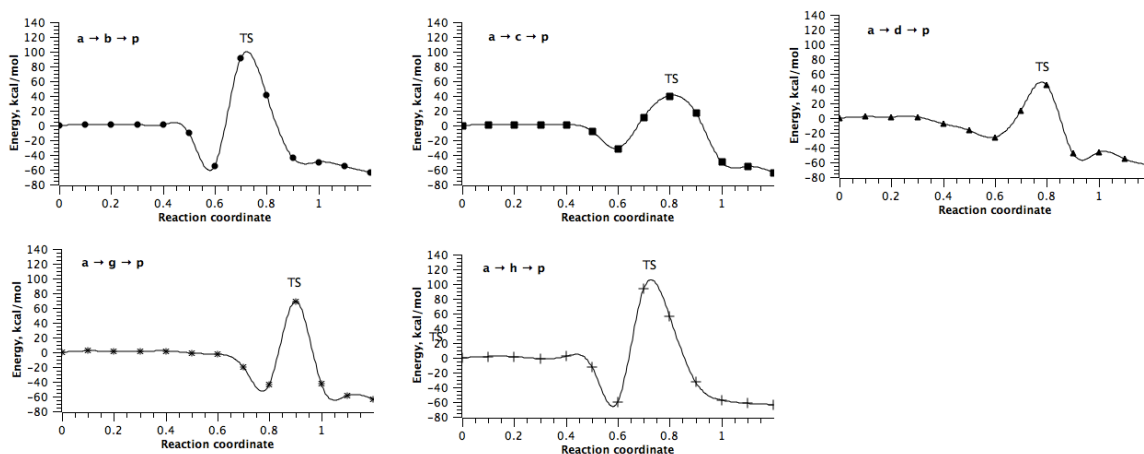


Figure 3.7. The reaction energy barriers for H₂S dissociation reactions along: “a → b → p”, “a → c → p”, “a → d → p”, “a → g → p” and “a → h → p” pathways, where “a”, “b”, “c”, “d”, “g” and “h” are corresponding to the stable intermediate states described in Figure 3.5.

The energy barriers for the other five calculated reaction pathways are plotted in Figure 3.7. Though state (e) is the global energy minimum of the potential energy surface for H₂S dissociation reaction, the energy barrier along that reaction pathway is also the highest, 114.00 kcal/mol. In our previous work,^[169] the energy barriers for water dissociation on the sv-graphene along three favorable pathways are 16 kcal/mol (a → b → p), 49 kcal/mol (a → f → p) and 55 kcal/mol (a → p). As for H₂S dissociation, “a → c → p” and “a → d → p” are two energetically favorable pathways, with activation energy barriers 40.44 kcal/mol and 44.98 kcal/mol, respectively. The dissociation energy barriers are summarized in Figure 3.8 for an easy comparison.

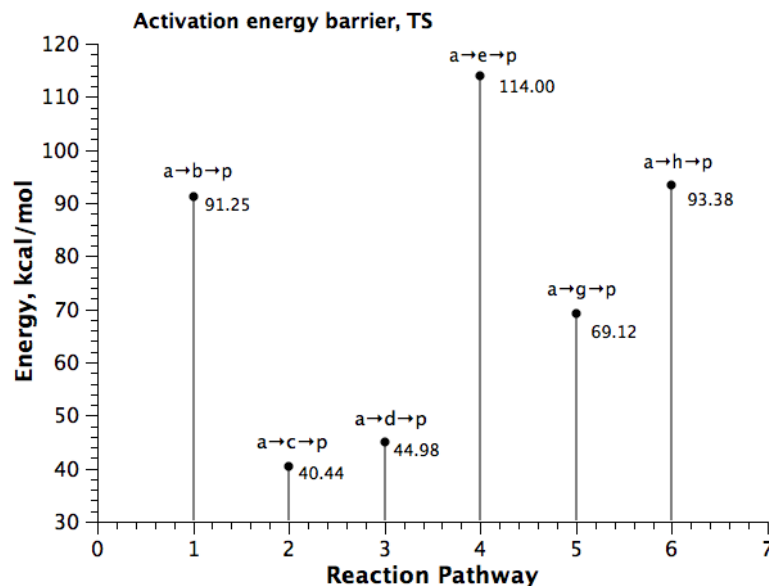


Figure 3.8. The reaction energy barriers: a comparison for H₂S dissociation along different reaction pathways.

3.4. Conclusions

Plane-wave pseudopotential *ab initio* DFT has been employed to investigate the adsorption and dissociation of H₂S on the single vacancy of graphene. We identify the stable adsorption structures of the sv-graphene models and the adsorption energies for H₂S adsorption. H₂S adsorption is energetically favorable in the middle of the single vacancy, with hydrogen atoms up and the sulfur atom lying closest to the surface. Stable intermediate states for H₂S dissociation are also determined from the calculation. Our results indicate that H₂S will dissociate in a similar way to H₂O for the same system. Both the adsorption and dissociation of H₂S are exothermic, and the calculated lowest activation energy barrier for dissociation is around 40.44 kcal/mol, indicating the dissociation of H₂S on a graphene single vacancy is a favorable process.

The DFT calculations confirm that the vacancy on the graphene surface can provide active sites for H₂S dissociation. Besides H₂S, we also calculate the interaction of NH₃ with the sv-graphene model. As shown in Figure 3.9, NH₃ is found to dissociate into -NH₂ and -H species on the vacancy. The two species form new bonds with the carbon atoms on the vacancy. Other species (-NH, -N, and -H), as potential dissociation products, are also easily bonded to the vacancy sites. In the case of -H species, the new C-H bond is 1.08 Å, very close to the C-H bond length of the alkanes. The -N radical stays in the middle of the single vacancy and forms three C-N bonds with the neighboring carbon atoms. The C-N bond lengths are 1.407 Å, 1.420 Å, and 1.420 Å, which are similar to that of C-C bonds. The bond angles of C-N-C are 120.1°, 120.1° and 120.0°. This means that the -N radical can ‘mend’ the single vacancy and thus maintain the flat hexagonal surface structure, similar to that of a pristine graphene surface.

For the graphene materials synthesized in the laboratory or produced in industry, there are other defects, such as the Stone-Wales defect, the adatoms, and also functional groups on the surface. What are the most active sites for NH₃ and H₂S dissociation? If there is a co-existence of vacancy defects and functional groups, can NH₃ and H₂S overcome the steric hindrance effects from the functional group to dissociate on the vacancy defects? These questions remain unresolved, but we will try to address the challenges in Chapter 4 and Chapter 5.

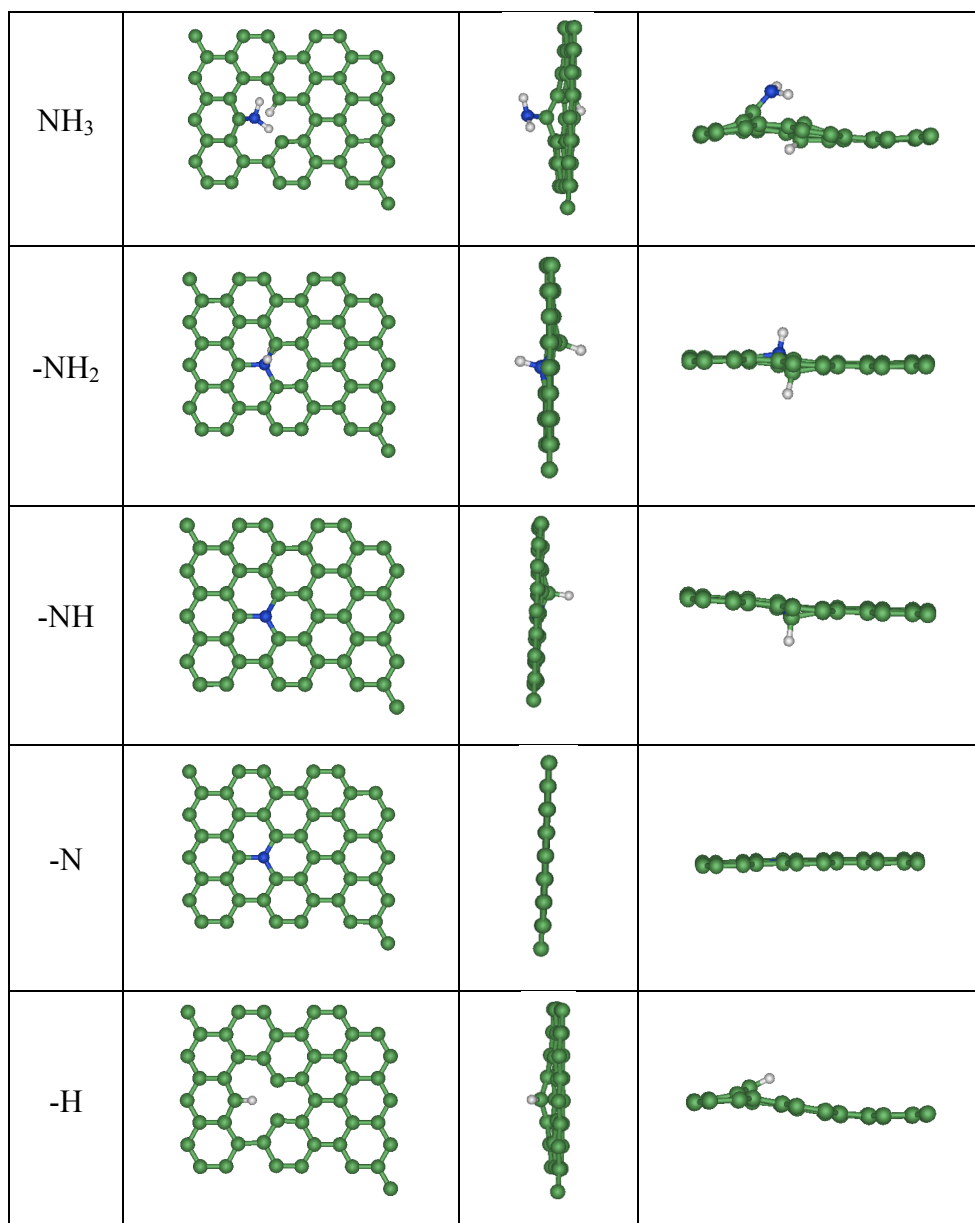


Figure 3.9. NH₃ dissociation on the sv-graphene model.

CHAPTER 4

Adsorption and Dissociation of Ammonia on Graphite Oxide

4.1. Introduction

Graphite oxide (GO), also known as graphitic acid, has attracted much research attention since its first synthesis by Brodie in the mid 1800s.[170] GO is known to be a promising material as an adsorbent,[171, 172] and is also widely used as a precursor to produce graphene platelets,[173, 174] an important component for composite materials,[26] and has been studied in the context of many applications. On the other hand, although the precise chemical structure of GO has been the research interest over the years,[174-181] the atomic structure of GO is still ambiguous. This is mainly due to the amorphous nature and the nonstoichiometric atomic composition of GO, and also the lack of precise analytical characterizing techniques.

As summarized in a recent review paper,[182] the earlier GO models are based on regular lattices with discrete repeat units, see Figure 4.1. The model proposed by Hofmann and Holst is composed of epoxy groups spread across the basal planes of graphite, with a net molecular formula of C_2O . [183] The model from Ruess is a modification of Hofmann and Holst's, which takes into consideration the hydrogen content and thus incorporates hydroxyl groups into the basal plane.[184] Scholz and Boehm suggested a model in 1969, where they do not include any epoxide or ether group, but have regular quinoidal species on a corrugated backbone.[185] Another important model is from Nakajima and Matsuo,[180] a lattice framework that forms a 2-stage graphite intercalation compound. The later models are based

on the nonstoichiometric and amorphous nature of GO, among which the most widely cited work is from Lerf and Klinowski.[\[46\]](#) Lerf and Klinowski envision GO as made of pseudo flat oxidized graphene layers. More precisely, the carbon grid would be formed by a random distribution of benzene and aliphatic rings. The oxygen functional groups would consist of 1,2 ethers and hydroxyl groups randomly distributed on the basal planes, see Figure 4.2.

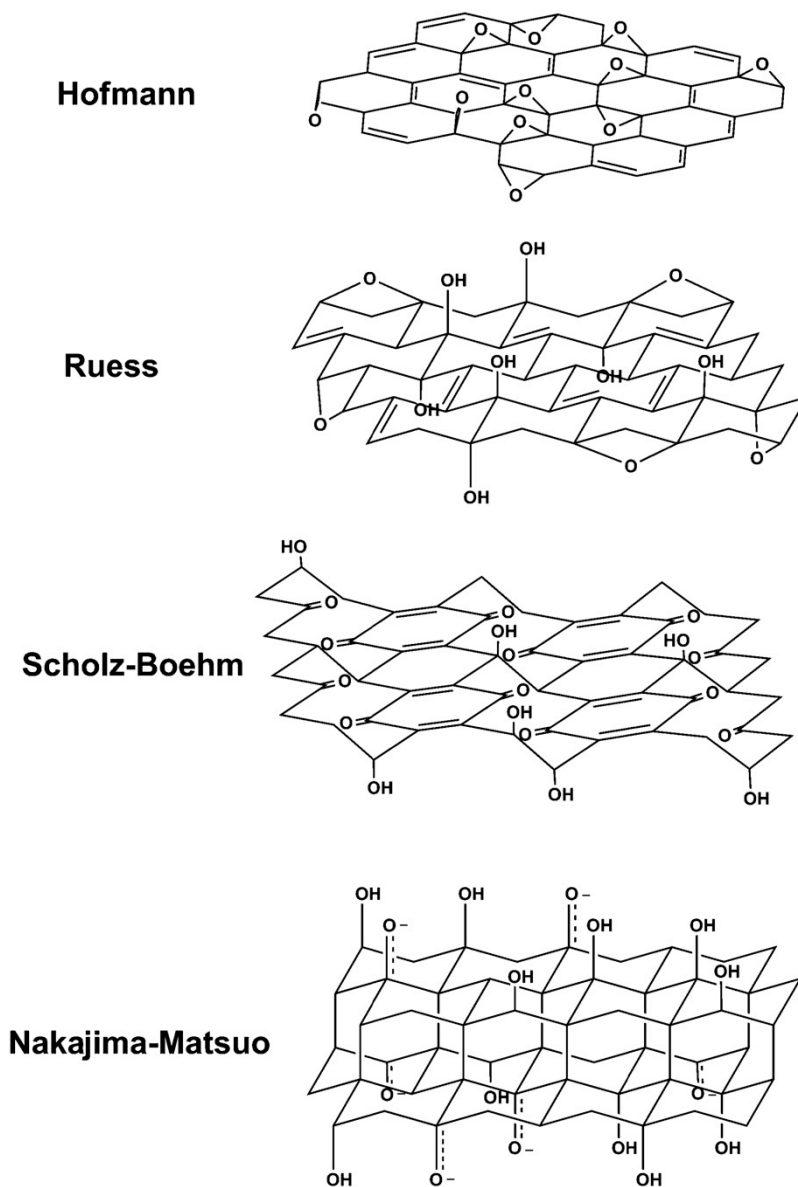


**Figure 4.1. A summary of several lattice structural GO models: Hofmann (in 1939);[183]
 Ruess (in 1946);[184] Scholz-Boehm (in 1969);[185] Nakajima-Matsuo (in 1988).[179]
 Adapted from Ref.[182]**

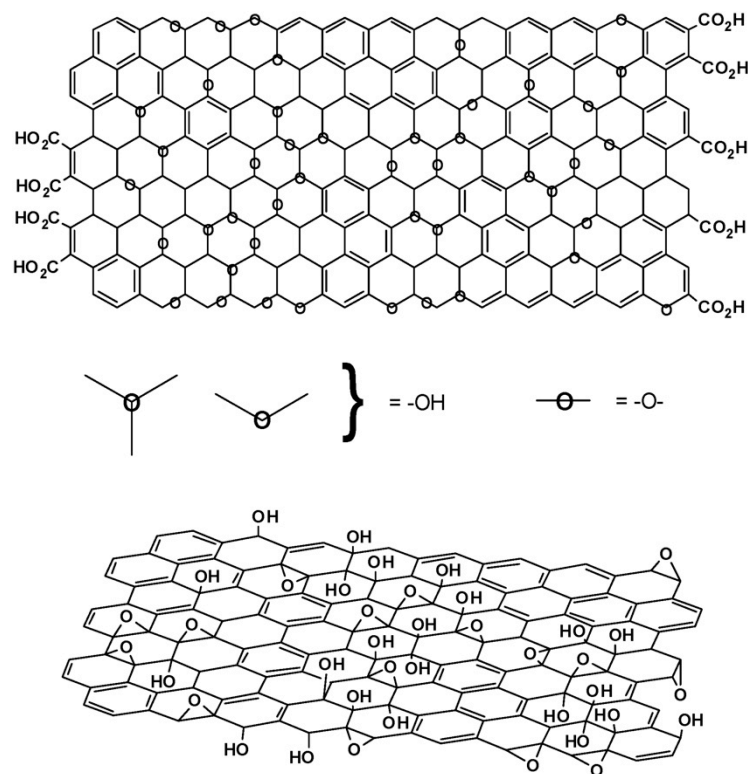


Figure 4.2. Lerf-Klinowski GO models[46]: (top) with carboxylic groups on the basal plane; (bottom) without any carboxylic group on the basal plane.

In general, these models focus on the morphology of the carbon grid, the location and types of the oxygen functional groups, and the effect of the extent of oxidation. They address the chemistry and topography of GO regardless of the method of GO preparation involved. So far, to our knowledge, no results have been published addressing the differences induced in the materials by the synthesis route applied. There are three methods widely used to synthesize GO: the Staudenmaier,[186] Brodie[170] and Hummers-Offeman methods.[187] All of them involve the oxidation of graphite but differ in the type of mineral acids and oxidizing agents used, as well as in the time of preparation, and the type of washing and drying processes. In the Staudenmaier method, the oxidizing mixture consists of nitric acid,

sulfuric acid and potassium chlorate. In the Brodie method, only nitric acid and sodium chlorate are used whereas in the Hummers method, potassium permanganate, sulfuric acid and hydrogen peroxide are involved. The difference, in terms of the GO product, includes the fact that the interlayer distance is usually smaller for GOs prepared via the Brodie method ($\sim 6\text{-}7 \text{ \AA}$) than for GOs obtained by the Hummers-Offeman method ($\sim 8\text{-}9 \text{ \AA}$). Moreover, the Hummers method leads to lower C/O atomic ratio (~ 2.25) than the Brodie (~ 2.6) or Staudenmeier method (~ 2.9), suggesting a greater extent of the oxidation process. In addition, despite the extensive washing process, GO prepared by Hummers method contains a significant amount of sulfur.[13]

In recent experiments our collaborators, T.J. Bandosz and co-workers have tested two GOs for ammonia adsorption. One is prepared with sulfuric acid as part of the oxidizing mixture (GO-H) and the other without any sulfur-containing compound (GO-B). Though both GOs have carboxyl, epoxy and hydroxyl groups, the results show that ammonia reacts only with the carboxylic group in GO-B, but with carboxyl, epoxy and sulfur groups in GO-H.[13] On the other hand, water is found to affect the ammonia adsorption, possibly due to the water-GO interaction and the formation of ammonium.[172] However, we still lack a fundamental understanding of the adsorption and reaction mechanisms of ammonia on GO materials, which in turn prevents us from designing better GO adsorbents.

In this chapter, we use the density functional theory (DFT) method to investigate the interactions between the molecules (NH_3 and H_2O) and the functional groups on the GO surface (the carboxyl, epoxy, hydroxyl and sulfonic acid groups) to identify the active site on the GO surface and to compare the competitive adsorption/dissociation between NH_3 and

H₂O. Results are compared with experimental results where possible. The chapter is organized as follows: Section 4.2 summarizes the GO model and the method used in the calculations; Section 4.3 contains the results of the calculations, from the discussion of stable GO models, the H₂O interaction with the GO models, and the adsorption and dissociation of NH₃ on the GO models; Section 4.4 gives the conclusions from the calculations in this chapter.

4.2. The GO Model and Computational Method

Much work has been done on the arrangement of functional groups on the GO surface, and it is accepted that the hydroxyl groups are located on top of individual carbon atoms in an upright position with respect to the basal plane.[178] The carboxyl groups usually sit at the edge of the carbon layers and the content is small.[181] As for the epoxy groups, the oxygen atom forms 1, 2-ether or 1, 3-ether groups on the carbon grid, where the numbering scheme refers to a three-member C-O-C ring and a four-member carbon-oxygen ring, respectively. However, little is known about the position and concentration of the sulfonic groups.

In this chapter, the GO surface is modeled by functionalizing a graphene sheet using the carboxyl, epoxy, hydroxyl and sulfonic groups. As shown in Figure 4.3, the GO model is made up of 32 carbon atoms, with periodic boundary conditions applied for X and Y directions. Functional groups are attached to the sites (C₁ to C₄). The 15-Å vacuum along the Z direction has been tested and found adequate to avoid interlayer interactions.

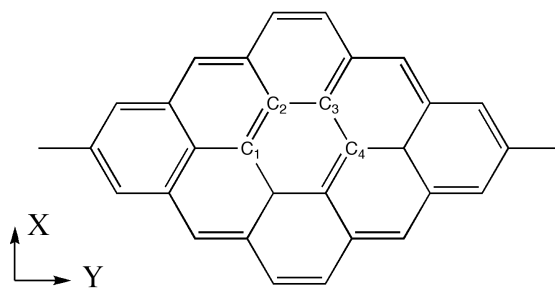


Figure 4.3. The GO model: C₁, C₂, C₃, and C₄ are four sites where functional groups are attached. The system is periodic for both X and Y directions.

Similar to Chapter 3, the DFT calculations use plane-wave pseudopotentials[62, 95] with the Becke-Lee-Yang-Parr (BLYP) exchange-correlation functional.[78, 154] All the structures are relaxed until the forces on the atoms are less than 0.01 eV/Å in the CPMD code (version 3.13).[155] Ultrasoft pseudopotentials[156] with a plane-wave cutoff of 40 Ry and a density cutoff of 320 Ry are applied for the calculations. Reaction pathways, energy barriers and transition states are obtained by using the nudged elastic band method[157] with the climbing image modification (CI-NEB),[158] as implemented in the Quantum-Espresso package (version 4.12).[159]

The adsorption energy (E_{ads}) is computed as the difference between the energy of the adsorbed molecule ($E_{Adsorbate-Surface}$) and the sum of the relaxed bare surface ($E_{Surface}$) and the corresponding gas-phase species ($E_{Adsorbate}$) energies, using the equation (4-1). The negative adsorption energy indicates an exothermic adsorption process.

$$E_{ads} = E_{Adsorbate-Surface} - \{E_{Surface} + E_{Adsorbate}\} \quad (4-1)$$

The minimum energy pathway for each dissociative reaction is determined by CI-NEB techniques. NEB is a method for finding saddle points and minimum energy paths between reactants and products. A discrete representation of the reaction is employed, with the points (moving images) along the path being relaxed using first derivative information. We use seven images to search for the saddle point of each dissociative reaction. The transition state (TS) of the optimized reaction coordinate is approximated by the image of highest energy. For all the possible TS reported in this chapter, we find only one imaginary frequency. The geometry optimizations starting from its back and forward to nearest configurations along the reaction path end up at the adsorbed and dissociated states, respectively. The overall reaction energy ΔE_{rxn} is calculated by equation (4-2), where the first and second terms represent the sum of energies of products and reactants, respectively. A negative ΔE_{rxn} indicates an exothermic reaction.

$$\Delta E_{rxn} = \sum E_{prod} - \sum E_{reac} \quad (4-2)$$

4.3. Results and Discussion

4.3.1. The GO models

We investigated 14 different GO models, as listed in Table 4-1. Models 1, 2, and 3 are a graphene with one carboxyl group; Models 4, 5, and 6 are designed to test how the hydroxyl group affects the adsorption; Models 7, 8, and 9 have one sulfonic group on the basal graphene surface; Models 10, 11, and 12 contain one hydroxyl and one carboxyl groups on the surface; Models 13 and 14 have 1, 2-ether and 1, 3-ether groups, respectively. The

pristine graphene has a planar geometry with sp^3 hybridization carbon atoms, characteristic of an aromatic system. When a functional group is attached to the carbon atom of the graphene surface, it will break down the double-bonded conjugated system and make the neighboring carbon atom unpaired. Those carbon atoms are saturated with hydrogen atoms in the calculations.

The results show that if two functional groups are added to the neighboring (C_1 , C_2) or the meta-positioned carbon atoms (C_1 , C_3), they can react with each other and release a formic acid molecule (Models 1 and 2), a H_2O molecule (Models 4 and 5) or a peroxy acid molecule (Models 10 and 11). Sulfonic groups are not stable for the designed functional patterns. We observe the release of a sulfurous acid molecule for Models 7, 8 and 9. Model 14 is not stable due to the high formation energy of 1, 3-ether, and the structure is eventually relaxed into Model 13. The relaxed stable structures from Models 3, 6, 12 and 13 are shown in Figure 4.4 for both the top and the side views.

Table 4-1. 14 investigated GO models. “COOH”, “OH”, “SO₃H”, “H” and “C” stand for carboxyl, hydroxyl, sulfonic groups, hydrogen atoms used to saturate the functionalized benzene hexagon, and the carbon atoms on which the epoxy groups are formed.

Site	1	2	3	4	5	6	7	8	9	10	11	12	13	14
C_1	COOH	COOH	COOH	OH	OH	OH	SO ₃ H	SO ₃ H	SO ₃ H	COOH	COOH	COOH	C	C
C_2	H			H			H			OH			C	
C_3		H			H			H			OH			C
C_4			H			H			H			OH		

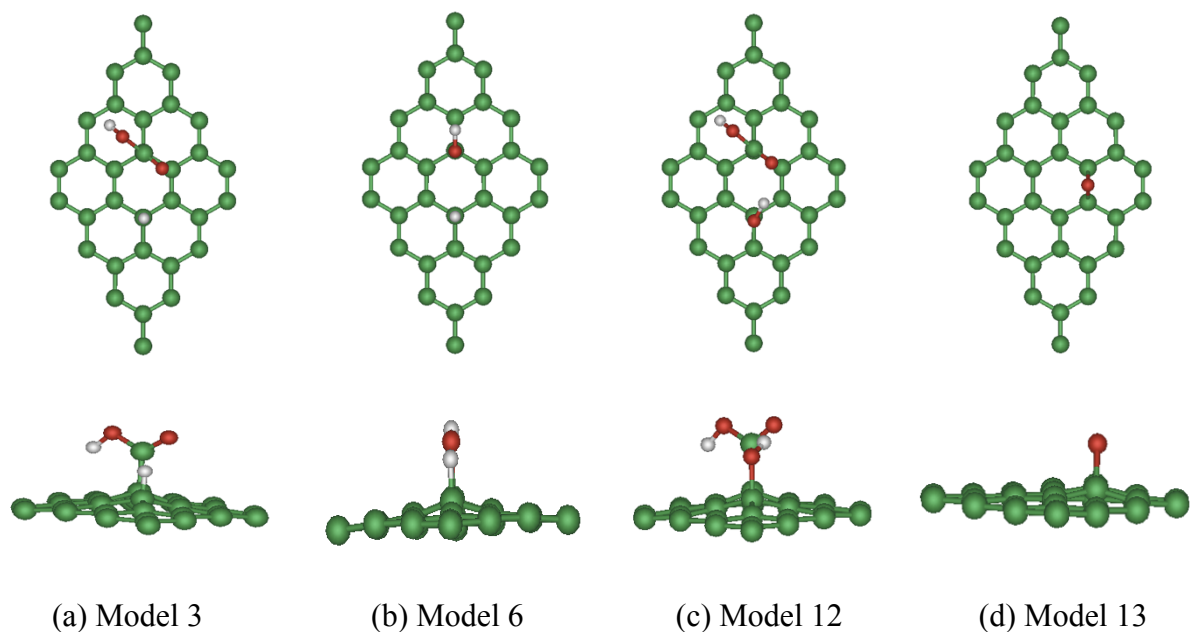


Figure 4.4. The optimized structures for the GO models: (a) Model 3; (b) Model 6; (c) Model 12; (d) Model 13.

4.3.2. H₂O interaction with the GO models

The four optimized structures of Figure 4.4 are used to calculate the interactions between H₂O and the functional groups of the GO surface. One H₂O molecule is introduced into each simulation box and is placed initially around the functional group. The Laio-Parrinello metadynamics method[188, 189] implemented in the CPMD package is used to identify all the stable intermediate states as well as the possibility of dissociation states.

The results show that H₂O does not dissociate in any of the four calculated systems. It is known that H₂O forms hydrogen bonds with electronegative atoms, such as fluorine, nitrogen or oxygen. The hydrogen atom of the H₂O molecule must be covalently bonded to the electronegative atom to form the hydrogen bond. It can occur between molecules or

within different parts of a single molecule. The hydrogen bond interaction is stronger than the van der Waals interaction but weaker than the covalent or ionic bonds. Various energetic[190, 191] and structural[192] criteria have been used to estimate the hydrogen bond in theoretical calculations. We use a geometrical criterion[193] here to examine whether a hydrogen bond is formed between H₂O and the oxygen atom from the hydroxyl or carboxyl functional groups. The hydrogen bond is considered to exist if the following three conditions are satisfied:

- (1) The distance R_{OO} between the oxygen atoms is smaller than a threshold value 3.75 Å;
- (2) The distance R_{OH} between the oxygen atom of the functional group and the hydrogen of H₂O is smaller than a threshold distance 2.46 Å;
- (3) The bond angle α between the O₁–O₂ direction and the O₂–H direction is smaller than 30°, where H, O₁ atoms are from H₂O and O₂ from the functional groups.

Table 4-2. The hydrogen bond information between the H₂O molecule and the functional groups: “O_{HC}”, “O_C”, “O_H” represent the oxygen atom from carboxyl single-bonded oxygen, carboxyl double-bonded oxygen and hydroxyl oxygen, respectively. “HB” stands for the existence of hydrogen bond.

	Model 3		Model 6		Model 12		Model 13
	O _{HC}	O _C	O _H	O _H	O _{HC}	O _C	O
R_{OO} , Å	3.62	2.98	2.85	2.97	3.23	3.02	3.02
R_{OH} , Å	2.99	2.07	1.87	3.22	3.21	2.39	2.04
α , degree	0.23	0.15	0.06	0.31	0.31	0.28	0.03
HB	NO	YES	YES	NO	NO	YES	YES

The calculation results for the hydrogen bond information are listed in Table 4-2. For all four calculated systems, H₂O can form hydrogen bonds with oxygen atoms from the functional groups. In addition, when there is a carboxyl group, H₂O prefers to form the hydrogen bond with the carbonyl oxygen atom. The result explains the experimental findings that by forming hydrogen bonds with the functional groups, water can screen the accessibility of epoxy and carboxyl groups for the interaction with ammonia and thus limits the amount of ammonia adsorption/dissociation.[13] This implies that if GO materials are used for ammonia removal, any effort in removing H₂O beforehand or during ammonia adsorption/dissociation will enhance the process by providing more available catalytic sites to ammonia molecules. The adsorption energies for the four calculated systems are: -0.48 kcal/mol (Model 3), -3.74 kcal/mol (Model 6), 2.95 kcal/mol (Model 12) and -0.23 kcal/mol (Model 13). The adsorption of H₂O on Model 12 is endothermic due to the steric effect from the hydroxyl group.

4.3.3. NH₃ interaction with the GO models

Similar to Section 4.3.2, one single NH₃ molecule is added to Models 3, 6, 12 and 13 to study the interaction between NH₃ and the functional groups. NH₃ does not dissociate on the hydroxyl group of Model 6. In the relaxed final structure, NH₃ is 4.51 Å from the surface. The three N-H bonds of the NH₃ molecule, the O-H bond of the hydroxyl group, and the C-O bond of the oxygen atom and the carbon atom of the surface are 1.035 Å, 1.035 Å, 1.039 Å, 0.98 Å and 1.54 Å, respectively. On the other hand, the N-H bond length for the gas-phase NH₃ is 1.036 Å. The O-H and C-O bonds of pristine Model 6 (Figure 4.4(b)) are 0.98 Å and

1.53 Å. The adsorption energy E_{ads} is -1.88 kcal/mol, which indicates a physisorption of NH_3 on the hydroxyl group of Model 6.

The results also show that NH_3 dissociates on the carboxyl group of Model 3 and 12 by forming a new amide structure, as shown in Figure 4.5. This agrees with the experiments, where the formation of amines has been confirmed by X-ray photoelectron spectroscopy (XPS), Fourier transform infrared (FTIP) and X-ray diffraction (XRD) characterizations.[13] Comparing results from Model 3 and Model 12, the hydroxyl group in Model 12 does not affect the NH_3 reaction with the carboxyl group, and the bond lengths of O-H and C-O for the hydroxyl group remain the same as the ones of the optimized Model 12. Ammonia dissociation affects the GO structure. The C-C bond, connecting the carbon atom of the carboxyl group to the basal surface, is prolonged from 1.63 Å to 1.69 Å for Model 3, and 1.64 Å to 1.68 Å for Model 12. Ammonia reacts with the epoxy group on Model 13. A hydroxylamine molecule is formed as the reaction product and is released from the GO surface, which is demonstrated in Figure 4.5. The ammonia dissociation is an exothermic reaction on Model 13, with the reaction energy -26.70 kcal/mol, but is an endothermic reaction for Models 3 and 12, with reaction energies 7.19 kcal/mol and 55.60 kcal/mol, respectively. The larger endothermic reaction energy from model 12 is due to the steric effect from the hydroxyl group, as we observe the same trend for H_2O adsorption on Model 12.

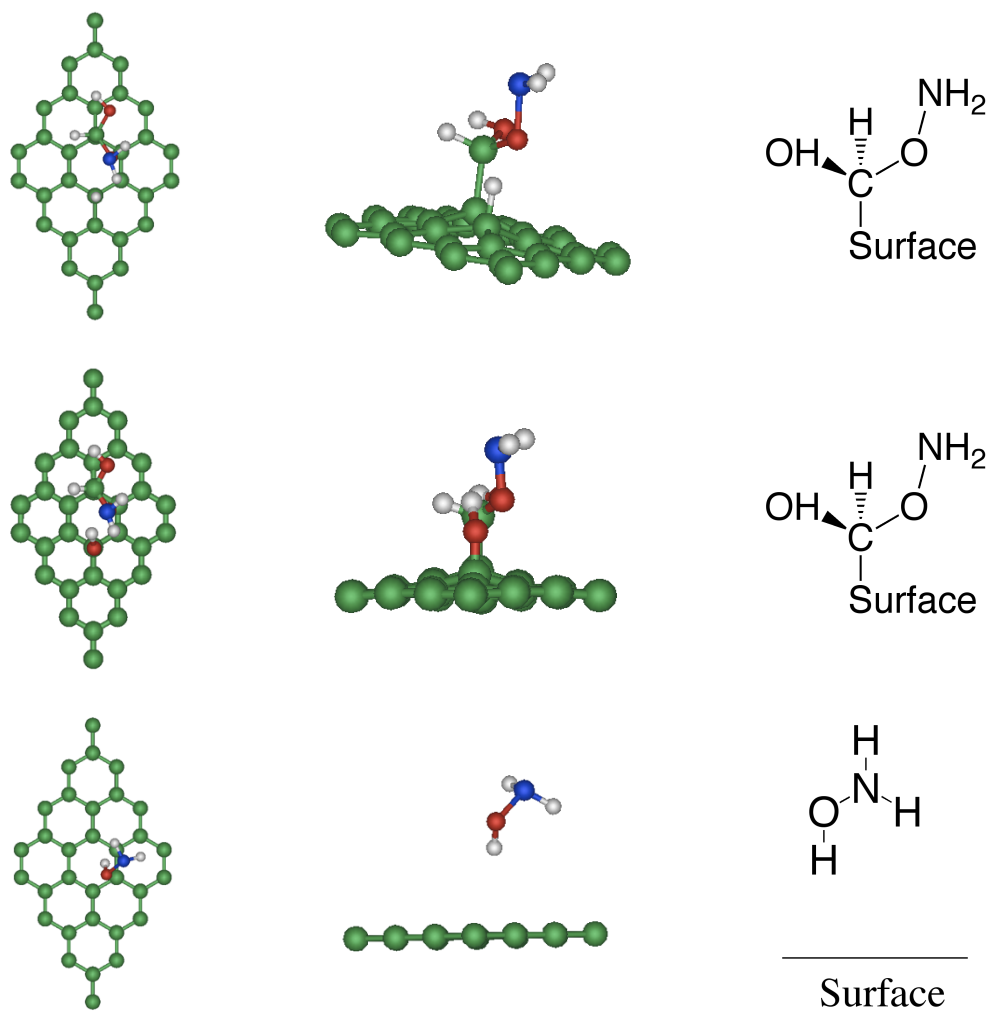
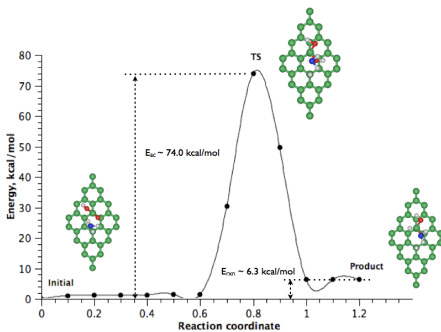


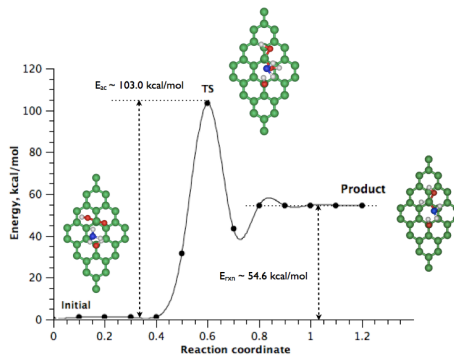
Figure 4.5. The final configuration for the NH₃/GO reaction: (top) NH₃ with the carboxyl group on Model 3; (middle) NH₃ with the carboxyl on Model 12; (bottom) NH₃ with the epoxy group on Model 13. The rows from left to right are the top, side and schematic views of the final configuration.

The NEB method with 13 images is adopted to calculate the reaction pathway, energy barrier and transition state for the NH₃ dissociation reaction on Models 3, 12 and 13. Since

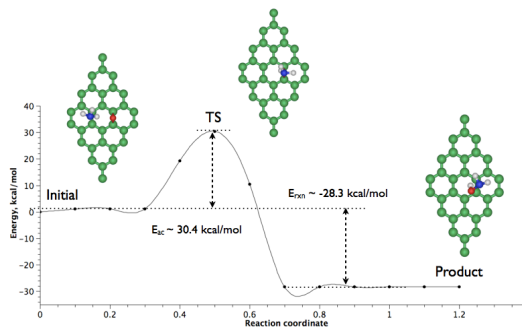
the NEB method requires the initial reactants and final products to be defined beforehand, the adsorbed NH_3 on each functional group is chosen as the reactant, and the final structures shown in Figure 4.5 as the products for the three different models. The total energy of the starting configuration is used as the reference.



(a) Model 3, Carboxyl group



(b) Model 12, carboxyl and hydroxyl groups



(c) Model 13, epoxy group

Figure 4.6. Activation energy barrier for the NH_3 dissociation on: (a) Model 3, GO with the carboxyl group; (b) Model 12, GO with the carboxyl and hydroxyl groups; (c) Model 13, GO with the epoxy group.

As shown in Figure 4.6, the NH_3 dissociation in Model 3 and 12 is endothermic, and the reaction energies are 6.3 kcal/mol and 54.6 kcal/mol, respectively. The dissociation reaction on the epoxy group in Model 13 is exothermic, -28.3 kcal/mol. It is worthwhile to point out that the reaction energy values here are different from the values we discussed in the beginning of this section. This is due to a different definition of reactants. Here for the NEB calculation, we use the configuration with NH_3 adsorbed on the functional group as the reactant, but in the previous part the gas-phase NH_3 and the GO model are treated as the two reactants. The transition state for Model 3 and 12 are similar, one N-H bond of the NH_3 molecule is broken and the NH_2 species forms a new bond with the oxygen atom of the carboxyl group. That same oxygen atom also forms a new O-H bond with the hydrogen atom dissociated from NH_3 . However, that O-H bond is broken later to form a C-H bond with the carbon atom of the carboxyl group. The reaction energy difference comes from the hydroxyl group in Model 12, where the O-H bond of the hydroxyl group is prolonged from 0.99 Å to 1.23 Å for the TS configuration. The steric effect of the hydroxyl group could also result in the increase of activation energy and the reaction energy. In the product of Model 12, the hydroxyl group is still connected to the basal surface, and the O-H bond is around 1.05 Å.

The formation of a hydroxylamine molecule in Model 13 is energy favorable, and the activation barrier of 30.4 kcal/mol is easy to overcome. Such interaction between NH_3 and the epoxy group is also observed in experiments and a reaction mechanism for NH_3 dissociation on the epoxy group is proposed in Figure 4.7.[\[13\]](#) From the DFT calculations here, we know that the proposed structure (d) is not stable. The amino group reacts with the hydroxyl group, and a hydroxylamine molecule is released as the reaction product.

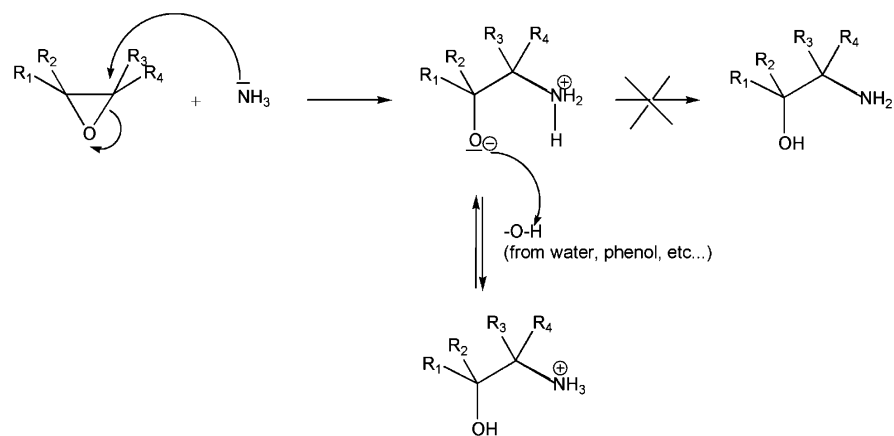


Figure 4.7. NH₃ dissociation on the epoxy group of GO: the reaction mechanism proposed in Ref.[13]

4.4. Conclusions

In this chapter, we have performed DFT calculations to study the interactions between H₂O and NH₃ with functional groups (carboxyl, hydroxyl, epoxy) on graphite oxide. The results show that H₂O does not dissociate on the functional groups, but forms a hydrogen bond with the oxygen atom from the three types of functional groups. The findings explain the experimental results[13] that water can screen the accessibility of carboxyl and epoxy groups for NH₃ adsorption and dissociation. Without the existence of water, NH₃ is found to dissociate on the carboxyl and epoxy groups. The NEB method has been applied to determine the reaction pathway, the energy barrier and the transition states of NH₃ dissociation. The NH₃ dissociation on the carboxyl group is found to be an endothermic process, but it is an exothermic reaction on the epoxy group and the activation energy is small. We also investigate different functional patterns of graphite oxide. Sulfonic groups are found to be unstable on the surface, and could probably exist at the edges of graphite oxide.

The single hexagonal cell of the graphene can host two functional groups. However, we observe the steric hindrance effect for NH_3 adsorption when there are two functional groups on the same hexagonal cell.

Together with the results from Chapter 3, we have gained the understanding that both the vacancy defect and the functional groups (the carboxyl and epoxy groups) on the graphene surface are active sites and can be used to decompose toxic gases. It seems to be a natural choice to produce graphite oxide materials, incorporating both the vacancy defect and the functional groups, to the maximum limit of their concentrations on the surface. However, we still lack a more detailed understanding of the realistic GO materials. For example, what will be the correlation effects from the two types of surface modification? What are the maximum concentrations for such surface modification? Can they react with each other to release other molecules, such as H_2O ? How stable are the GO materials if we use them at higher temperatures? Can we re-generate the active sites for many cycles in the real-life applications? In order to answer those concerns, we first need a GO model with both the vacancy defects and functional groups. This is the topic of Chapter 5.

CHAPTER 5

Realistic Graphene Oxide Models by Reactive Molecular Dynamics

Simulations

5.1. Introduction

Graphene oxide (GO) is attracting much research interest because it exhibits exceptional electrochemical, mechanical and optoelectronic properties, which makes it a promising candidate in batteries,[\[194, 195\]](#) field-effect transistors,[\[196, 197\]](#) nanocomposites[\[198\]](#) and biomedical applications.[\[199\]](#) It is also known that GO possesses catalytic potential.[\[200\]](#) For example, GO is reported to display a very high turnover frequency in Suzuki-Miyaura coupling reactions when it is impregnated with palladium nanoparticles.[\[201\]](#) Bielawski and co-workers report using GO as a heterogeneous catalyst to oxidize benzyl alcohol into benzoic acid.[\[202\]](#) Badosz and co-workers have conducted adsorption experiments and they observe the dissociation of ammonia, hydrogen sulfide and sulfur dioxide on oxygen-containing functional groups of GO materials.[\[203-205\]](#)

Despite those efforts, the catalytic potential of GO has not been extensively explored yet, due to the lack of a realistic atomic GO model. The chemistry of GO depends closely on the fabrication process and conditions. As a result, the amorphous feature of GO imposes challenges for determining a unique atomic model. Considerable efforts have been undertaken in the past decades to study GO structures. Models have been proposed and have gained success in explaining experimental and theoretical observations.[\[46, 175, 177\]](#) The

understanding of GO structures includes the possible species of functional groups, the range of functional group concentrations and their binding sites on the GO surface. For example, it is accepted now that the hydroxyl and epoxy groups are distributed on the basal plane, and the carboxyl and alkyl groups are located at the edges.[46] However, key information, including the type of functional group, the concentration and the distribution pattern with respect to a specific GO synthesis method, still remains unclear. Theoretical investigations on GO models, including the ones from the previous Chapters 3 and 4, usually focus on only one type of functional group. This is inadequate because functional groups, Stone-Wales defects, adatoms, and vacancy defects are observed for GO structures, and those sites have already demonstrated catalytic potential to some extent.

In this chapter a new procedure is introduced to generate realistic GO structures for theoretical calculations. We have learnt from the DFT calculations in Chapter 4 that functional groups are not stable if they are close to each other on the same hexagonal ring. In addition, based on the DFT calculations in Chapter 3, the products from the functional group interactions, usually in the form of small gas species such as H₂O, CO or CO₂, can further react with the basal surface and functional groups to create new defects/functional groups and other radical species, and thus initiate chain reactions. Starting from a graphene structure, we randomly functionalize the surface by a mixture of hydroxyl and epoxy groups. The concentration and the ratio of functional groups result in different pseudo GO models, where we observe the carboxyl, carbonyl, epoxy, hydroxyl groups, vacancy defects and other large carbon-oxygen rings. We then carry out ReaxFF reactive molecular dynamics (RMD) simulations to study the adsorption and dissociation of H₂S on those GO structures.

The chapter is organized as follows: Section 5.2 contains the computational details of the ReaxFF force field, the preparation of the GO model, the annealing process, and other RMD details. In Section 5.3, we discuss the thermal evolution of the GO structures in the RMD calculations. Once the realistic GO structures are available, temperature-programmed RMD calculations are performed to study the behaviour of H₂S and H₂S/H₂O mixtures on those GO structures at ambient condition. Finally, a summary is given in Section 5.4.

5.2. Computational Details

5.2.1. ReaxFF reactive force field

The ReaxFF method was developed in 2001 to study the hydrocarbon systems.[102] It is a first principles-based general bond-order dependent force field that provides an accurate description of bond breaking and bond forming. It has been demonstrated to be capable of describing the energies of surfaces, structures, and barriers of materials, including hydrocarbons, nitramines, metals and metal oxides. The fundamental difference between ReaxFF and other force fields is that ReaxFF does not need any connectivity input for the chemical bonds, but instead calculates the bond order directly from instantaneous interatomic distances which are updated continuously. Other features of ReaxFF have been summarized both in publications and on websites. It has been demonstrated in ReaxFF that, through an annealing process of GO, hydroxyl and epoxy groups on GO can be transformed into carbonyl, ether, pyran, furan and other oxygen-containing groups as well as vacancies and carbon ring defects.[206]

5.2.2. The GO Model

We use a 4.3 nm × 4 nm zigzag graphene sheet as the basal surface of GO, and apply a Monte Carlo scheme to randomly attach epoxy and hydroxyl groups to both sides of the graphene sheet. A simple geometry overlap criterion is chosen to make sure that the same hexagonal ring accommodates no more than two functional groups initially.

We study three functionalization concentrations: 10%, 20% or 30% of the total number of basal carbon atoms are functionalized by hydroxyl or epoxy groups. For each functionalization concentration, we test three combinations (2/3,1/1 and 3/2) of the hydroxyl and epoxy groups. There are a total of 9 initial GO structures prepared. The GO structure is centred in a 4.3 nm × 4 nm × 2.5nm box. Periodic boundary conditions are applied along the X, Y and Z directions. Figure 5.1 shows an example of one initial GO structure. For that structure, 30% of the carbon atoms are functionalized, among which 50% are functionalized by the hydroxyl groups and the other half by the epoxy groups. We herein use “ $a-(b:c)$ ” to name the GO structures, where a is the functionalization concentration, which has the value of 10%, 20% or 30%. “ $b:c$ ” stands for the ratio of the total numbers of hydroxyl ($N_{hydroxyl}$) and epoxy (N_{epoxy}) groups, that is, $b : c = N_{hydroxyl} : N_{epoxy}$.

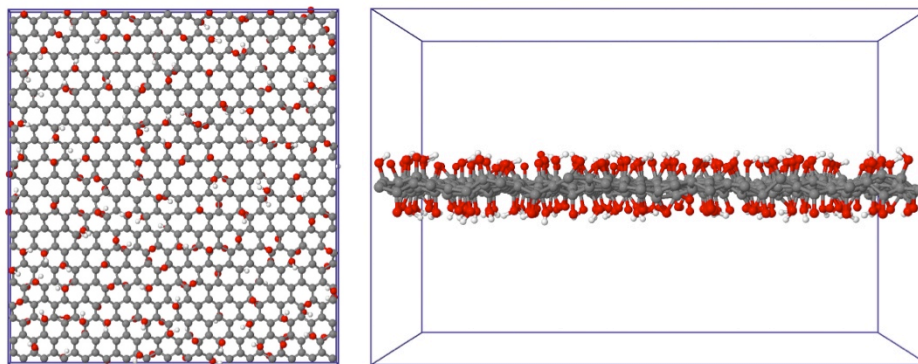


Figure 5.1. The front view (Left) and top view (Right) of a $4.3 \text{ nm} \times 4 \text{ nm} \times 2.5 \text{ nm}$ simulation box. The initial GO structure 30%-(1:1), where 30% of the basal carbon atoms are functionalized by the hydroxyl and epoxy groups in the ratio of 1:1, is placed in the center of the simulation box. Periodic boundary conditions are applied along X, Y and Z directions.

5.2.3. Temperature-Programmed RMD

While the functional groups are added to the surface according to simple geometry criteria, the initial GO model (I) is first relaxed at a low temperature 10 K, as shown in Figure 5.2, to fine tune the conformation of the functional groups. During the 25 ps RMD at 10 K, we observe the curvature change of the basal surface, but there is no chemical reaction between the functional groups or from the functional group/ basal surface interactions. The optimized structure (A) is then heated steadily from 10 K to 2010 K at a speed of 0.005 K/iteration. Along the heating-up path, we observe the release of CO and CO₂ molecules from the surface, and also the formation of defects on the basal surface. The high temperature (2010 K) is chosen so that we can observe the reactions that normally require a very long simulation at room temperatures. A 25-ps RMD is then followed to optimize the GO structure (B) at 2010 K. Many more small molecules (CO, CO₂, H₂O) are released from the surface. We are also

able to identify larger vacancy and other functional groups on the GO structure. After that, the GO structure (C) is cooled from 2010 K to 300 K at the same rate of 0.005 K/iteration. It is interesting to note that along this path, the gas-phase molecules can react with the GO structure to be part of the final structure (D). At last, a 25-ps RMD is performed to further optimize the GO structure (D). The final structure (F) from the annealing protocol is considered to be the optimized GO model, which can be used to remove H₂S or NH₃ by reactive adsorption. Longer simulations (up to 300 ps) have been performed to compare the structures (C). There is no significant structure difference observed, although the structures are not identical. A different rate of 0.05 K/iteration has also been tested for the heat-up (A to B) and cool-down (C to D) paths. It produces a similar final GO structure (F), compared with the one from the rate of 0.005 K/iteration. We thus conclude that the final GO structure (F) depends on the initial structure (I) and the cook-off temperature used. A test calculation for the cook-off temperature at 5000 K can break the GO structure into pieces along the B to C path.

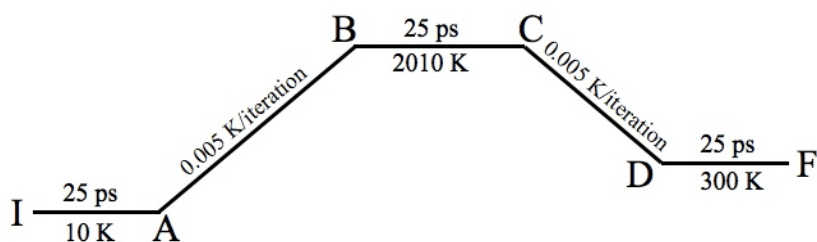


Figure 5.2. The annealing protocol of GO structure in RMD: “I” and “F” are the initial and final GO configurations, respectively. “A”, “B”, “C” and “D” are the intermediate GO configurations along the path. A time step of 0.25 fs is used throughout the calculations.

All RMD calculations are performed in a canonical molecule (N), volume (V) and temperature (T) ensemble with the Verlet integrator of a timestep of 0.25 fs. The temperature is controlled by the Berendsen thermostat method with a damping constant of 100 fs. The velocities are initiated using a Boltzmann distribution. A bond-order cutoff of 20% of the original bond length is used to identify the connectivities and the molecular species, and also to monitor the structural evolution of GO as a function of time. The RMD calculations are performed using the ReaxFF library that is implemented in the LAMMPS software package.[108] An example of RMD calculation in LAMMPS is provided in Appendix B.

5.3. Results and Discussion

5.3.1. Structural evolution of GO model

The local arrangement of hydroxyl and epoxy groups on the GO surface has been a subject of discussion for a long time. The preferential alignment of the epoxy groups along a zigzag direction of the graphene lattice has been observed from first principles calculations.[207] This observed structure was later confirmed by the non-contact atomic force microscopic (NC-AFM) experiments of Fujii and Enoki.[208] Using density functional theory (DFT) calculations, Lahaye and co-workers found that a hydroxyl group accompanies an epoxy group at the opposite side of the same hexagonal ring.[178] The result agrees well with experimental results by Cai and co-workers.[209] However, DFT calculations are computationally expensive and can only effectively deal with the GO structure of a few tens of atoms. It is thus not practical to use DFT calculations to study a realistic GO structure with all kinds of functional groups and defects.

Here in this chapter, the GO structures are generated from the RMD calculations using the annealing protocol discussed in section 5.2.3, and are the final optimized structures (F). The initial structures (I) are functionalized by an equal number of hydroxyl and epoxy groups. However, along the annealing path, most of the hydroxyl groups are released from the GO surface in the form of H₂O molecules, when the temperature is above 1000 K. Epoxy groups are the dominant groups for the final GO structure (F). But they react with saturated *sp*³ basal carbon atoms at high temperatures (> 1500 K) and create vacancies when the products (CO₂ and CO) are released from the GO surface. Furthermore, such reaction is only observed when the initial functionalization concentration is high (20% or 30%). There is no vacancy created for the three cases 10%-(1:1), 10%-(2:3) and 10%-(3:2), where only 10% of the basal carbon atoms are functionalized. On the other hand, for one functionalization concentration, the different combinations investigated (1:1, 2:3 or 3:2 for the number of hydroxyl and epoxy groups) do not change the final structure (F).

We show three final GO structures (F) in Figure 5.3, namely, 10%-(1:1), 20%-(1:1) and 30%-(1:1). Figure 5.3 also provides a list of the new functional patterns, such as vacancies (Figure 5.3 (b-1)), large carbon rings (Figure 5.3 (b-2), (c-3)), carboxyl group (Figure 5.3 (c-1)) and the preferential alignment of epoxy groups along the zigzag direction (Figure 5.3 (c-2)). For the 10%-(1:1) GO structure, besides the remaining hydroxyl and epoxy groups, we find new functional groups, for example, the pair of meta-epoxy groups (a-1), and the pair of carbonyls (a-2). When the initial functional concentration is increased to 20%, we identify the following functionalization patterns: the single vacancy with a pair of carbonyls (b-1), the large carbon ring structure (b-2), and the aldehyde group (b-3). As for

the 30%-(1:1) GO structure, we observe the formation of the carboxyl group (c-1), the preferential alignment of the epoxy groups along the zigzag direction (c-2), and also a furan structure (c-3).

It is accepted that the transformation of the functional groups requires high concentrations of the functional groups and high temperatures.[206] This can be explained by the population analysis shown in Figure 5.4. For the 30%-(1:1) GO structure, the transformations of the functional groups and the release of reaction products begin at around 1000 K. But it requires a higher temperature (~ 1500 K) to observe the transformations and chemical reactions for the 10%-(1:1) and 20%-(1:1) GO structures.

Figure 5.4 also shows that, for the 30%-(1:1) GO structure, the total number of molecules is increasing along the high temperature relaxation path, B to C in Figure 5.2. It means that more and more reaction products are being released from the GO structure. We do not observe the same phenomena for the 10%-(1:1) or 20%-(1:1) GO structures. It also agrees with the results in Figure 5.3 that a higher functional density of GO structure can result in a more dramatic atomic rearrangement and more new functional groups and defects. A close examination of the reaction products reveals that the formation of carboxyl group and the release of O₂, CO₂ and CO molecules are only observed for the 30%-(1:1) GO structure where hydroxyl and epoxy sites are in close proximity and can react with each other.

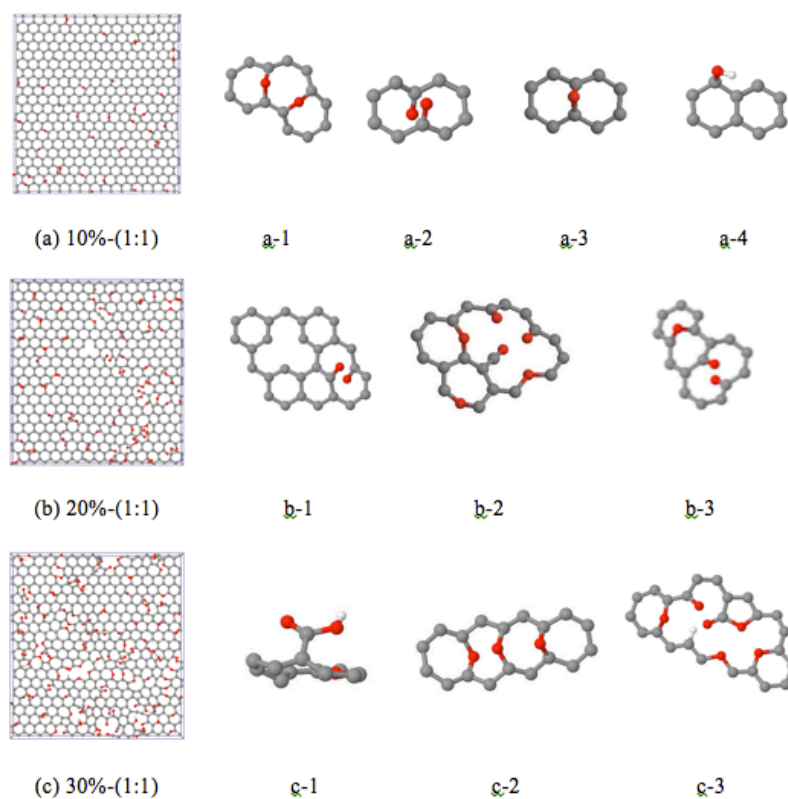


Figure 5.3. Configurations of GO structures with the functional groups and local defects: (a), (b) and (c) are the final configurations of GO where 10%, 20% and 30% of the basal carbon atoms are functionalized by the hydroxyl and epoxy groups in the ratio of 1:1, respectively. Functional groups and carbon arrangements formed in the configurations of (a): a pair of meta-epoxy groups (a-1), a pair of carbonyls (a-2), an epoxy group (a-3), a hydroxyl group (a-4); (b): a single vacancy and a pair of carbonyls (b-1), a large carbon ring (b-2), an aldehyde group (b-3); (c): a carboxyl group (c-1), a preferential alignment of epoxy groups along the zigzag direction (c-2), a furan (c-3). The color codes are: carbon-grey, oxygen-red, hydrogen-white.

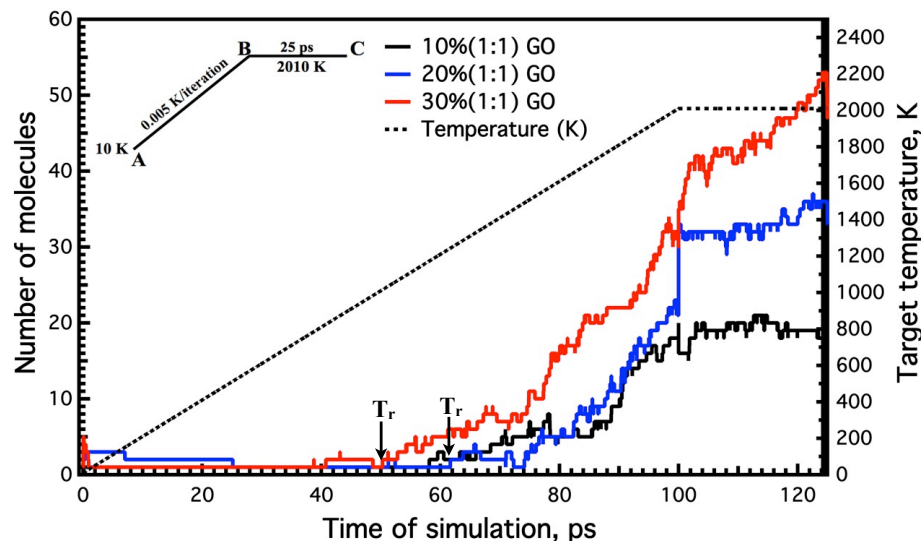


Figure 5.4. Population analysis of the GO structures: the number of molecules along the cook-off path (A to B) and high temperature relaxation path (B to C) for different functional group concentrations: 10% (black line); 20% (blue line); 30% (red line). T_r is the temperature when we start to observe the release of reaction products. The black dashed line is the targeted temperature of the RMD calculation.

5.3.2. H₂S dissociation on the GO structures

We learned from the DFT calculations in Chapters 3 and 4 that H₂S and NH₃ can decompose on the vacancy defect or functional groups (carboxyl and epoxy) of GO. Here, we use the realistic GO structure prepared in Section 5.3.1 to study the H₂S interaction by the temperature-programmed RMD calculations. The 30%-(1:1) GO structure is chosen because, as shown in the previous section, the higher initial density of functional groups can result in a more dramatic atomic rearrangement, and thus provides more active sites for H₂S molecules. The 30%-(1:1) GO structure incorporates vacancy defects, epoxy, carboxyl as well as other functional groups. We prepare the simulation box by removing the gas-phase molecules and

free radicals from the final RMD box of the 30%-(1:1) structure in Section 5.2.1. Then 100 H₂S molecules are randomly added to both sides of the GO structure in the simulation box. The simulation box is heated in the NVT ensemble from 300K to 2300K at the rate of 0.005 K per iteration. The time step is 0.25 fs.

We observe that H₂S molecules can decompose on the functional groups of the 30%-(1:1) GO structure. From the population analysis in Figure 5.5, we identify that the chemisorption of H₂S starts around 470 K, but the dissociation of H₂S into HS species does not happen until a high temperature of about 1460 K. There is not any atomic S observed for H₂S dissociation because both the direct decomposition of H₂S into S and the two-step decomposition via HS require a large energy barrier to be surmounted. The HS species are found to form stable bonds with carbonyl groups, but they do not react with hydroxyl or epoxy groups on the GO surface.

The release of H₂O, CO₂ and CO molecules starts at 800 K, 1850 K and 1900 K, respectively. H₂O is the reaction product from the interaction of hydroxyl and epoxy groups. The calculated result agrees with the literature that the hydroxyl group desorption requires a lower temperature. The release of CO and CO₂ were attributed to the atomic rearrangement of GO and the reactions between hydroxyl and epoxy groups. It generally requires a dense pattern of hydroxyl and epoxy sites.

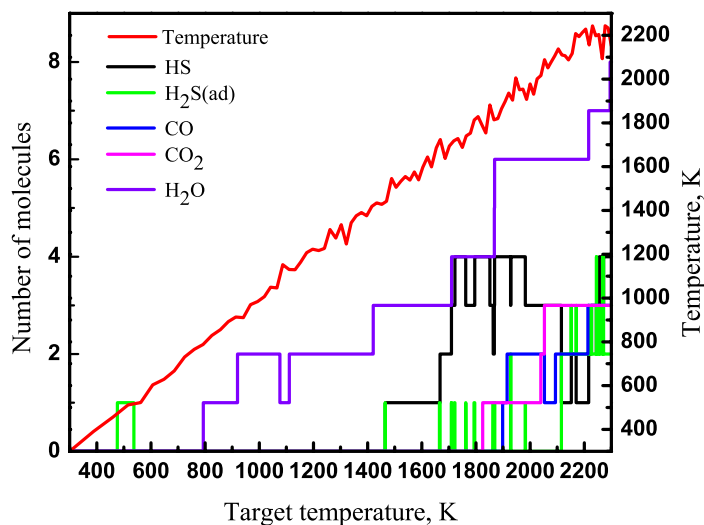


Figure 5.5. The population analysis of H₂S chemisorption and dissociation on the 30%-(1:1) GO structure. The color codes are: temperature (K)-red, HS-black, chemisorb H₂S-geen, CO-blue, CO₂-magenta, H₂O-purple. The box contains 100 H₂S molecules at the beginning of the calculation.

5.3.3. Competitive adsorption of the H₂S/H₂O mixtures on GO

The temperature-programmed RMD confirms that GO has a catalytic potential for the H₂S dissociation when the temperature is above 1500 K. On the other hand, H₂O, as a major reaction product, is released from the GO surface starting at around 800 K. These H₂O molecules can compete with H₂S for the active sites on the GO structure. Using the three GO structures from Figure 5.3, we studied the competitive adsorption of two H₂S/H₂O mixtures, where one is made up of 100 H₂S and 50 H₂O molecules, and the other has 100 H₂S and 100 H₂O. The simulation box is similar to the one in section 5.2.2. The GO structure is put in the centre of the simulation box, and H₂S and H₂O molecules are randomly added to the simulation box. The RMD calculation is performed in the NVT ensemble, where the

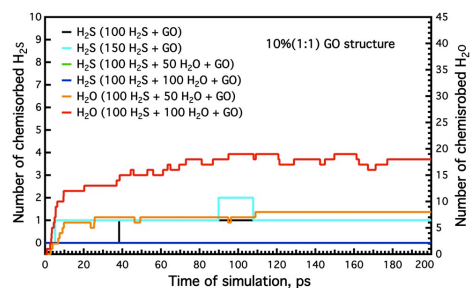
temperature is 300 K. A time step of 0.25 fs is used for the 200 ps trajectory. For comparison, we also study systems where only the GO structures and H₂S molecules are present. Table (5-1) has a summary of the 12 systems for the RMD calculations.

Table 5-1. A summary of the 12 systems with the number of molecules.

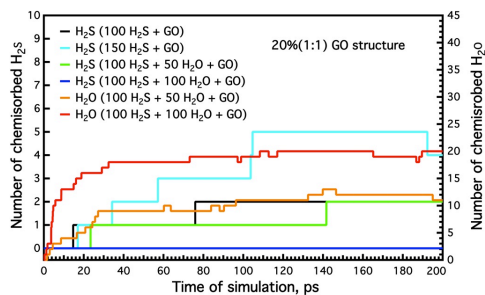
	H ₂ O/H ₂ S		H ₂ S	
10%-(1:1)	50/100	100/100	50	100
20%-(1:1)	50/100	100/100	50	100
30%-(1:1)	50/100	100/100	50	100

For the gas-phase H₂S molecules, the number of chemisorbed H₂S increased as the functional group coverage of the GO structures increased from 10% to 30%. As we can see from the population analysis in Figure 5.6, the number of chemisorbed H₂S molecules are 1, 2, and 6, for the 10%-(1:1), 20%-(1:1) and 30%-(1:1) GO structures, respectively. The larger density of the gas-phase H₂S molecules results in more H₂S molecules chemisorbed, as shown by the difference between the black and cyan lines in Figure 5.6(b). This is explained as follows: for the 10%-(1:1) GO structure, the number of active sites is limited, and once those sites are occupied, no more H₂S molecules can get adsorbed. For the 30%-(1:1) GO structure, as discussed above, the dramatic atomic rearrangement allows for the easier adsorption of H₂S molecules, so it can reach adsorption saturation even at the lower H₂S density. But for the 20%-(1:1) GO structure, more H₂S molecules are adsorbed since there are more H₂S molecules in the simulation box.

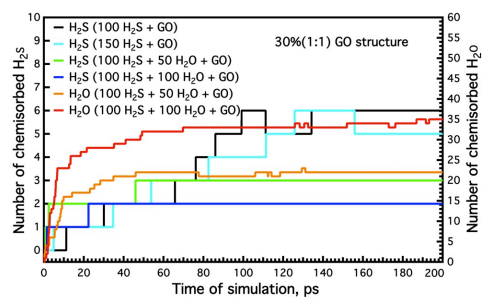
It is also obvious that H_2O can easily adsorb on the GO structures. When the functional group coverage is increased from 10% to 30%, the number of chemisorbed H_2O changes from 8 to 22 for the 50/100 $\text{H}_2\text{O}/\text{H}_2\text{S}$ mixture, and 18 to 35 for the 100/100 $\text{H}_2\text{O}/\text{H}_2\text{S}$ mixture. On the other hand, the number of adsorbed H_2S molecules decreases due to the existence of the H_2O molecules. For the 50/100 $\text{H}_2\text{O}/\text{H}_2\text{S}$ mixture, the number of chemisorbed H_2S changes from 6 to 3 on the 30%-(1:1) GO structure. There are only 1 or 2 H_2S molecules adsorbed on the other two GO structures, so it is not easy to explain the trend. The increase in H_2O molecules can further block the adsorptive sites from H_2S molecules. For the 100/100 $\text{H}_2\text{O}/\text{H}_2\text{S}$ mixture, we do not observe any H_2S chemisorption on the 10%-(1:1) or 20%-(1:1) GO structures. For the 30% GO structure, there are 2 H_2S molecules adsorbed, while the number is 6 for the corresponding case where we only have H_2S in the gas phase.



(a) 10%-(1:1) GO



(b) 20%-(1:1) GO



(c) 30%-(1:1) GO

Figure 5.6. Population analysis for H₂S (left axis) and H₂O (right axis) chemisorption on GO structures: (a) 10%-(1:1); (b) 20%-(1:1); (c) 30%-(1:1). For the 10%-(1:1) case, the green and blue lines coincide at $n_{\text{H}_2\text{S}}=0$.

It is interesting to note that we do not observe any dissociation of H₂S or H₂O on the vacancy defects of the GO structures. This is probably due to the steric hindrance effects

from other functional groups. But it may be simply that the calculation is at 300 K, so the H₂S molecule does not have enough kinetic energy to overcome the reaction energy barrier. The third explanation is that we may need to re-train the ReaxFF parameters for the vacancy defects.

5.4. Conclusions

In this chapter, we use ReaxFF and the temperature-programmed MD simulations to generate realistic GO structures. By adding hydroxyl and epoxy groups to the graphene and by controlling the functional group concentration, we can generate GO structures with other functional patterns and defects, such as the pair of meta-epoxy groups, the pair of carbonyls, the single vacancy with a pair of carbonyls, the large carbon ring, the aldehyde group, the carboxyl group, the preferential alignment of epoxy groups along the zigzag direction and so on. Those new functional groups are confirmed by experiments or theoretical calculations.[\[182, 206\]](#) This temperature-programmed RMD opens a new door to prepare the amorphous atomic GO model for theoretical calculations.

We further study the adsorption and dissociation of H₂S and H₂O/H₂S mixtures on the generated GO structures at 300 K. H₂S is observed to react with the functional groups and H₂O, CO₂ and CO molecules are released from the surface as reaction productions. Similar to the results from Chapter 3, for the H₂O/H₂S mixture, H₂O molecules are preferentially adsorbed to the GO structure, and thus block the active sites for H₂S adsorption.

CHAPTER 6

Thermal Stability of CuBTC MOF: Reactive Molecular Dynamics

Simulations

6.1. Introduction

Metal-organic framework (MOF) is a new class of porous organic/inorganic hybrid materials that exhibits a high degree of crystallinity and a large surface area, allowing potential applications for gas sorption/separation,[\[210\]](#) size-/shape-selective catalysis,[\[211\]](#) drug delivery[\[212\]](#) and toxic gas removal.[\[24\]](#) Among various MOFs, the 3-dimensional copper-based MOF, CuBTC (BTC=1,3,5-benzenetricarboxylate), also known as HKUST-1,[\[213\]](#) has received a great deal of interest recently. In addition to general interest in its application in adsorption and separations, recent studies have shown that the unsaturated copper sites in CuBTC are available for chemisorption and catalytic reactions, such as the dissociation of ammonia[\[36\]](#) and hydrogen sulfide.[\[205\]](#)

Most previous theoretical and simulation studies involving CuBTC have been concerned with its application in adsorption and separation processes, for example, the adsorption of water,[\[214-216\]](#) the separations of alkane mixtures,[\[217\]](#) CO₂/CH₄,[\[218, 219\]](#) H₂/CH₄,[\[220\]](#) CO/CO₂[\[221\]](#) and olefin/paraffin[\[222\]](#) systems. However, questions remain concerning the chemical, thermal and mechanical stability of these framework materials, and on the validity of rigid atomic models of CuBTC that have been widely used in the simulation studies of adsorption.

The application of MOFs demands reasonable structural stability to avert excessive structural distortion, framework collapse and temperature/pressure-induced amorphization.[223, 224] However, researchers have observed the breathing effect, the distortion and decomposition of CuBTC in many applications.[225] Gul-E-Noor *et al.* used ^1H and ^{13}C solid-state NMR spectroscopy to observe the structural changes and framework decomposition of CuBTC due to water adsorption.[226] Allendorf *et al.*[227] demonstrated the concept of molecular detection (H_2O , CO_2 , MeOH and EtOH) by measuring the adsorption-induced distortion of CuBTC. Petit *et al.* reported the dissociation of ammonia and hydrogen sulfide in CuBTC.[205, 228] The ammonia vapour removal by CuBTC is also reported by ^1H MAS NMR experiments of Peterson *et al.* [229]

Those experimental observations imply that the rigid atomic model of CuBTC, which is widely used in the literature to compute adsorption isotherms, is not a proper choice when the breathing effect is not negligible.[225, 227, 230] In addition, we need a force field, which is capable of describing both the flexible nature of the CuBTC framework and the adsorbate-adsorbate and adsorbate-CuBTC interactions for chemisorption and reaction. Much attention has recently been focused on a proper force field for CuBTC.[231, 232] Amirjalayer *et al.* developed a first-principles derived force field for CuBTC and successfully predicted its topology preference.[233] Zhao *et al.* retrained the angle bending and torsion angle parameters of CuBTC against density functional theory (DFT) calculations, and the new force field reproduced both thermal expansion and vibrational properties of CuBTC.[234] To the best of our knowledge, no force field has been proposed that can account for the

flexibility of the framework and describe simultaneously the chemisorption and chemical reaction in CuBTC.

In this chapter we report a ReaxFF reactive molecular dynamics (RMD) simulation of thermal stability of CuBTC. We show that CuBTC has a reasonable degree of thermal stability up to 550 K but decomposes at higher temperatures. The chapter is organized as follows: Section 6.2 provides a brief introduction to the ReaxFF force field, the description of the CuBTC model and the characteristics of the RMD simulation; in Section 6.3 we report the calculation results and discuss the thermal stability of CuBTC for the temperature range of 300 K to 1100 K. We observe a structural transition at medium temperatures (> 600 K) and the collapse of CuBTC framework at high temperature (1100 K). Finally, a summary is given in Section 6.4.

6.2. Computational Details

6.2.1. ReaxFF reactive force field

ReaxFF is a first principles-based bond-order dependent force field that provides an accurate description of bond breaking and bond forming.[\[102\]](#) It has been demonstrated to be capable of describing the structures, energy surfaces, and reaction barriers of materials, including hydrocarbons,[\[51, 235\]](#) nitramines,[\[236, 237\]](#) metals[\[238-240\]](#) and metal oxides.[\[241, 242\]](#) The fundamental difference between ReaxFF and other force fields is that ReaxFF does not need any connectivity input for the chemical bonds, but instead calculates the bond order directly from instantaneous interatomic distances which are updated continuously. The electrostatic and van der Waals interactions are also calculated between every atom pair

during the simulation. To enable the description of CuBTC structure, we combined the Cu/O/H parameters of van Duin *et al.* [243] with the glycine ReaxFF parameters published recently.[235] These force fields are sharing O/H parameters and use exactly the same potential functions, making integration of these parameter sets relatively straightforward. We do not further optimize bond parameters of C/Cu pairs, since such bonds are not expected to form in the oxygen-rich environment of the simulations. The non-bonded C/Cu interactions were obtained from standard combining rules.

6.2.2. RMD simulation

The initial coordinates of CuBTC were obtained from the x-ray powder diffraction (XRPD) results of Williams *et al.*[213] Since there were water molecules coordinated to copper sites in the as-synthesized form, we manually removed those water molecule coordinates to get the dehydrated CuBTC geometry. The coordinated water can also be easily removed in experiments, for example by heating to 373 K in air. The periodic cubic simulation box was made up of a $1 \times 1 \times 1$ unit cell of the dehydrated CuBTC (molecular formula: $\text{Cu}_{48}\text{C}_{288}\text{O}_{192}\text{H}_{96}$). All calculations were performed in an isothermal-isobaric (NPT) ensemble with Verlet integrator with a time step of 0.25 fs. The pressure and temperature were controlled by the Berendsen barostatting and thermostatting methods, with damping constants of 2500 fs and 100 fs, respectively. Velocities were initiated using a Boltzmann distribution. A bond-order cutoff of 20% of the original bond length was used to identify the connectivities and the molecular species, and to monitor the structural evolution of CuBTC

as a function of simulation time. A 300 ps trajectory was collected every 50 fs to analyse the results of each RMD calculation.

A previous experimental investigation[213] of CuBTC thermal stability found two results: (1) CuBTC is stable up to 513 K; (2) thermal gravimetric analysis (TGA) indicated the release of CO₂ when CuBTC is heated from 523 K to 673 K, and the formation of CuO and glassy carbon when CuBTC is further heated to 1073 K. In accordance with the experimental observations, we chose the following two sets of temperatures: (a) 9 temperatures, increased at a step of 100 K from 300 K, that is, T = 300, 400, 500, 600, 700, 800, 900, 1000 and 1100 K, to study the thermal stability and the new species produced by the structure collapse; (b) 20 temperatures, increased at a step of 5 K from 505 K, that is, T = 505, 510, 515 ... 585, 590 and 595 K, to determine the collapse temperature of the dehydrated CuBTC.

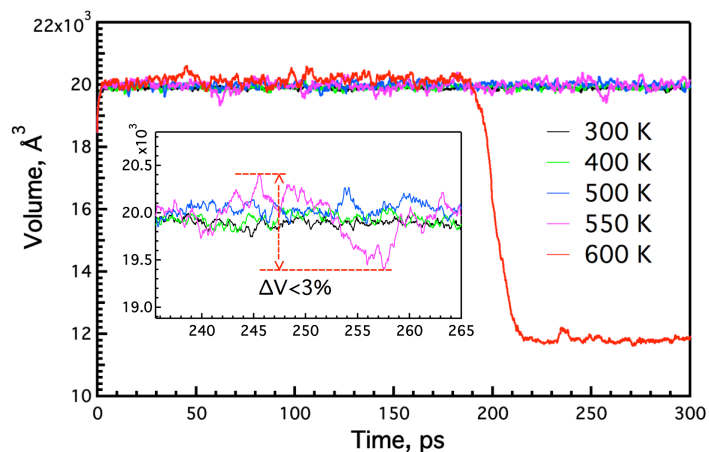
6.3. Results and Discussion

6.3.1. Volume evolution of CuBTC framework

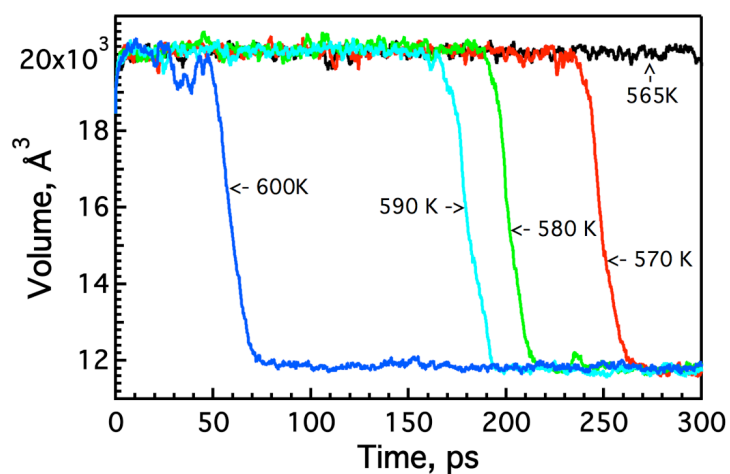
Figure 6.1(a) shows the volume of the CuBTC framework as a function of simulation time at T = 300, 400, 500, 550 and 600 K. We observed that the CuBTC framework is thermally stable up to 550 K and the structure is collapsed at 600 K. At the beginning of the simulation, the volume expanded from the initial value of 18280 Å³. This is because the dehydrated CuBTC model was prepared by removing the coordinated water molecules from the hydrated CuBTC framework. When the simulation began, the coordinates were relaxed from the hydrated atomic positions to the dehydrated ones. Figure 6.1(a) also demonstrated that the

volume was oscillating with larger amplitude when the temperature increased from 300 K to 550 K. However, even the largest fluctuation at 550 K was within 3% of the equilibrium volume of CuBTC framework, see the insertion plot in Figure 6.1(a). Many MOFs exhibit adsorbate-induced structural flexibility and the unit cell dimensions of some MOFs are reported to vary by as much as 10% when molecules are adsorbed within the pores.[\[244\]](#)

By the second temperature set, we determined the collapse temperature for the dehydrated CuBTC framework in Figure 6.1(b). For clarity, the temperatures below 565 K, where the dehydrated CuBTC framework is thermally stable, are not shown. We ran longer calculations (up to 1.5 ns) to make sure the collapse does not occur at a later stage for those temperatures. The results demonstrated that the dehydrated CuBTC framework starts to collapse at around 570 K, and we observed the collapse at all other higher temperatures. The result is in close agreement with the experimental result,[\[213\]](#) where they found the dehydrated CuBTC framework is stable up to 513 K. The coordinated water molecules in the experiments can explain the collapse temperature difference, and it also implies that the dehydrated CuBTC framework is thermally more stable.



(a)



(b)

Figure 6.1. The volume evolution of CuBTC framework at: (a) T=300, 400, 550, and 600 K; (b) T = 565, 570, 580, 590 and 600 K.

When the temperature was increased above 600 K, as shown in Figure 6.2, there were unusual volume changes, indicating that the CuBTC framework could not retain its crystal structure and was not thermally stable under these temperatures. Based on the plots in Figure 6.2, we divided these temperatures into three categories: (1) 600 K and 700 K, where we

observed a smooth volume transition. At 700 K, CuBTC retained the volume size for the first 75 ps simulation, and then started to shrink between 75 ps and 110 ps. The final volume was 40% less than the equilibrium value of the dehydrated framework. The structure snapshots in Figure 6.3 showed that at 75 ps CuBTC still preserved the crystal structure with channels of about 9.0 Å in diameter surrounded by tetrahedral pockets of about 3.5 Å in diameter. Those channels and micropore structures were destroyed after the volume transition brought CuBTC to an amorphous phase. The transition was delayed until 185 ps at 600 K, but the two cases shared all the other characteristics such as the final structure and volume size. (2) 800, 900, 1000 K, where CuBTC framework started to shrink immediately when the simulation began. Though a longer simulation was needed to reach the equilibrium structure, we may safely conclude from Figure 6.2 that the final volume would be around 13400 Å³. (3) 1100 K, where a random change of volume was observed along the simulation, indicating a complete collapse of CuBTC framework.

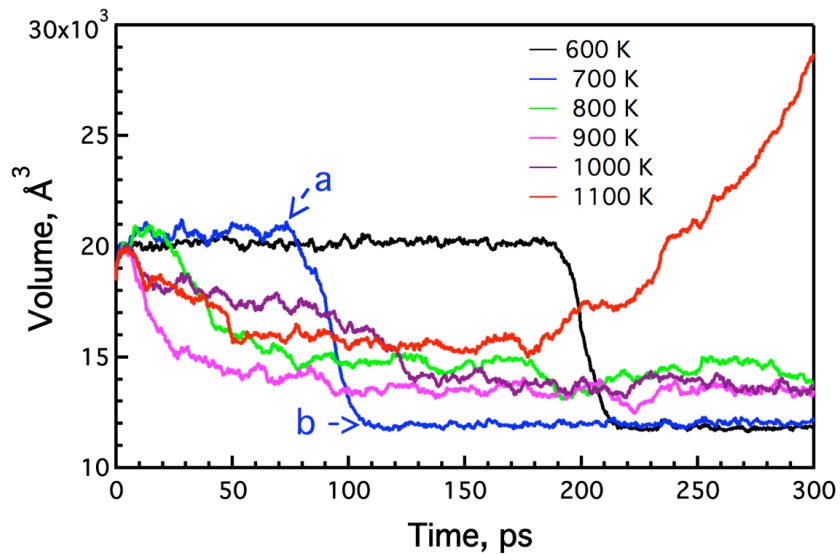


Figure 6.2. The volume evolution of CuBTC at the investigated high temperatures: $T = 600$, 700 , 800 , 900 , 1000 , and 1100 K.

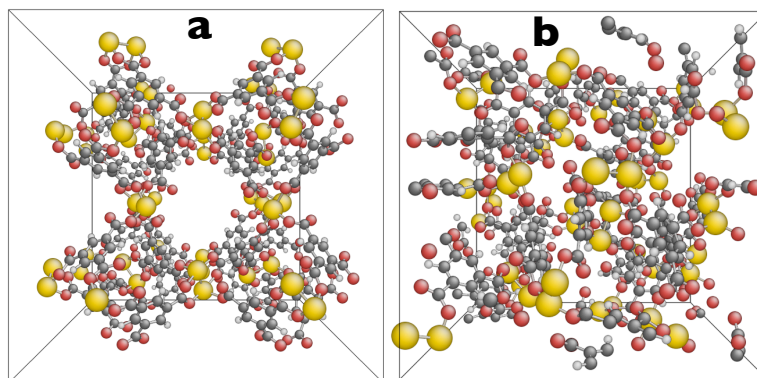


Figure 6.3. Structure snapshot of CuBTC framework at 700 K: image (a) and image (b) represent the two configurations at $t=75$ ps and 110 ps, respectively. Color codes are: yellow-Copper, grey-Carbon, red-Oxygen, and white-Hydrogen.

6.3.2. Decomposition of CuBTC framework

A population analysis was performed to monitor the possible decomposition of CuBTC framework at the investigated temperatures. There was no decomposition observed at the

lower temperatures of 300, 400, 500 and 550 K. The CuBTC framework retained both the crystal structure and the channels and micropores. At 600 K and 700 K, despite the volume size transition, we did not observe any molecule released from the framework. CuBTC retained the molecular formula of $\text{Cu}_{48}\text{C}_{288}\text{O}_{192}\text{H}_{96}$ although it lost the regular distribution of the channels and micropores.

The framework was not stable when the temperature was above 800 K. At 800 K, we observed the release of one CO_2 molecule at around 100 ps. The release of the atomic carbon and CO molecules was also identified in the later part of the simulation. As shown in Figure 6.4, the atomic carbon and CO_2 molecules were not stable and they reacted back and forth with the CuBTC framework. Compared with them, CO molecules were more stable once they were released into the gas phase. This is in agreement with the difference in the reactivity of the two species. We observed the same products but slightly higher concentrations at 900 K and 1000 K. It is worth pointing out that thermal gravimetric analysis (TGA) indicated that CuBTC gave a step-wise weight loss by releasing by-products: H_2O (295K to 393K); CO_2 (523 K to 673 K); a mixture of CuO and glassy carbon (above 1023 K). The main by-product from the simulations here is, however, carbon monoxide. The discrepancy is expected since CO is often a kinetic product, while CO_2 is the thermodynamic product. Given the relatively short duration of 300 ps and the high thermal stress, we expect the kinetic product to be prevalent in such ReaxFF simulations. If we would perform a slower heat-up simulation the CO_2/CO ratio will probably move towards the thermodynamic ratio. The force fields employed here were tested for carbon monoxide and carbon dioxide, and as such should not have a bias towards CO.

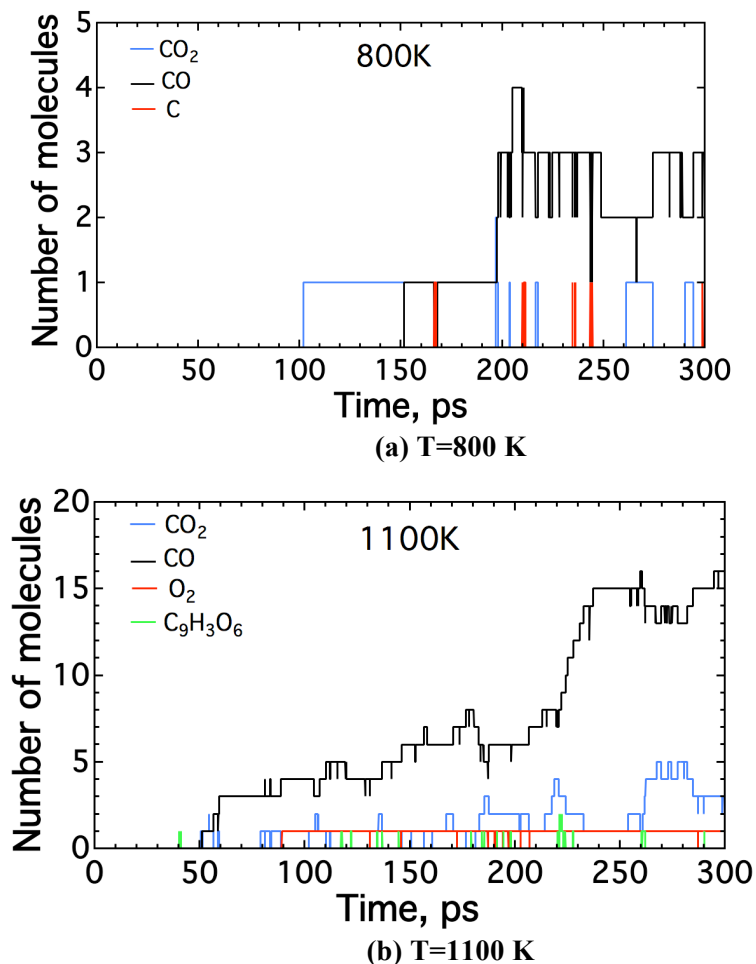


Figure 6.4. Population analysis of major species released from CuBTC framework: (a) T= 800 K; (b) T=1100 K.

At 1100 K, we identified the release of 1,3,5-benzenetricarboxylate ($C_6H_3(CO_2)_3$, BTC) molecule at around 40 ps. The concentration was low, less than 3 molecules during the 300 ps simulation. But it demonstrated that the bond between the copper atom and the organic linker (BTC) were not stable at high temperature. The breaking of copper and BTC bond was also observed by Petit *et al.*[36] when they performed dynamic adsorption experiments of ammonia on graphite oxide/ CuBTC nanocomposites at room temperature. Peterson *et al.*

also observed the decomposition of CuBTC upon ammonia adsorption at room temperature, and they identified the existence of $(\text{NH}_4)_3\text{BTC}$ from the ^1H MAS NMR measurement.[229] Besides the release of $\text{C}_9\text{H}_3\text{O}_6$ from the framework, we also observed CO_2 , CO and O_2 as the decomposition products at 1100 K. The concentration of CO molecules was much larger than the ones at 800 K, 900 K, and 1000 K, indicating the complete collapse of CuBTC framework and the release of BTC units.

6.3.3. Cu-Cu Radial distribution function of CuBTC framework

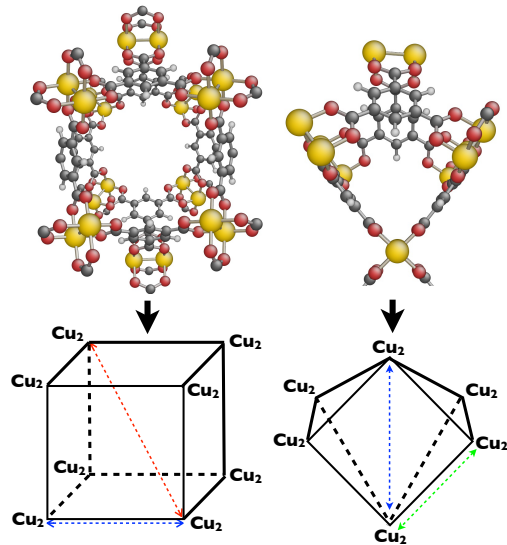
The radial distribution function (RDF), $g(r)$, also known as the pair correlation function, is a useful tool to extract structural information from molecular simulation trajectories. It gives the density probability for an atom to have a neighbour at a given distance. It is known that the CuBTC framework comprises channels of about 9.0 Å in diameter surrounded by tetrahedral pockets of about 3.5 Å diameter. In Figure 6.5 we show (a) typical pairs of Cu dimer and (b) the Cu-Cu radial distribution functions obtained from the 300 ps RMD simulation of CuBTC framework at 300, 700, and 1100 K. The three temperatures represent low, medium and high temperatures. As discussed in Section 3.1, CuBTC framework demonstrated different behaviour under those temperatures. The coordination number distribution was also provided in Figure 6.5(b).

As shown in Figure 6.5(b), the Cu dimer RDF had a peak at a Cu-Cu distance of 2.65 Å for all three temperatures. It represented the bond length of 2.65 Å of the Cu dimer and was in good agreement with the experimental measurement of 2.63 Å. It also implied the stability of the Cu dimers up to 1100 K.

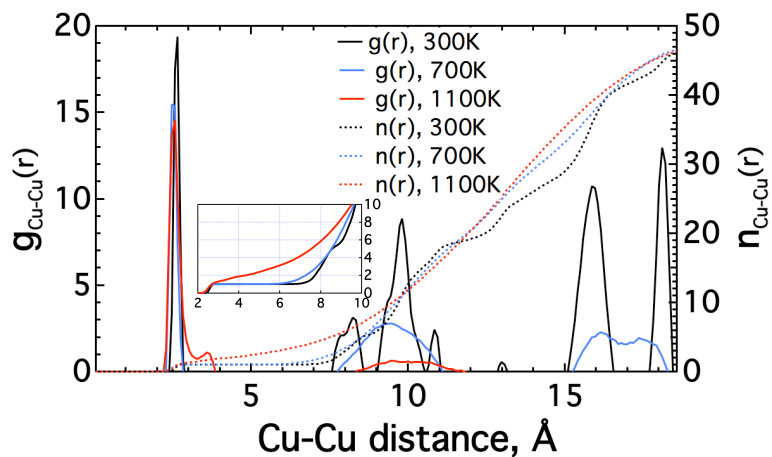
At 300 K, the RDF plot had other peaks. The peaks at 8.25 Å, 9.82 Å and 10.85 Å correspond to the tetrahedral pocket structure, and the ones at 15.88 Å and 9.82 Å represent the size of the main channel. The peak at 13.00 Å is much lower than the other ones. This is probably due to the fluctuation of the CuBTC framework, and results from averaging the peak height over the 300 ps simulation.

At 700 K and 1100 K, we observed significant changes to the peaks around $r = 10.00$ Å and 15.00 Å. They became broader but lower than the corresponding ones at 300 K. Thus the CuBTC framework lost part of the correlation between remote pairs of Cu dimers. At 1100 K, there were no peaks at 9.82 Å or 15.88 Å, which indicated that the main channels and micropores in CuBTC were collapsed at that temperature. A new peak was observed at 3.58 Å at 1100 K. It resulted from the collapse of the CuBTC framework, enabling the Cu dimers to move closer to each other.

The coordination number distribution was expected to show a step-wise behaviour with increase of the separation distance, r . As demonstrated by the insert plot in Figure 6.5(b), the integration of the RDF to a distance of 7.0 Å showed a coordination number of 1.0, 1.7 and 4.2 for 300 K, 700 K, and 1100 K, respectively. This difference in Cu coordination number implied increasing instability of the CuBTC framework at the higher temperature. The intercept at the right axis corresponded to the total number of copper atoms in the molecular formula of CuBTC framework used.



(a)



(b)

Figure 6.5. (a) Typical pairs of Cu dimer in the CuBTC framework. ‘Cu₂’ stands for the Cu dimer. Color codes are: yellow-Copper, grey-Carbon, red-Oxygen, and white-Hydrogen; (b) Cu-Cu , distribution function $g(r)$ and coordination number distribution $n(r)$ of CuBTC framework at 300 K, 700 K and 1100 K. The colored number at each peak represents the distance between the Cu dimers, the ones with the same color as in (a).

Contour plots of the Cu-Cu RDF at T= 300 K, 700 K, and 1100 K are provided in Figure 6.6. These demonstrate the evolution of the RDF with simulation time. At 300 K, the contour plot is made up of several separate bars. The number and position of the bars correspond to the peaks in Figure 6.5(b) (black solid line). The width results from the flexible nature of CuBTC and can be viewed as the fluctuating extension of the framework. The color scale shows the height difference of the RDF peaks. For example, a high peak of the Cu-Cu bond of the dimer is represented by the dark color at 2.65 Å in the contour map.

At 700 K, the RDF evolution was divided into two stages at about 100 ps. For the first part of the simulation, although it was not easy to distinguish peak distributions for the range 8 Å to 18 Å in r as we did for the 300 K case, we still observed blank regions of (3 Å, 7.5 Å) and (11 Å, 14.5 Å), indicating the existence of main channels and tetrahedral pockets, and the completeness of a CuBTC framework. After 100ps, the r range (3 Å, 7.5 Å) remained blank, but we observed the RDF peaks in the r range (11 Å, 14.5 Å). The change in RDF peak distribution indicated the disappearance of long-range correlations between Cu dimers and the partial collapse of the CuBTC framework at 700 K. It was obvious soon after the simulation began that the RDF peak showed a random distribution at 1100 K. This implies that CuBTC easily lost the main channels and tetrahedral pockets, and had a complete collapse of the framework at 1100 K. The distribution bar at 2.65 Å demonstrated the stability of the Cu dimer even at 1100 K.

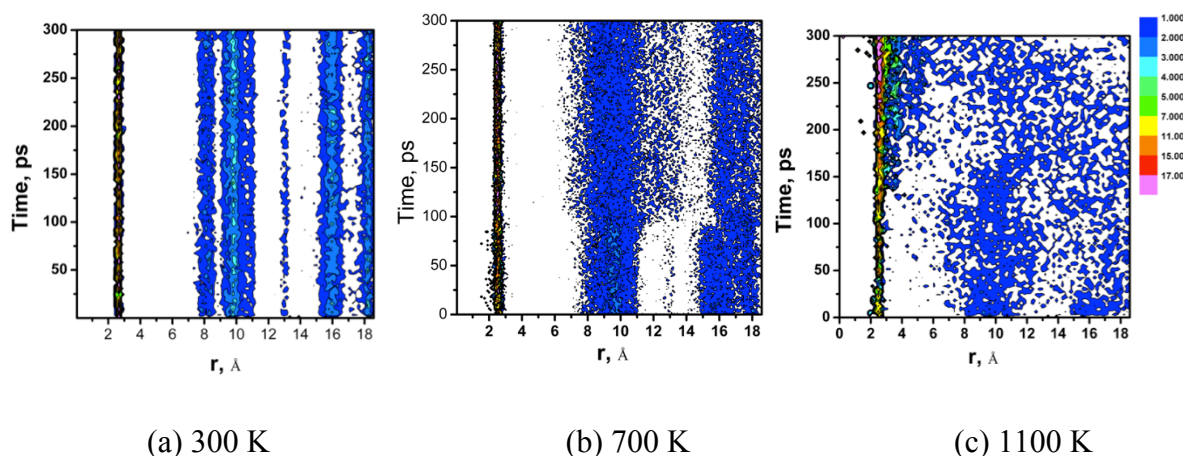


Figure 6.6. Contour plots of the evolution of the Cu-Cu RDF at (a) 300K; (b) 700K; (c) 1100K. The color scale represents the peak height of the Cu-Cu RDF.

6.4. Conclusions

Using the ReaxFF force field with the parameters developed recently for Cu/C/H/O, we studied the thermal stability of the dehydrated CuBTC framework from 300 K to 1100 K. The results show that CuBTC is thermally stable up to 565 K. When the temperature increases above 565 K, the framework starts to partially collapse. The RDF analysis shows that the long range correlations between Cu dimers disappear, indicating the loss of the main channels of CuBTC. When the temperature is above 800 K, we find decomposition of CuBTC. CO is the major production species and we also observe the release of CO₂, O₂, 1,3,5-benzenetricarboxylate (C₆H₃(CO₂)₃, BTC) and glassy carbon. The Cu dimer is stable up to 1100 K, but we find the formation of new copper oxide clusters at 1100 K. These results are consistent with experimental findings, validating the accuracy of the ReaxFF force field for the CuBTC framework and paving the path for future theoretical investigations of

the dynamical properties of CuBTC, and its application in adsorption, separation and catalytic process.

CHAPTER 7

Ammonia Adsorption on CuBTC: Molecular Simulation and Experimental Study

7.1. Introduction

Metal-organic frameworks (MOFs), an emerging class of materials introduced by Yaghi and co-workers,[48, 245] have played a significant role in the field of gas adsorption over the past decade.[159, 246, 247] The hybrid materials consist of inorganic (metals) and organic (carboxylate, sulfonate or phosphonate ligands) moieties[248, 249] bonded together. The strong scientific interest in these materials in adsorption processes results from their typically high porosity (up to 4500 m²/g for MOF-177)[250] along with their tunable chemistry (via selection of the inorganic and/or organic components).

Many studies reporting gas adsorption using MOFs address H₂ storage,[246] CO₂ capture[218] or CH₄ removal.[251] Nevertheless, as mentioned above, MOFs display features that could make them suitable for the removal/capture of other gases. For instance, only a few studies have been reported on the adsorption of ammonia (a toxic gas) using MOFs, despite the promising capacities of some of them.[24, 25, 36, 252] The MOFs exhibiting good ammonia uptake and reported so far include a copper-based MOF (CuBTC) and several zinc-based MOFs (MOF-74, MOF-177, IRMOF-3).[24, 25, 36, 252, 253]

In addition, from a general point of view, the identification of the mechanisms, thermodynamics and adsorption sites of gas adsorption on MOFs still remains a challenge. In

the case of ammonia adsorption on CuBTC, it has been shown that ammonia binds to the unsaturated MOF metallic sites (copper) via Lewis acid-base interactions, as indicated by a color change of the adsorbent.[24, 25, 36] An additional adsorption mechanism subsequent to the binding to copper has also been evidenced via a second color change of the material and via the apparent collapse of the MOF structure (inferred from thermal stability and porosity changes).[25, 36] Nevertheless, the details of what occurs in this second step are still not understood. Similarly, Saha and co-workers have observed the collapse of the MOF-177 structure upon exposure to ammonia, but the precise mechanism leading to this observation remains unclear,[252] although hydrogen bonding of ammonia with the metallic sites of MOF-177 has been hypothesized. As shown by Britt and co-workers, the presence of amino groups in IRMOF-3 organic ligand has a positive effect on ammonia adsorption.[24] Nevertheless, the reason for this is not discussed. Considering all of these factors, it is evident that a greater knowledge of reactive adsorption on MOFs is needed, as it would enable the design of new materials with enhanced performance and efficiency. Experimental[159, 246-249] and computational studies have been implemented to elucidate these questions but further work is still needed to achieve a complete understanding.

This chapter reports the study of ammonia adsorption on CuBTC. We first perform Density Functional Theory (DFT) calculations to study the interaction between NH_3 and CuBTC. Grand Canonical Monte Carlo (GCMC) simulations are then used to calculate the NH_3 adsorption isotherms on CuBTC at different temperatures. The results are discussed in conjunction with the experimental data measured at the dynamic and equilibrium conditions for NH_3 adsorption on CuBTC.

7.2. Molecular Modeling and Experimental Setup

7.2.1. DFT calculation of NH₃/CuBTC interactions

It has been reported that NH₃ has a strong binding on the Cu dimer of CuBTC.[254] DFT calculations have been carried out to determine the binding energy of NH₃ on both the organic linker and the metal Cu sites. The results were obtained by the Quantum-Espresso package (version 4.12) [155] with the PW91-GGA exchange-correlation functional. The plane-wave cutoff of 55 Ry and the density cutoff of 550 Ry have been tested to give a converged total energy and a good prediction of the geometrical parameters. The periodic rhombohedral box is made up of 156 atoms in the dehydrated form, as shown in Figure 7.1. Different sites have been investigated for NH₃ adsorption: A - along the Cu-Cu bond; B - close to the benzene ring; C - center of the main channel; D - center of the tetrahedral pore; E - perpendicular to the Cu-Cu bond (see Figure 7.1).

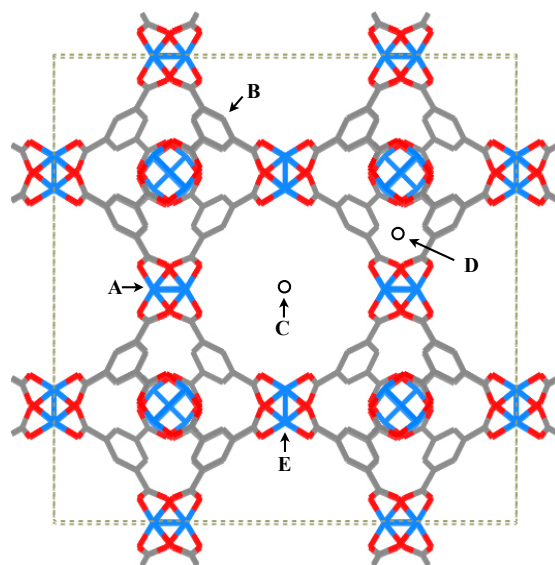


Figure 7.1. The supercell of CuBTC structure, where A, B, C, D, E correspond to different NH₃ adsorption sites: A - along the Cu-Cu bond; B - close to the benzene ring; C - center of the main channel; D - center of the tetrahedral pore; E - perpendicular to the Cu-Cu bond. The color codes are: blue – copper; red – oxygen; grey - carbon. Hydrogen atoms are not shown for clarity. The lattice is shown in dashed line.

The binding energy (E_b) is computed as the difference between the energy of the NH₃/CuBTC system ($E_{NH_3-CuBTC}$) and the sum of the relaxed pristine CuBTC (E_{CuBTC}) and the corresponding gas-phase species (E_{NH_3}) energies (see equation (7-1)). A larger binding energy indicates a stronger interaction between NH₃ and the adsorption site of CuBTC.

$$E_b = \{E_{NH_3} + E_{CuBTC}\} - E_{NH_3-CuBTC} \quad (7-1)$$

7.2.2 GCMC simulation of NH₃ adsorption on CuBTC

We performed GCMC simulations to directly address the adsorption behavior of ammonia on CuBTC and compare the calculated results with the experimental data. We calculate NH₃

adsorption on a $2 \times 2 \times 2$ supercell of CuBTC at three temperatures 301 K, 318 K and 348 K, and pressures up to 100 kPa. The CuBTC structure is treated as rigid in the simulation and the Lennard-Jones parameters are taken from the literature.^[255] A 5-site TraPPE model is used to describe NH₃ interactions.^[256] A cutoff of 12.8 Å is used for the Lennard-Jones interactions, while the long-range electrostatic interactions are treated by the Ewald summation method. The force field parameters and atomic charges are summarized in Table 7-1. The atomic notations for CuBTC in the GCMC calculation are displayed in Figure 7-2.

Table 7-1. The Lennard-Jones parameters: σ - the finite distance at which the interparticle potential equals zero, ϵ - the minimum potential, and atomic charges of atoms for CuBTC and NH₃ (q). M is a pseudo site of the 5-site NH₃ TraPPE model, where the negative charge is placed.

	CuBTC						NH ₃		
	C ₁	C ₂	C ₃	H	O	Cu	N	H	M
σ (Å)	3.75	3.55	3.55	2.42	2.96	3.11	3.42	0.00	0.00
ϵ/k_B (K)	44.91	35.23	35.23	15.10	73.98	2.52	185.00	0.00	0.00
q (e)	0.778	-0.092	-0.014	0.109	-0.665	1.098	0.00	0.41	-1.23

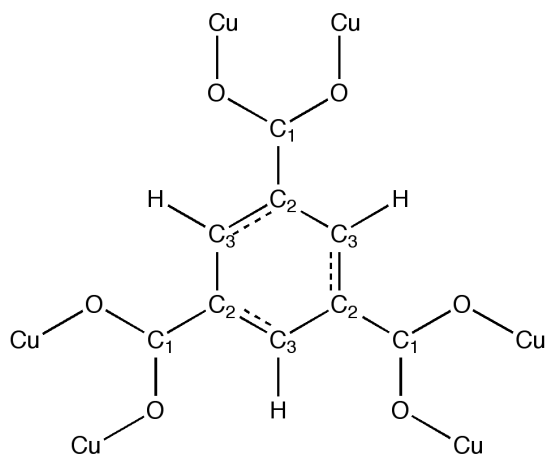


Figure 7.2. The atomic notations for CuBTC model in the GCMC calculation.

5×10^7 configurations were generated for each single-point adsorption calculation, among which the first 3×10^7 iterations are for equilibration and the later 2×10^7 are used to calculate the ensemble averages. The absolute adsorption data is converted into the excess values using equation (7-2):

$$N_{ex} = N_{abs} - V_g \rho \quad (7-2)$$

where V_g is the pore volume calculated using the method of Myers and Monson and ρ_g is the density of the ambient gas phase NH_3 .

7.2.3 Experimental measurements

The experimental studies were carried out by T.J. Bandosz and co-workers at The City College of New York. The procedure to synthesize the CuBTC material can be found in Ref. [257], using the method described by Millward and co-workers.[258]

(a) NH₃ breakthrough dynamic test

In order to determine the ammonia breakthrough capacity, dynamic breakthrough tests were performed at room temperature. In a typical test, a flow of ammonia diluted with dry air passes through a fixed bed of adsorbent with a total inlet flow rate of 225 mL/min and an ammonia concentration of 1000 ppm. The adsorbent bed contains about 2 cm³ of glass beads well mixed with the amount of adsorbent required to obtain a homogeneous bed, between 50 and 120 mg for CuBTC. The mixture was packed into a glass column. The beads are used to avoid the pressure drop and thus to favor the kinetics of the breakthrough tests. The electrochemical sensor from the Multi-Gas Monitor ITX system was used to measure the concentration of ammonia in the outlet gas. The adsorption capacity (mmol/g) of each adsorbent is calculated by integration of the area above the breakthrough curve.

(b) NH₃ adsorption: equilibrium measurements

The ammonia adsorption measurements at equilibrium were carried out using a ChemiSorb HTP (Micrometrics) with Karlrez® O-rings. This instrument has six independent furnaces, one for each sample port and is equipped with a two-stage vacuum system, diaphragm and high-vacuum turbomolecular pump. Prior to each measurement, the samples were outgassed in situ at 120 °C for 6 hours under vacuum. The quality of vacuum was checked by the leak test set at 2 mmHg/min. Ammonia used for the adsorption measurements was electronic grade (Air Products), minimum purity 99.999%. The tests were performed at the three temperatures 301 K, 318 K and 348 K.

(c) Determination of the isosteric heat of NH₃ adsorption

The isosteric heats of NH₃ adsorption, Q_{st} , were calculated from the Clausius-Clapeyron equation using the virial approach described in equation (7-3):[259]

$$\ln(p) = \ln(a) + \frac{1}{T} \sum_{i=0}^m c_{i,1} a^i + \sum_{i=0}^n c_{i,2} a^i \quad (7-3)$$

where a , p and T are the amount adsorbed, pressure, and temperature, respectively and $c_{i,1}$ and $c_{i,2}$ are empirical parameters. The variables m and n represent the order of the two polynomials, and a^i is a fitting parameter. Parameters $c_{i,1}$ and $c_{i,2}$ were obtained by fitting this equation to the adsorption data measured at two or more temperatures. The isosteric heat of adsorption as a function of a is given by Clausius-Clapeyron equation (7-4):

$$Q_{st}(a) = -R \left(\frac{\partial \ln(p)}{\partial (1/T)} \right)_a = -R \sum_{i=0}^m c_{i,1} a^i \quad (7-4)$$

where R is the universal gas constant.

7.3. Results and Discussion

7.3.1 NH₃ interaction with CuBTC

As shown in Table 7-2, NH₃ has the strongest binding with CuBTC structure when it interacts with the Cu-Cu dimer. The bond length between NH₃ and the Cu atom on site A (see Figure 7.1) is 2.04 Å. This demonstrates that NH₃ can chemisorb on CuBTC through copper dimers. The binding energies for two NH₃ molecules, one at each side of the copper dimer are 121.05 kJ/mol and 121.43 kJ/mol, respectively. It is thus estimated that under ideal conditions, the adsorption contribution from copper sites is 48 NH₃ per CuBTC unit cell.

Considering the molecular formula $\text{Cu}_{48}\text{C}_{288}\text{O}_{192}\text{H}_{96}$ for the dehydrated CuBTC super cell, we estimated that the amount of ammonia adsorbed on copper sites of CuBTC is 5.0 mmol/g. The trend in the isosteric heat as a function of the ammonia loading can be related to the strength of adsorption as well as the presence of difference adsorption sites in the adsorbent. The isosteric heat is changing from 60 to 44 kJ/mol, from a low loading to the high loading of NH_3 on CuBTC. The heats of adsorption are rather high, indicating a strong retention of NH_3 on CuBTC, especially when compared to the adsorption of other adsorbates such as CO_2 , CH_4 or H_2 on MOF materials. The reported heats of adsorption for these species are 4-45 kJ/mol for CO_2 , 2-30 kJ/mol for CH_4 , and 1-13 kJ/mol for H_2 , depending on the materials and the conditions of the calculations. From the heat of adsorption, we thus classify ammonia adsorption on CuBTC as a chemisorption process. These interactions are the strongest for CuBTC, and they represent the formation of $(\text{NH}_4)_3\text{BTC}$, which is expected to decompose during the outgassing and vacuum treatment, resulting in the reappearance of the sites for subsequent runs.

However, the binding energies calculated from DFT are higher than the experimental isosteric heats. This is because the experiments lack the measurements for the zero surface coverage of ammonia.

Table 7-2. The binding energy (kJ/mol) of NH_3 on different sites of CuBTC.

Sites	A	B	C	D	E
Binding energy (kJ/mol)	125.67	4.89	1.39	6.20	34.30

7.3.2. NH₃ adsorption on CuBTC

The knowledge of NH₃ binding energy on Cu sites provides qualitative information about the NH₃/CuBTC interactions and an estimate of the NH₃ adsorption contribution from the copper sites alone. However, the CuBTC structure comprises channels of about 9.0 Å in diameter surrounded by tetrahedral pockets of about 3.5 Å in diameter. Those micropores can also accommodate NH₃ molecules and thus an ammonia adsorption capacity higher than 5.0 mmol/g is possible. The adsorption capacity also depends on the temperature and pressure. For example, Karra and Walton reported the adsorption of 11.2 mmol (CO₂)/g (CuBTC) at 298 K and 300 kPa.[220] Yang and Zhong observed an adsorption of 10.3 mmol (CO₂)/g (CuBTC) at 298 K and 1 MPa, but 3.6 mmol (CH₄)/g (CuBTC) and 0.3 mmol (H₂)/g (CuBTC) under the same temperature and pressure.[255]

According to the experimental dynamic test, the breakthrough capacity of NH₃ adsorption on CuBTC is 6.8 mmol/g, while the BET surface area and the micropore volume for the CuBTC sample were measured to be 909 m²/g and 0.449 m³/g, respectively. The NH₃ uptake capacity on CuBTC is derived from the adsorption isotherms at 120 kPa. The measured values are found to be 12.1 mmol (NH₃)/g (CuBTC) at 301 K, 8.9 mmol (NH₃)/g (CuBTC) at 318 K, and 6.4 mmol (NH₃)/g (CuBTC) at 348 K. It is an interesting observation that a partial collapse of the porous structure is found after adsorption of NH₃ in a dynamic test under dry conditions. The measured surface area after adsorption in dynamic conditions is only from 5% to 18% of the original surface area, but the samples are still capable of retaining a significant quantity of NH₃ via physical adsorption, as evidenced by the adsorption isotherm data. Moreover, Peterson and co-workers have also reported about 40%

of the original amount adsorbed in the second adsorption run on CuBTC, with similar decreases in the surface area determined from nitrogen adsorption.[25]

The partial collapse of CuBTC is due to ammonia adsorption. As indicated from the DFT calculation, the highest energy centers on CuBTC are unsaturated copper sites, where complexation of NH_3 takes place. Preadsorption on those sites can cause a partial destruction of the porous network of CuBTC, with the release of carboxylic linkages being able to react with NH_3 to form $(\text{NH}_4)_3\text{BTC}$ as indicated by dynamic tests.[36] After outgassing and vacuum, the latter salts likely decompose, and the carboxylates then become available for reactions with NH_3 in the subsequent adsorption isotherm measurements. It must be noted that, due to the irreversible partial collapse of the CuBTC structure, re-adsorption of NH_3 on CuBTC is limited and the uptake is expected to be smaller than on the initial samples, as shown by Peterson and co-workers.[25]

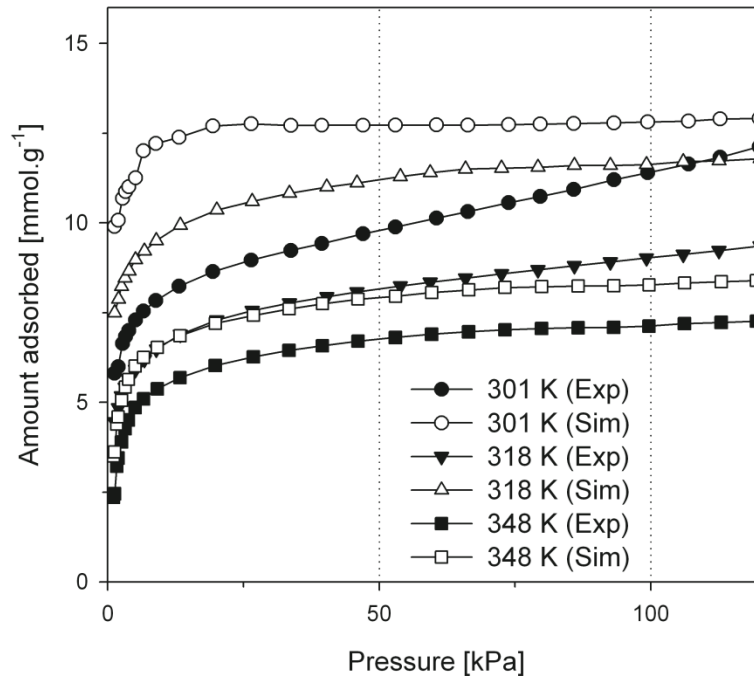


Figure 7.3. Adsorption isotherms for NH₃ adsorption on CuBTC: the comparison of GCMC results (open points) and experimental data (filled points). Temperatures are 301 K, 318 K and 348 K.

A comparison between experimental and GCMC simulated adsorption isotherms of NH₃ on CuBTC is shown on Figure 7.3 for temperatures 301K, 318K and 348K. It is clear that the calculated data generally support the shape of the experimental adsorption isotherms (except at 301 K), and also predicts the same trend that the amount of adsorbed NH₃ decreases when the temperature increases from 301K to 348K. Furthermore, the extent of this decrease in NH₃ adsorption capacity (for increasing temperature) is of the same order of magnitude between experimental and simulated data. However, it is not surprising that the net adsorption amount observed in the simulation deviates from the experimental results. The simulated data is larger than the corresponding experimental observations. The discrepancy

mainly comes from the use of a rigid model of CuBTC in the simulation. Even though some work has been conducted to account for the breathing effect and the structural changes occurring in MOF system upon adsorption,^[260-263] the present case is even more extreme since a partial collapse of CuBTC is observed during ammonia adsorption and this feature is not accessible in the GCMC calculation. Consequently, the GCMC prediction overestimates the amount of ammonia adsorbed since rigid pores that can accommodate ammonia molecules may collapse in the experiments. The predicted adsorption amount from GCMC calculations is also larger than the previous DFT estimation. This is because the DFT method can only correctly predict the chemisorption of NH₃ on copper sites, but we observed from GCMC calculation the physisorption of NH₃ in the micropores of CuBTC, as shown by a final adsorption configuration in Figure 7.4.

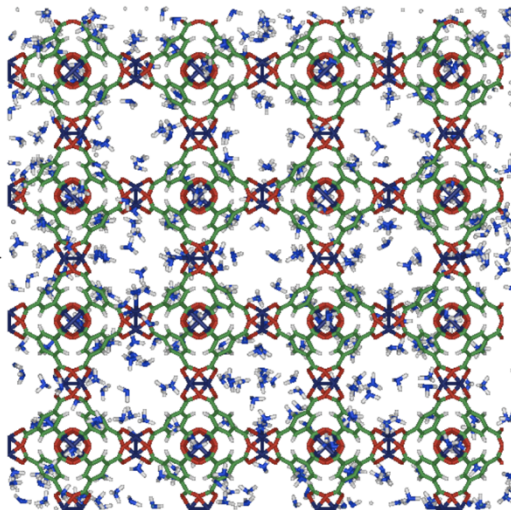


Figure 7.4. Final configuration of the CuBTC structure with adsorbed NH₃ molecules at copper sites and in the micropores (T = 348 K, P = 120 kPa). The color codes are: dark blue – copper; red – oxygen; grey – carbon; light blue – nitrogen; white - hydrogen.

The ammonia adsorption isotherms for CuBTC at 301 K and, to the lesser extent at 318 K, do not reach a limiting capacity. This indicates that at higher pressures even more ammonia could be adsorbed. This behavior can be linked to a significant volume of large pores (about 9 Å in diameter) present in the MOF materials. These pores were found suitable for CO₂ storage at high pressures. Interestingly, at 348 K, type I isotherms with a characteristic plateau are measured. That change in the shape can be related to the reactive adsorption of ammonia on CuBTC, which is enhanced at higher temperatures. As indicated previously, ammonia adsorbs on CuBTC via complexation on unsaturated copper that is followed by a gradual destruction of the porous network with the release of carboxylic linkages and their further reactions with ammonia leading to the formation of (NH₄)₃BTC. At higher temperatures the reactions leading to the destruction of the pore network should be more pronounced and the collapse of the structure with the progress of adsorption observed before causes the limitations in the availability of the adsorption centers. This is visible in the change in the shape of the ammonia adsorption isotherm. The reactive adsorption and the instability of the MOF cause the measured isotherms to represent the apparent complex interactions mechanisms.

7.4. Conclusions

The results of this study support the mechanism of ammonia adsorption on CuBTC, and can be considered as the first effort to understand the reactive adsorption of NH₃ on CuBTC. In general, CuBTC exhibits higher ammonia adsorption capacities than for other gas-phase molecules reported in the literature, such as CO₂, CH₄ and H₂. The heats of adsorption from

experiments are compared with the DFT calculation results. The isosteric heats of ammonia adsorption on CuBTC indicate strong adsorption of ammonia. This is linked to chemical adsorbate-adsorbent interactions. The molecular simulations conducted on CuBTC support the trends found experimentally. In particular, the strong chemisorption of ammonia on the metallic centers of CuBTC is confirmed. Nevertheless, higher adsorption capacities are predicted compared to the measured ones. This discrepancy is believed to arise from the partial collapse of the CuBTC structure upon exposure to ammonia, which is not accounted for in the GCMC simulations with rigid models and classical force fields.

In order to address this drawback of the rigid CuBTC model used here, we propose the use of a ReaxFF force field that accounts for the flexibility of the MOF, as well as the chemisorption and physisorption of NH_3 . This work is described in Chapter 8.

CHAPTER 8

Reactive Adsorption of Ammonia on CuBTC: a ReaxFF Molecular Dynamics Simulation

8.1. Introduction

Metal-organic frameworks (MOFs) are 3-D network hybrid materials consisting of inorganic (metal) and organic (carboxylate, sulfonate or phosphonate ligands) moieties.[264, 265] They exhibit a high porosity, a large surface area, and a tunable chemistry through the selection of inorganic and/or organic components.[244, 266] Those characteristics make MOFs good candidates in the fields of gas adsorption and separations. Recent studies further show that MOFs demonstrate potential as catalysts through the metal sites,[267-269] and they have been applied to sense,[270] capture or decompose molecules such as H₂O, CO₂, H₂S and NH₃. [24, 210] The previous experiments have shown that a copper based MOF (CuBTC, also known as HKUST-1) and several zinc-based MOFs (MOF-74, MOF-177, IRMOF-3) exhibit good ammonia uptake and demonstrate the decomposition of NH₃ and H₂S gases on the metal sites.[36, 205, 228]

However, it is still a challenge to theoretically identify the thermodynamics and the mechanism of reactive adsorption on MOFs. The challenge comes mainly from the lack of a force field that can accurately describe both the flexible nature of the MOF framework and the reactive interactions between adsorbates and the MOF. For example, many theoretical calculations, specifically grand canonical Monte Carlo (GCMC) simulations, have been

focused on the prediction of physical adsorption and separation of gas mixtures in rigid MOF models.[221, 271-274] But many MOFs exhibit adsorbate-induced structural flexibility in experiments,[224, 227] and the unit cell dimensions of some MOFs are reported to vary by as much as 10% when molecules are adsorbed within the pores.[244] In addition, most calculations apply non-reactive force fields where the chemistry of the system is pre-defined and no bond breaking or formation is allowed during the simulation. Such models cannot describe situations where a MOF framework is found to undergo a structural collapse or to react with the adsorbate.[205, 228] Also, some MOFs undergo adsorption-induced phase translation to new crystal structures.[224] In the case of ammonia adsorption on CuBTC, it has been shown that ammonia binds to the unsaturated copper sites via Lewis acid-base interactions, as indicated by a color change of the adsorbent.[52] We also see evidence of strong chemisorption of ammonia on copper sites in the isosteric heat measurements.[36] Although our molecular simulations of NH₃/CuBTC systems support the adsorption trend observed from the experiments, the predicted adsorption capacities are too high compared with the experimental results.[228] The discrepancy is attributed to the partial collapse of the CuBTC framework upon exposure to ammonia, which was not accounted for in the previous GCMC simulations.

The present chapter reports a ReaxFF molecular dynamics (RMD) simulation of ammonia adsorption on CuBTC. It is known that CuBTC has two exchangeable coordination sites, which are occupied by water molecules in the as-synthesized form. The coordinated water can be easily removed, for example by heating to 373K in air, and makes the unsaturated copper sites available for adsorption.[52] We use the dehydrated framework here

and divide the study into the following three cases: (1) the hydrostatic stability of dehydrated CuBTC under different temperatures and water concentrations; (2) the adsorption of NH_3 on dehydrated CuBTC at 301, 318 and 348 K, where experimental adsorption data are available for comparison; (3) the adsorption of $\text{NH}_3/\text{H}_2\text{O}$ mixtures on dehydrated CuBTC at 301 K. The chapter is organized as follows: Section 8.2 introduces the computational methods, including the ReaxFF force field, the atomic model of the dehydrated CuBTC system, and the reactive molecular dynamics method. In section 8.3, we present the results for the hydrostatic stability of dehydrated CuBTC. The reactive adsorption results of NH_3 and $\text{NH}_3/\text{H}_2\text{O}$ mixtures on dehydrated CuBTC are described in Section 8.4 and Section 8.5, respectively. The conclusions are finally summarized in Section 8.6.

8.2. Computational Methods

8.2.1 ReaxFF force field

Although *ab initio* quantum mechanical (QM) methods are capable of predicting the energy barrier, reaction mechanism and reaction rate, QM calculations are known to be computationally intensive and thus are limited to relatively small systems and short time scales, generally hundreds of atoms for tens of picoseconds. Developed by fitting the QM results, ReaxFF is a bond-order dependent force field that provides an accurate description of reaction chemistry of bond breaking and bond forming, and allows MD simulations for thousands of atoms for a time scale of microseconds.[\[102\]](#) It has been successfully used to describe the structures, energy surfaces, and reaction barriers of materials, including hydrocarbons,[\[51, 235\]](#) nitramines,[\[236, 237\]](#) metals,[\[238-240\]](#) and metal oxides.[\[241, 243\]](#)

The key difference between ReaxFF and other force fields is that ReaxFF does not need the connectivity input for the chemical bonds, but calculates the bond order and covalent interaction directly from instantaneous interatomic distances which are updated at every step of the dynamics. The electrostatic and van der Waals interactions are also calculated at every step during the dynamics for all the atom pairs. The set of ReaxFF parameters used in this work was determined using a combination of previously developed force fields. Parameters were retrained to enable the description of CuBTC structure and its interaction with NH₃ and H₂O.[235, 243] For example, we combined the Cu/O/H parameters of van Duin *et al.*[243] with the glycine ReaxFF parameters published recently.[235] These force fields share O/H parameters and use exactly the same potential functions, making integration of these parameter sets relatively straightforward. We do not further optimize bond parameters of C/Cu pairs, since such bonds are not expected to form in the oxygen-rich environment of the simulations. The non-bonded C/Cu interactions were obtained from standard combination rules.

8.2.2 Atomic models for dehydrated CuBTC

The trial of building up the atomic model for the dehydrated CuBTC system involved first the GCMC simulation of NH₃ adsorption on the rigid CuBTC framework. Full details of the procedure are described in our previous work.[228] We calculated NH₃ adsorption on a 2 × 2 × 2 super cell of dehydrated CuBTC framework at 301 K, 318 K and 348 K. The framework and NH₃ (a 5-site TraPPE model[256]) were treated as rigid, and we used Lennard-Jones parameters to describe the adsorbate-adsorbent interactions. As shown in Figure 8.1(a), the

adsorbed amount observed in the simulation is greater than that found experimentally. We attributed the discrepancy to the use of rigid models of CuBTC and NH₃ in the simulation. Also, the partial collapse of CuBTC observed during ammonia adsorption experiments cannot be accounted for in such GCMC calculations. As a second step we thus took the coordinates of the hydrated CuBTC framework from the x-ray powder diffraction (XRPD) result of Williams *et al*[213] and manually removed the coordinated water molecules to obtain the dehydrated CuBTC geometry. Taking the NH₃/CuBTC configuration as an example, the number of NH₃ molecules corresponding to our experimental adsorption result, were randomly inserted into the main channels and tetrahedral pockets of the CuBTC framework. A separation distance of 3.0 Å was used to avoid overlaps when inserting NH₃ molecules. Other initial configurations for RMD calculations in this work were also prepared in this way. A snapshot of the CuBTC framework with 63 NH₃ molecules at 348 K is provided in Figure 8.1(b).

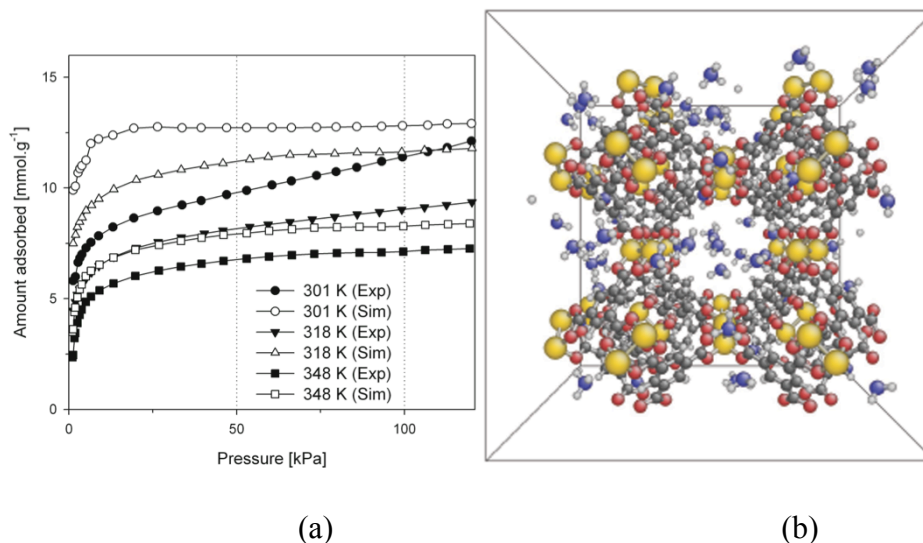


Figure 8.1. (a) A comparison of simulated and experimental adsorption isotherms of NH₃ on dehydrated CuBTC framework at 301, 318, and 348 K; [228] (b) A snapshot of the CuBTC framework with 63 NH₃ molecules at 348 K; periodic boundary conditions are applied in the x, y and z directions. Color codes are: yellow-Copper, grey-Carbon, red-Oxygen, white-Hydrogen, and blue-Nitrogen.

8.2.3. RMD simulation characteristics

The periodic cubic simulation box was made up of a $1 \times 1 \times 1$ unit cell of the dehydrated CuBTC framework (molecular formula: $\text{Cu}_{48}\text{C}_{288}\text{O}_{192}\text{H}_{96}$) with the desired number of NH₃ and or H₂O molecules. The calculations were performed in an isothermal-isobaric (NPT) ensemble with Verlet integrator and a time step of 0.25 fs. The pressure and temperature were controlled by the Bersendsen barostatting and thermostatting methods, with damping constants of 2500 fs and 100 fs, respectively. Velocities were initiated using a Boltzmann distribution. The trajectory was collected every 50 fs to analyze the results of each RMD calculation.

We studied the hydrostatic stability of CuBTC framework under the following conditions: temperatures – 301, 323, 345, 367, 389 K; water concentrations (the number of water molecules) – 12, 24, 48, 96, 144, 196. The defined number of water molecules corresponds to 0.25, 0.5, 1.0, 2.0 3.0 and 4.0 mole equivalents with respect to copper sites of the CuBTC framework. The choice of water content corresponds to that in a recent publication of Gul-E-Noor *et al.*, where they studied water adsorption on CuBTC by ^1H and ^{13}C solid-state NMR spectroscopy.[226] Our aim was to determine the hydrostatic stability of dehydrated CuBTC at temperatures where most adsorption and separation experiments are conducted.

In accordance with our previous experiments,[228] NH_3 adsorption was studied at three temperatures: 301 K, 318 K and 348 K, where the simulation box had 120, 88, and 63 NH_3 molecules, respectively. Last, three $\text{NH}_3/\text{H}_2\text{O}$ mixtures (24 H_2O / 120 NH_3 , 48 H_2O / 120 NH_3 , 96 H_2O / 120 NH_3) were chosen to study how water molecules affect NH_3 adsorption on CuBTC at room temperature, 301 K.

8.3. Results and Discussion

8.3.1. Hydrostatic stability of dehydrated CuBTC framework

As one of the few MOFs that are produced by the chemical industry, the hydrostatic stability of CuBTC has been studied in many experiments. Schlesinger *et al.* reported that dehydrated CuBTC is thermally stable until 473 K, whereas the hydrated form $(\text{Cu}_3(\text{BTC})_2(\text{H}_2\text{O})_3)$ decomposes when the temperature is above 343 K, implying that CuBTC is not stable in the presence of water molecules.[275] Other publications, however, conclude that water

adsorption in CuBTC is reversible and the adsorbed H₂O can be thoroughly removed without destroying the CuBTC framework under moderate temperatures.[214, 276] Simulation results of H₂O adsorption isotherms have been reported on CuBTC at room temperatures.[277] However the use of a rigid CuBTC model and a non-reactive force field has prevented previous simulations from predicting CuBTC hydrostatic stability in real applications.

In our calculations, the hydrostatic stability of CuBTC under different water concentrations and different temperatures is monitored by the evolution of the copper – copper radial distribution function (RDF). The RDF, also known as the pair correlation function, is a useful tool to extract structural information from molecular simulation trajectories by providing the probability density of one atom having a neighbor at a given distance. Typical Cu-Cu distances of CuBTC are provided in Figure 8.2 (a), where the framework comprises channels of about 9.0 Å in diameter surrounded by tetrahedral pockets of about 3.5 Å in diameter. In Figure 8.2 (b) to (e) the RDF evolution of Cu-Cu distance for a pristine CuBTC framework are shown at 301 K, 12 H₂O in CuBTC at 301 K, 12 H₂O in CuBTC at 389 K, and 192 H₂O in CuBTC at 389 K, respectively. We can conclude from the RDF information that CuBTC retains both its local and global structures at the designed combinations of water concentration and temperature. These calculations provide theoretical support to experimental findings that dehydrated CuBTC framework is hydrostatically stable for moderate temperature applications (up to 116 °C).[213]

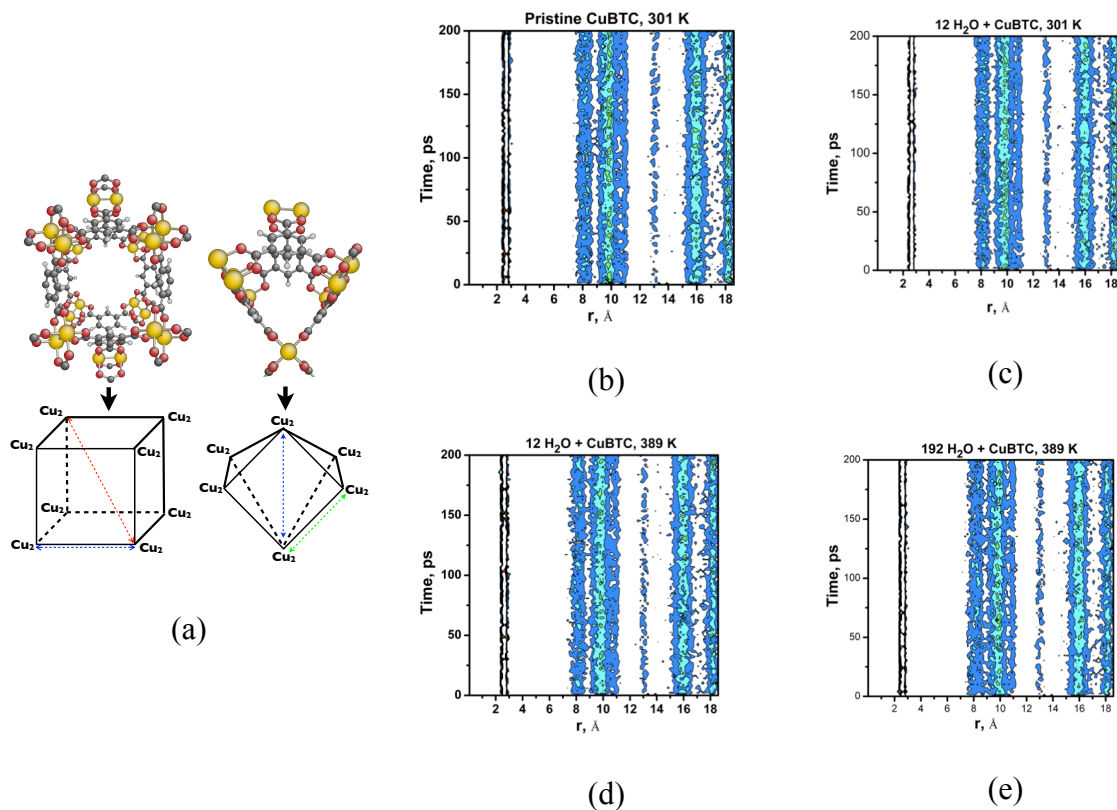


Figure 8.2. (a) A sketch of typical Cu-Cu distances of a CuBTC framework. Right hand figures (b) to (e) show the evolution of Cu-Cu radial distribution function for: (b) a pristine dehydrated CuBTC at 301 K; (c) 12 H₂O in a dehydrated CuBTC at 301 K; (d) 12 H₂O in a dehydrated CuBTC at 389 K; (e) 192 H₂O in a dehydrated CuBTC at 389 K.

8.3.2. Reactive adsorption of NH₃ on dehydrated CuBTC framework

Ammonia molecules are found to decompose on CuBTC in all three cases studied: 301, 318 and 348 K, where the simulation box has a periodic dehydrated CuBTC framework and 120, 88, and 63 NH₃ molecules, respectively. The difference in temperature or NH₃ concentration changes the number of chemisorbed and decomposed NH₃ molecules, but does not change the reaction mechanism. We thus only present the results of the reactive adsorption of NH₃ at 348 K.

A comparison of the Cu-Cu RDF for a pristine dehydrated CuBTC with the one with 63 NH₃ molecules is shown in Figure 8.3. It is clear that the Cu-Cu pair correlation is lost at large distances upon interacting with NH₃ molecules. Although most peaks appear at r ranges of 8 - 11 Å and 16 - 18 Å after interaction with NH₃, they are not distinguishable as in the pristine dehydrated CuBTC. This indicates the partial decomposition of the CuBTC framework due to NH₃ adsorption. The Cu dimers, demonstrated by the two peaks at $r = 2.5$ Å and 2.9 Å, are stable over the 300 ps RMD. This decomposition of the framework provides an explanation for the discrepancy in the NH₃ adsorption isotherms in Figure 8.1 (a). The GCMC results from the rigid CuBTC model overestimate the amount of ammonia adsorbed since the channels and micropores that can accommodate ammonia molecules will change during the NH₃ adsorption. A pore volume decrease of 5 % to 18 % (breathing effect excluded) has been estimated in our experiments, resulting from the partial collapse of the CuBTC framework upon NH₃ adsorption.[\[228\]](#)

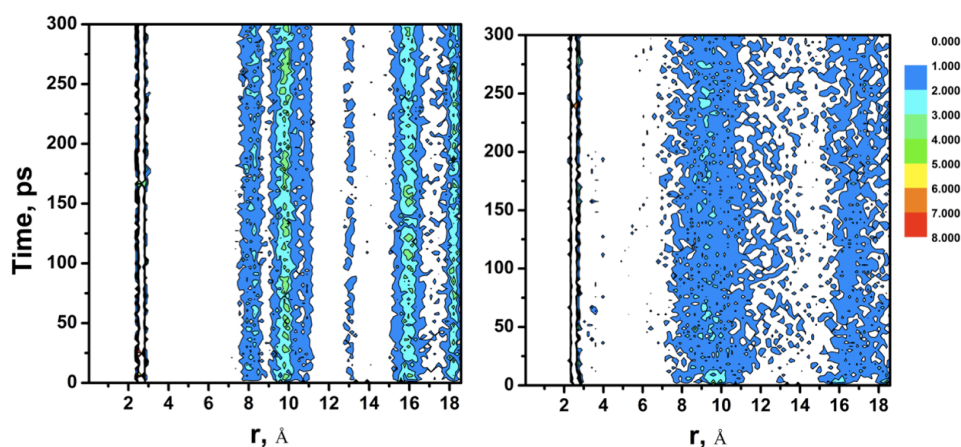


Figure 8.3. Cu-Cu radial distribution function evolution at 348 K: (a) pristine dehydrated CuBTC framework; (b) dehydrated CuBTC framework with 63 NH₃ molecules.

On the other hand, we want to know whether the CuBTC framework will collapse completely if there are adequate NH_3 molecules. Our previous DFT calculation has shown that NH_3 can chemisorb on the CuBTC framework through copper dimers, forming a bond of length 2.04 Å with a Cu atom of CuBTC.[228] The binding energies for two NH_3 molecules, one at each side of the copper dimer, are 121.05 kJ/mol and 121.43 kJ/mol, respectively, indicating that each Cu dimer can host two chemisorbed NH_3 molecules, one at each copper site. Considering the molecular formula of $\text{Cu}_{48}\text{C}_{288}\text{O}_{192}\text{H}_{96}$ for the dehydrated CuBTC framework used, we expect a chemisorption of 48 NH_3 molecules in our calculations.

The RDFs of the nitrogen atom with respect to the oxygen and copper sites of CuBTC are plotted in Figure 8.4. The color map scale has been changed to demonstrate the first RDF peaks only. The first peak for the O-N RDF is at ~ 2.7 Å for the whole 300 ps RMD simulation, indicating that the distance between the NH_3 molecules and the oxygen sites of CuBTC does not change over the course of the simulation. On the other hand, the Cu-N RDF shows that the distance between the nitrogen of NH_3 and the copper sites is about 2.0 Å, and the value is stable after 50 ps of the calculation. The calculated distance between NH_3 and copper sites is in good agreement with the DFT result. The distance also indicates that NH_3 molecules preferentially adsorb to the copper sites but not to the oxygen atoms of CuBTC.

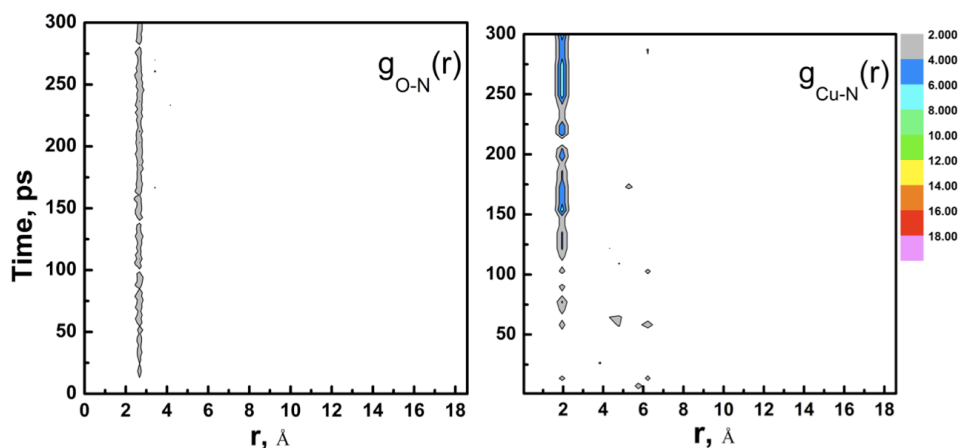


Figure 8.4. Evolution of radial distribution function for the 63-NH₃/CuBTC system at 348 K: (a) O-N; (b) Cu-N.

The distribution of the 63 NH₃ molecules were analyzed during the 300 ps RMD simulation, as shown in Figure 8.5. The curves are fitted with five term polynomial functions to better demonstrate the trend and the limit. The number of initial gas-phase NH₃ molecules is decreasing upon interaction with the CuBTC framework. NH₃ molecules are quickly chemisorbed to CuBTC during the first 50 ps of the simulation and the number remains around 50 - 53 for the remaining 250 ps of the simulation. The gas-phase NH₃ molecules, which are physisorbed in the channels or micropores, are less than 10 % of the initial number. This demonstrates that the dehydrated CuBTC framework hosts NH₃ molecules mainly through chemisorption. The smaller amount of physisorbed NH₃ can be explained by the collapse of the CuBTC framework upon NH₃ chemisorption, where the numbers of main channels and micropores are reduced significantly. The amount of chemisorbed NH₃ is more than we expect from DFT calculations. This is probably due to the collapse of the CuBTC framework, making the Cu dimer and carboxylic moiety available to interact with more NH₃

molecules. For example, three H₂O molecules are reported to be coordinated to Cu in the CuBTC framework in the experiments of Schlesinger and co-workers.[275]

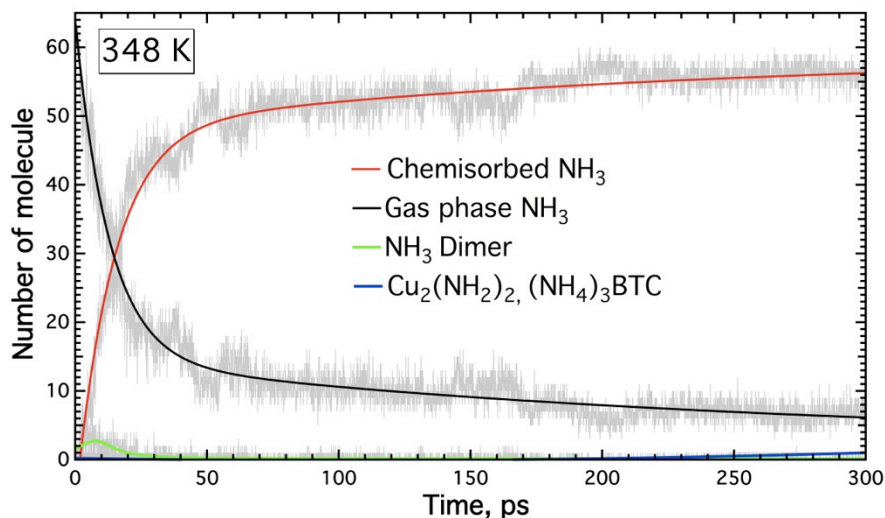


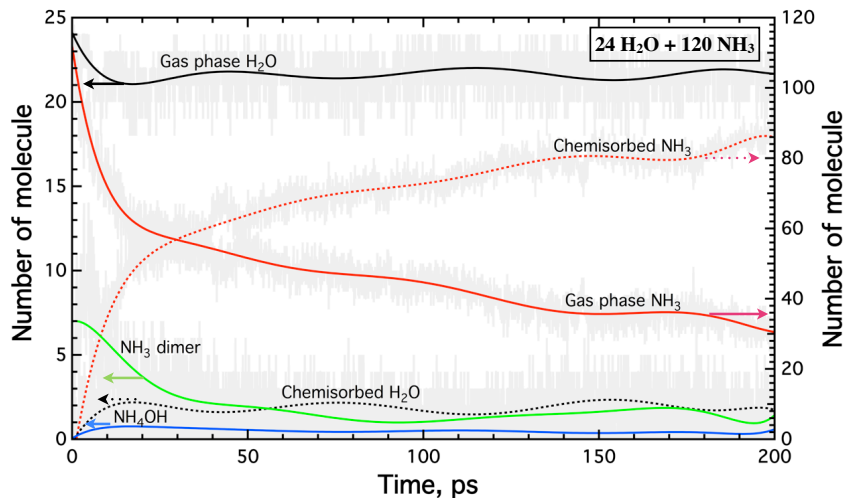
Figure 8.5. Reactive adsorption of NH₃ on dehydrated CuBTC at 348 K. The distribution of molecules is monitored as a function of simulation time.

We also observed the formation of NH₃ dimers at the beginning of the RMD calculations. The number decreases quickly, indicating that the NH₃ prefers to chemisorb to the copper sites rather than forming a dimer with another NH₃ molecule. In the later part of our calculation, we detect that the Cu dimer can decompose and forms a new product with NH₃. NH₃ molecules also saturate the breaking bonds of copper and BTC by forming a new structure of (NH₄)₃BTC. The formation of equimolar Cu₂(NH₂)₂ and (NH₄)₃BTC structures is only observed at 348 K. There is no such product at the lower temperatures of 301 K or 318 K. The results agree with previous experiments by T.J. Bandosz and co-workers, where the N-H vibration frequency of NH₄⁺ is observed for NH₃ adsorption on CuBTC/Graphene

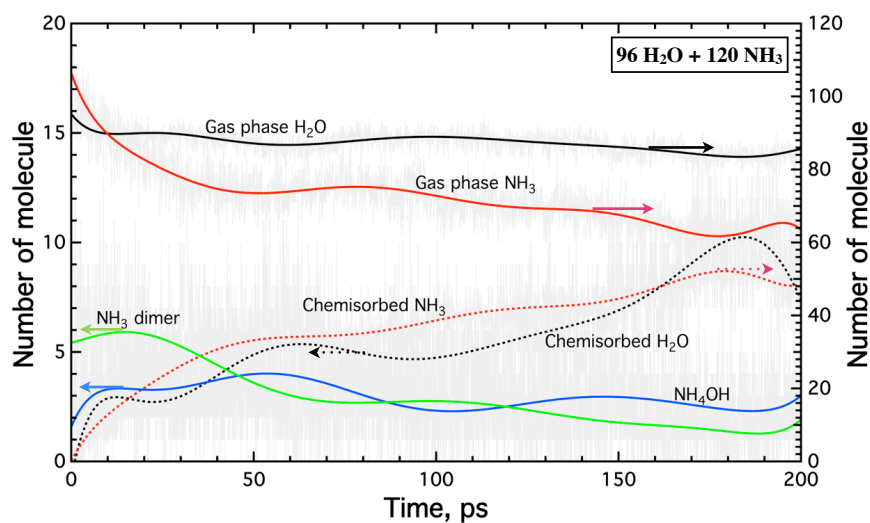
nanocomposite.[36, 228] The formation of $(\text{NH}_4)_3\text{BTC}$ is also observed in the experiments of Peterson *et al.*[229] Their ^1H MAS NMR results also reveal the existence of $\text{Cu}(\text{OH})_2$ under humid conditions, which is not confirmed in our calculation of a dehydrated CuBTC framework.

8.3.3. Reactive adsorption of $\text{H}_2\text{O}/\text{NH}_3$ mixtures on dehydrated CuBTC framework

The molecular distribution for two $\text{H}_2\text{O}/\text{NH}_3$ mixtures on dehydrated CuBTC framework at 301 K is shown in Figure 8.6. The mixture of 48 $\text{H}_2\text{O}/120$ NH_3 shows similar trends and thus is not shown. The distribution of H_2O and NH_3 molecules are recorded over the 200 ps simulation and the data are fitted in the same way as in Figure 8.5, to show the trend and limit of the curves.



(a) 24 H₂O/120 NH₃, 301 K



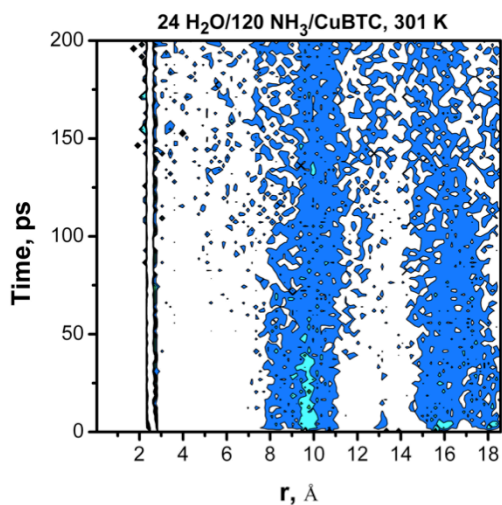
(b) 96 H₂O/120 NH₃, 301 K

Figure 8.6. Reactive adsorption of H₂O/NH₃ mixtures on dehydrated CuBTC at 301 K. The distribution of molecules is monitored as a function of simulation time: (a) 24 H₂O/120 NH₃; (b) 96 H₂O/120 NH₃. Arrows are added to guide the reading of numbers in accordance with the axis.

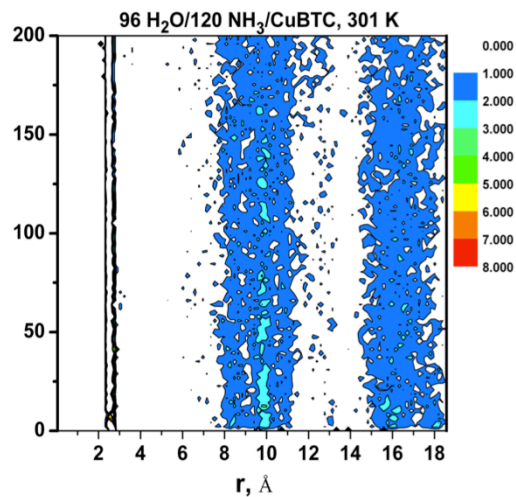
The number of gas-phase H₂O molecules is changing from 24 to 21, and 96 to 86 for the two mixtures, indicating that most H₂O molecules do not interact with the CuBTC

framework but remain as free molecules in the channels and micropores. On the contrary, the number of chemisorbed NH_3 molecules is substantially reduced by the increase of H_2O molecules, from 86 to 48, when the number of H_2O increases from 24 to 96. The results imply that the dehydrated CuBTC framework has higher chemisorption selectivity for NH_3 molecules. Although H_2O molecules do not demonstrate a strong chemisorption on the CuBTC framework, they can block NH_3 from interacting with the framework and greatly reduce the amount of chemisorbed NH_3 on CuBTC. It has to be stressed that only chemisorbed ammonia is discussed here. The positive effect of water on overall adsorption of ammonia on CuBTC was discussed elsewhere. The enhanced adsorption of ammonia was linked to the dissolution of NH_3 in the water film present in the CuBTC pores after the pre-humidification process. Such water coverage is not reached in our calculations.

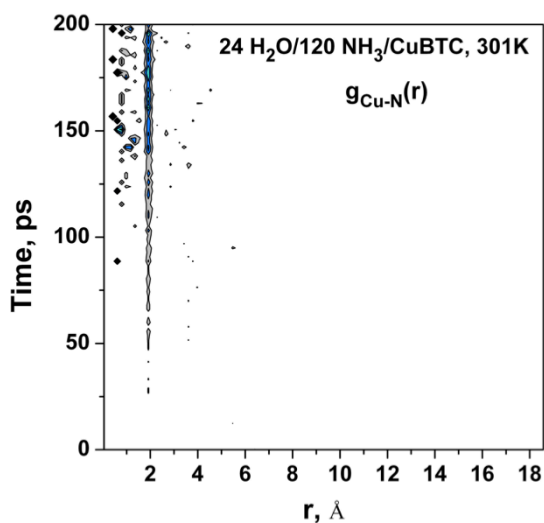
These results are also supported by the RDF analysis in Figure 8.7. The peaks of the Cu-Cu RDF are distributed more randomly for the low H_2O content mixture. This is because under low water content, more NH_3 molecules are chemisorbed to the CuBTC and the framework is collapsed in the long run. The Cu-N RDFs further support this conclusion. At low water content (Figure 8.7c), NH_3 can react with the CuBTC framework and some bonds of Cu-N are found to be less than 2.0 \AA in the later part of the simulation. With the same color scale map, the Cu-N RDF with high water content does not have any peak distributed in the range of $0 \sim 2.0 \text{ \AA}$. Due to fewer chemisorbed NH_3 molecules on CuBTC, the probability of finding Cu-N RDF peaks at $r = 2.0 \text{ \AA}$ is also greatly reduced, demonstrated by a lighter color in Figure 8.7d.



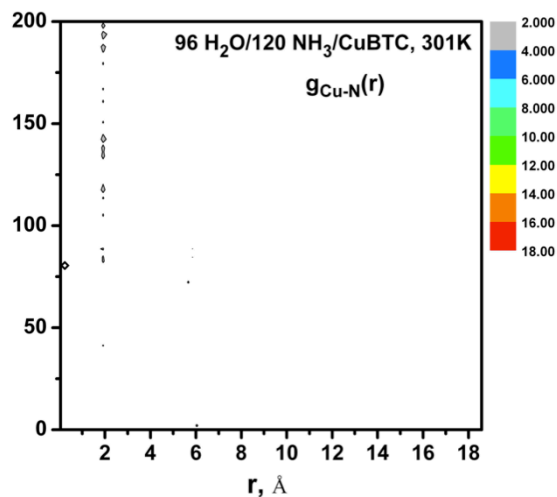
(a) Cu-Cu, 24 H₂O



(b) Cu-Cu, 96 H₂O



(c) Cu-N, 24 H₂O



(d) Cu-N, 96 H₂O

Figure 8.7. Evolution of radial distribution functions: (a) Cu-Cu RDF for the 24 H₂O/120 NH₃/CuBTC system; (b) Cu-Cu RDF for the 96 H₂O/120 NH₃/CuBTC system; (c) Cu-N RDF for the 24 H₂O/120 NH₃/CuBTC system; (d) Cu-N RDF for the 96 H₂O/120 NH₃/CuBTC system.

8.4. Conclusions

With the ReaxFF force field parameterized for the Cu/O/H/N system, we have studied the reactive adsorption of NH_3 on dehydrated CuBTC metal-organic framework. We find that the dehydrated CuBTC is hydrostatically stable under water contents up to 4.0 mole equivalents with respect to copper sites and temperatures up to 116 °C. When NH_3 molecules are added to the channel and micropores of CuBTC, they prefer to chemisorb to the copper sites rather than forming a dimer with another NH_3 molecule. The formation of equimolar $\text{Cu}_2(\text{NH}_2)_2$ and $(\text{NH}_4)_3\text{BTC}$ structures is also observed at 348 K, which is in good agreement with previous experimental findings. The CuBTC framework partially collapses upon NH_3 adsorption, but the Cu-Cu dimer structure is stable under the investigated conditions. The adsorption behavior of $\text{H}_2\text{O}/\text{NH}_3$ mixture on dehydrated CuBTC is also investigated in this work. Water molecules do not demonstrate a strong interaction with the copper sites of CuBTC, but the existence of water can substantially reduce the amount of chemisorbed NH_3 molecules. To the best of our knowledge, this is the first theoretical study of the reactive adsorption of NH_3 on CuBTC framework. The results explain the experimental findings and provide atomic level insight into the removal of ammonia by reactive adsorption on CuBTC frameworks.

CHAPTER 9

Conclusions and Outlook

9.1. Conclusions

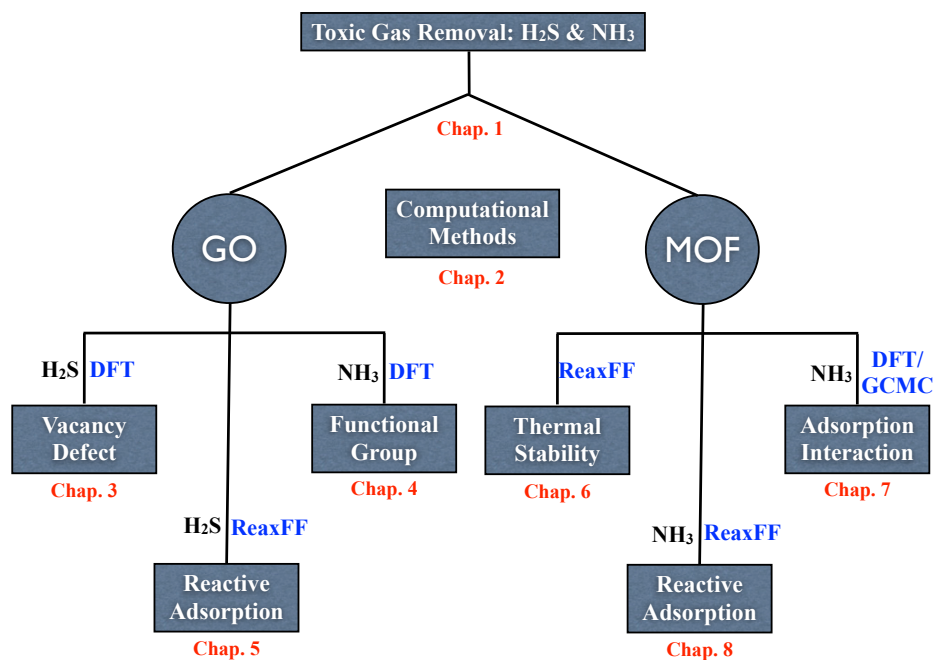


Figure 9.1. The tree of thesis outline with the color codes: black - the toxic gas investigated; blue - the computational method; red - the chapter number; white - the keyword for the topic.

As shown in Figure 9.1, in this thesis, we have been applying different computational methods to study the reactive adsorption of NH_3 and H_2S on graphene oxide (GO) and CuBTC metal-organic framework (MOF). The results can be summarized as follows:

- The adsorption and dissociation of H_2S on a single vacancy on the graphene surface were investigated by the DFT method. The stable adsorption structures and adsorption

energies of H₂S have been identified, and H₂S adsorption was found to be energetically favorable on the center of the single vacancy, with hydrogen atoms up and the sulfur atom lying closest to the surface. Stable intermediate states for H₂S dissociation were also determined from the calculation. The results indicate that H₂S dissociates in a similar way to H₂O on the single vacancy. Both the adsorption and dissociation of H₂S are exothermic, and the calculated lowest activation energy barrier for dissociation is around 40.44 kcal/mol, indicating the dissociation of H₂S over graphene single vacancy is a favorable process.

b. The efforts to understand the catalytic role of GO materials also included DFT calculations to study the interactions between NH₃ and the functional groups (carboxyl, hydroxyl, epoxy) of GO. The results show that NH₃ can dissociate on the carboxyl and epoxy groups. Furthermore, the dissociation of NH₃ on the carboxyl group is an endothermic process, but an exothermic reaction with the epoxy group and the activation energy is small. Another important result is that H₂O does not dissociate but forms a hydrogen bond with the functional groups. This explains the experimental results and shows that H₂O molecules can screen the accessibility of carboxyl and epoxy groups for the reactions with NH₃.

c. The temperature-programmed MD calculations, together with the ReaxFF method, were applied to generate realistic GO models for theoretical calculations. By using hydroxyl and epoxy functional groups and controlling the functionalization density, we were able to generate different functional patterns on the graphene surface, including the carboxyl group, the aldehyde group, the single vacancy with a pair of carbonyls, the pair of meta-epoxy groups, the pair of carbonyls, the large carbon ring, the preferential alignment of epoxy groups along the zigzag direction and so on. We further studied the adsorption and

dissociation of H₂S and H₂O/H₂S mixtures on those realistic GO structures. H₂S is observed to dissociate on the GO structures, but H₂O molecules can more easily adsorb to the active sites of GO, and thus block the H₂S molecules from interacting with GO.

d. MOFs are widely used as adsorbents in adsorption and separation applications. However, the thermal and hydrostatic stabilities are always a limit to their applications. By using the ReaxFF method, we studied the thermal stability of the dehydrated CuBTC framework from 300 K to 1100 K. The results show that CuBTC is thermally stable up to 565 K. When the temperature increases above 565 K, the framework starts to partially collapse. The RDF analysis showed that the long-range correlations between the Cu dimers disappear, indicating the loss of the main channels of CuBTC. When the temperature is above 800 K, we find decomposition of CuBTC. CO is the major production species and we also observe the release of CO₂, O₂, 1,3,5-benzenetricarboxylate (C₆H₃(CO₂)₃, BTC) and glassy carbon. These results are consistent with experimental findings, and can be considered to be the first step to understand the reactive adsorption on CuBTC.

e. In general, CuBTC exhibits higher ammonia adsorption capacities than other gas-phase molecules reported in the literature, such as CO₂, CH₄ and H₂. The DFT calculations support the fact that CuBTC hosts a strong adsorption of ammonia. GCMC simulations using classical non-reactive force fields were adopted to study the adsorption isotherms of NH₃ on CuBTC. The simulation results support the trends found experimentally. Nevertheless, higher adsorption capacities are predicted compared to the experimental measurements. This discrepancy is due to the partial collapse of the CuBTC structure upon exposure to ammonia,

which cannot be accounted for in the GCMC simulations with rigid models and classical force fields.

f. With the ReaxFF force field, we have studied the reactive adsorption of NH_3 on the dehydrated CuBTC. We find that the dehydrated CuBTC is hydrostatically stable under water contents up to 4.0 mole equivalents with respect to copper sites and temperatures up to 116 °C. When NH_3 molecules are added to the channel and micropores of CuBTC, they prefer to chemisorb to the copper sites rather than forming a dimer with another NH_3 molecule. The formation of equimolar $\text{Cu}_2(\text{NH}_2)_2$ and $(\text{NH}_4)_3\text{BTC}$ structures is also observed at 348 K, which is in good agreement with previous experimental findings. The CuBTC framework partially collapses upon NH_3 adsorption, but the Cu-Cu dimer structure is stable under the investigated temperatures up to 348 K. The adsorption behavior of $\text{H}_2\text{O}/\text{NH}_3$ mixtures on dehydrated CuBTC is also investigated. Water molecules do not demonstrate a strong interaction with the copper sites of CuBTC, but the existence of water can substantially reduce the amount of chemisorbed NH_3 molecules. The results explain the experimental findings and provide atomic level insight into the removal of ammonia by reactive adsorption on CuBTC frameworks.

9.2. Future research plans

In this thesis, we used the graphene sheet as the base material to study the effects of a single vacancy and functional groups on the adsorption and dissociation of H_2S or NH_3 . It would be also important to study the graphite oxides. As shown in Figure 9.2, the graphite oxide can be considered as a stack of graphene oxides or the oxidization of the graphite materials. The

original interlayer van der Waals interactions as well as the interlayer distances will be affected by the defects or functional groups.

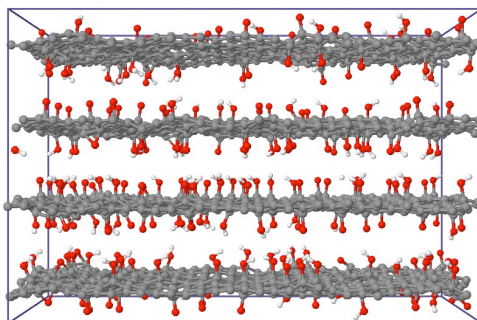


Figure 9.2. A schematic model for graphite oxide material: gray-carbon, red-oxygen, and white-hydrogen.

On the other hand, although we observed the dissociation of H_2S on the vacancy defect of the graphene in Chapter 3, we do not identify such dissociation from RMD calculations in Chapter 5. This is probably due to the steric hindrance effect from the realistic GO models used in Chapter 5, where the H_2S molecules are preferentially adsorbed on the functional groups. It would be of interest to perform RMD calculations to study H_2S interactions with the single vacancy or Stone-Wales defects, as proposed in Figure 9.3. The ReaxFF parameters may need to be re-trained to describe the interactions accurately.

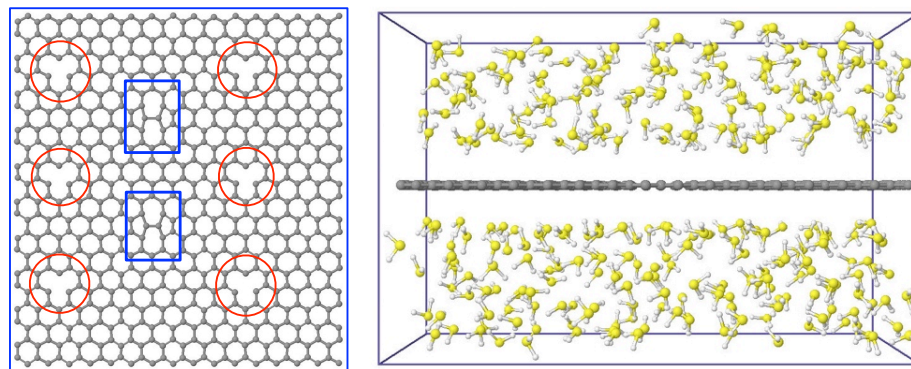


Figure 9.3. The RMD simulation model to study the interactions between H₂S molecules and the graphene with the single vacancy defects (red circles), and Stone-Wales defects (blue rectangles).

It has been shown experimentally that,[36, 205, 228, 278] compared to the use of GO or CuBTC alone, GO/CuBTC nanocomposites demonstrate a significantly enhanced capacity for NH₃ or H₂S adsorption. In particular, GO is believed to lead to an enhancement in nonspecific adsorption owing to the presence of extended graphene type layers and also to an enhancement in strong specific adsorption owing to its acidic character. On the other hand, the MOF can improve the kinetics of adsorption due to the structure of its framework. Moreover, the specific interactions and reactivity can also be enhanced owing to the MOF's chemical composition. A proposed structure of the GO/CuBTC nanocomposite is shown in Figure 9.4, where the structural synergy enhances the physisorption of NH₃.

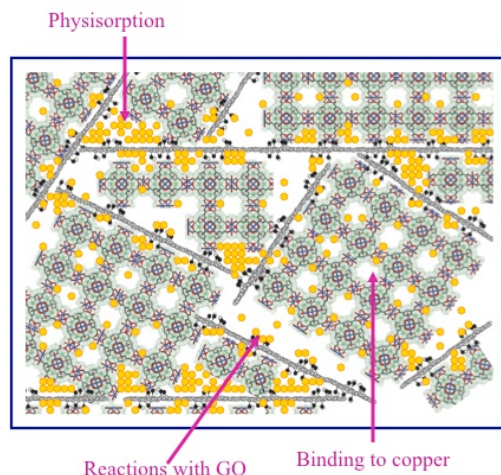


Figure 9.4. A schematic model of the GO/CuBTC composite: the contribution for NH_3 (yellow spheres) adsorption comes from the physisorption in the pores/channels, the chemisorption on the Copper sites of CuBTC, and the reaction with the functional groups of GO. [257]

It is quite challenging to computationally study the properties of GO/CuBTC nanocomposites. The first difficulty is the nanocomposite model itself. Graphite oxide is an amorphous material, while CuBTC is a crystal. It is thus not possible to simply match the lattice parameters and build up the model. Instead, we may have to use the surface-cluster model to study the surface/interface properties between GO and CuBTC. As demonstrated in Figure 9.5, the GO/CuBTC model has many atoms, so that DFT methods cannot efficiently handle such a calculation. We need to develop ReaxFF parameters to describe the GO/CuBTC nanocomposite, and later the interaction between NH_3 and the nanocomposite.

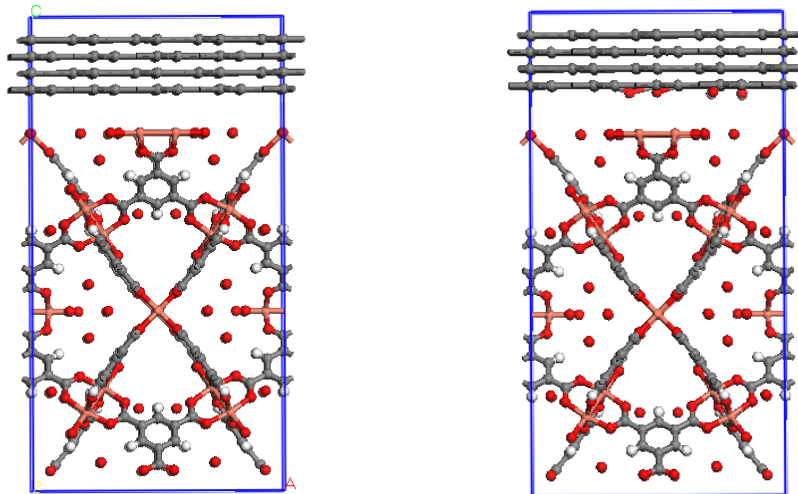


Figure 9.5. Schematic models for the nanocomposite: (Left) Graphite-CuBTC; (Right) GO-CuBTC. The CuBTC MOF crystal is cleaved along the [100] face; four layers of carbons are used to represent the graphite or GO. The color codes are: Carbon (Grey), Oxygen (Red), Hydrogen (White), and Copper (Light Salmon).

REFERENCES

- [1] "National Planning Scenario 8: Chemical Attack - Chlorine Tank Explosion", Homeland Security Council and Department of Homeland Security **2005**.
- [2] "Committee on Transportation and Infrastructure, Subcommittee on Railroads", E.R. Hamberger, Association of American Railroads, Statement before the U.S. House of Representative, **2006**.
- [3] "Catastrophe, Injury, and Insurance: The Impact of Catastrophes on Workers Compensation, Life, and Health Insurance", Risk Management Solution, Inc., **2004**.
- [4] "Chemical Security 101: What You Don't Have Can't Leak, or Be Blown up by Terrorists", Center for American Progress, **2008**.
- [5] "Hazardous Materials Regulations ", The U.S. Department of Transportation, **2012**.
- [6] C.O. Ania, T.J. Bandosz, "Sodium on the Surface of Activated Carbons as a Factor Enhancing Reactive Adsorption of Dibenzothiophene", *Energy & Fuels*, 2006, **20**, 1076-1080.
- [7] M. Seredych, T.J. Bandosz, "Investigation of the Enhancing Effects of Sulfur and/or Oxygen Functional Groups of Nanoporous Carbons on Adsorption of Dibenzothiophenes", *Carbon*, 2011, **49**, 1216-1224.
- [8] A. Max. *Ammonia*, in *Ullmann's Encyclopedia of Industrial Chemistry*. Willey-VCH, Weinheim, **2006**.
- [9] "Toxic Faq Sheet for Ammonia", Agency for Toxic Substances and Disease Registry, **2004**.
- [10] M. Seredych, M. Khine, T.J. Bandosz, "Enhancement in Dibenzothiophene Reactive Adsorption from Liquid Fuel Via Incorporation of Sulfur Heteroatoms into the Nanoporous Carbon Matrix", *Chemistry & Sustainability, Energy & Materials*, 2011, **4**, 139-147.
- [11] M. Seredych, T.J. Bandosz, "Adsorption of Dibenzothiophenes on Activated Carbons with Copper and Iron Deposited on Their Surfaces", *Fuel Processing Technology*, 2010, **91**, 693-701.
- [12] "Toxicological Profile for Hydrogen Sulfide", Agency for Toxic Substances and Disease Registry, **2006**.
- [13] C. Petit, M. Seredych, T.J. Bandosz, "Revisiting the Chemistry of Graphite Oxides and Its Effect on Ammonia Adsorption", *Journal of Materials Chemistry*, 2009, **19**, 9176-9185.

- [14] S. Pizzarello, X. Feng, S. Epstein, J.R. Cronin, "Isotopic Analyses of Nitrogenous Compounds from the Murchison Meteorite - Ammonia, Amines, Amino-Acids, and Polar Hydrocarbons", *Geochimica et Cosmochimica Acta*, 1994, **58**, 5579-5587.
- [15] P. Serp, M. Corrias, P. Kalck, "Carbon Nanotubes and Nanofibers in Catalysis", *Applied Catalysis a-General*, 2003, **253**, 337-358.
- [16] C.V. Hidalgo, H. Itoh, T. Hattori, M. Niwa, Y. Murakami, "Measurement of the Acidity of Various Zeolites by Temperature-Programmed Desorption of Ammonia", *Journal of Catalysis*, 1984, **85**, 362-369.
- [17] E. Bourgeatlamy, P. Massiani, F. Drenzo, P. Espiau, F. Fajula, T.D. Courrieres, "Study of the State of Aluminum in Zeolite-Beta", *Applied Catalysis*, 1991, **72**, 139-152.
- [18] F.J. Arriagada, K. Osseo-Asare, "Synthesis of Nanosize Silica in a Nonionic Water-in-Oil Microemulsion: Effects of the Water/Surfactant Molar Ratio and Ammonia Concentration", *Journal of Colloid and Interface Science*, 1999, **211**, 210-220.
- [19] C. Graf, D.L.J. Vossen, A. Imhof, A. van Blaaderen, "A General Method to Coat Colloidal Particles with Silica", *Langmuir*, 2003, **19**, 6693-6700.
- [20] A. Gutowska, L.Y. Li, Y.S. Shin, C.M.M. Wang, X.H.S. Li, J.C. Linehan, et al., "Nanoscaffold Mediates Hydrogen Release and the Reactivity of Ammonia Borane", *Angewandte Chemie-International Edition*, 2005, **44**, 3578-3582.
- [21] J.B. Peri, "Infrared Study of Adsorption of Ammonia on Dry Gamma-Alumina", *Journal of Physical Chemistry*, 1965, **69**, 231-&.
- [22] L. Singoredjo, R. Korver, F. Kapteijn, J. Moulijn, "Alumina Supported Manganese Oxides for the Low-Temperature Selective Catalytic Reduction of Nitric-Oxide with Ammonia", *Applied Catalysis B-Environmental*, 1992, **1**, 297-316.
- [23] G. Centi, S. Perathoner, "Nature of Active Species in Copper-Based Catalysts and Their Chemistry of Transformation of Nitrogen-Oxides", *Applied Catalysis a-General*, 1995, **132**, 179-259.
- [24] D. Britt, D. Tranchemontagne, O.M. Yaghi, "Metal-Organic Frameworks with High Capacity and Selectivity for Harmful Gases", *Proceedings of the National Academy of Sciences of the United States of America*, 2008, **105**, 11623-11627.
- [25] G.W. Peterson, G.W. Wagner, A. Balboa, J. Mahle, T. Sewell, C.J. Karwacki, "Ammonia Vapor Removal by Cu-3(Btc)(2) and Its Characterization by Mas Nmr", *Journal of Physical Chemistry C*, 2009, **113**, 13906-13917.

- [26] C. Petit, T.J. Bandoz, "Mof-Graphite Oxide Composites: Combining the Uniqueness of Graphene Layers and Metal-Organic Frameworks", *Advanced Materials*, 2009, **21**, 4753-+.
- [27] Z. Li, G. Zhu, G. Lu, S. Qiu, X. Yao, "Ammonia Borane Confined by a Metal-Organic Framework for Chemical Hydrogen Storage: Enhancing Kinetics and Eliminating Ammonia", *Journal of the American Chemical Society*, 2010, **132**, 1490-+.
- [28] M.M. Dubinin, H.F. Stoeckli, "Homogeneous and Heterogeneous Micropore Structures in Carbonaceous Adsorbents", *Journal of Colloid and Interface Science*, 1980, **75**, 34-42.
- [29] S.J.T. Pollard, G.D. Fowler, C.J. Sollars, R. Perry, "Low-Cost Adsorbents for Waste and Waste-Water Treatment - a Review", *Science of the Total Environment*, 1992, **116**, 31-52.
- [30] J. Helminen, J. Helenius, E. Paatero, I. Turunen, "Adsorption Equilibria of Ammonia Gas on Inorganic and Organic Sorbents at 298.15 K", *Journal of Chemical and Engineering Data*, 2001, **46**, 391-399.
- [31] D.E. Richardson, H.R. Yao, K.M. Frank, D.A. Bennett, "Equilibria, Kinetics, and Mechanism in the Bicarbonate Activation of Hydrogen Peroxide: Oxidation of Sulfides by Peroxymonocarbonate", *Journal of the American Chemical Society*, 2000, **122**, 1729-1739.
- [32] T.J. Bandoz, "On the Adsorption/Oxidation of Hydrogen Sulfide on Activated Carbons at Ambient Temperatures", *Journal of Colloid and Interface Science*, 2002, **246**, 1-20.
- [33] C. Petit, B. Levasseur, B. Mendoza, T.J. Bandoz, "Reactive Adsorption of Acidic Gases on Mof/Graphite Oxide Composites", *Microporous and Mesoporous Materials*, 2012, **154**, 107-112.
- [34] C. Petit, L. Huang, J. Jagiello, J. Kenvin, K.E. Gubbins, T.J. Bandoz, "Toward Understanding Reactive Adsorption of Ammonia on Cu-Mof/Graphite Oxide Nanocomposites", *Langmuir*, 2011, **27**, 13043-13051.
- [35] T.J. Bandoz, C. Petit, "Mof/Graphite Oxide Hybrid Materials: Exploring the New Concept of Adsorbents and Catalysts", *Adsorption-Journal of the International Adsorption Society*, 2011, **17**, 5-16.
- [36] C. Petit, B. Mendoza, T.J. Bandoz, "Reactive Adsorption of Ammonia on Cu-Based Mof/Graphene Composites", *Langmuir*, 2010, **26**, 15302-15309.
- [37] C. Petit, K. Kante, T.J. Bandoz, "The Role of Sulfur-Containing Groups in Ammonia Retention on Activated Carbons", *Carbon*, 2010, **48**, 654-667.

- [38] T.C. Dinadayalane, J. Leszczynski, "Remarkable Diversity of Carbon-Carbon Bonds: Structures and Properties of Fullerenes, Carbon Nanotubes, and Graphene", *Structural Chemistry*, 2010, **21**, 1155-1169.
- [39] H.E. Romero, P. Joshi, A.K. Gupta, H.R. Gutierrez, M.W. Cole, S.A. Tadigadapa, et al., "Adsorption of Ammonia on Graphene", *Nanotechnology*, 2009, **20**, 245501.
- [40] P. Cabrera-Sanfeliu, G.R. Darling, "Dissociative Adsorption of Water at Vacancy Defects in Graphite", *Journal of Physical Chemistry C*, 2007, **111**, 18258-18263.
- [41] A. Ghosh, D.J. Late, L.S. Panchakarla, A. Govindaraj, C.N.R. Rao, "NO₂ and Humidity Sensing Characteristics of Few-Layer Graphenes", *Journal of Experimental Nanoscience*, 2009, **4**, 313-322.
- [42] O. Leenaerts, B. Partoens, F.M. Peeters, "Adsorption of H₂O, NH₃, Co, Ni, and Cu on Graphene: A First-Principles Study", *Physical Review B*, 2008, **77**, 125416.
- [43] B. Huang, Z. Li, Z. Liu, G. Zhou, S. Hao, J. Wu, et al., "Adsorption of Gas Molecules on Graphene Nanoribbons and Its Implication for Nanoscale Molecule Sensor", *Journal of Physical Chemistry C*, 2008, **112**, 13442-13446.
- [44] F. Schedin, A.K. Geim, S.V. Morozov, E.W. Hill, P. Blake, M.I. Katsnelson, et al., "Detection of Individual Gas Molecules Adsorbed on Graphene", *Nature Materials*, 2007, **6**, 652-655.
- [45] T.O. Wehling, K.S. Novoselov, S.V. Morozov, E.E. Vdovin, M.I. Katsnelson, A.K. Geim, et al., "Molecular Doping of Graphene", *Nano Letters*, 2008, **8**, 173-177.
- [46] A. Lerf, H.Y. He, M. Forster, J. Klinowski, "Structure of Graphite Oxide Revisited", *Journal of Physical Chemistry B*, 1998, **102**, 4477-4482.
- [47] M. Eddaoudi, D.B. Moler, H.L. Li, B.L. Chen, T.M. Reineke, M. O'Keeffe, et al., "Modular Chemistry: Secondary Building Units as a Basis for the Design of Highly Porous and Robust Metal-Organic Carboxylate Frameworks", *Accounts of Chemical Research*, 2001, **34**, 319-330.
- [48] H. Li, M. Eddaoudi, M. O'Keeffe, O.M. Yaghi, "Design and Synthesis of an Exceptionally Stable and Highly Porous Metal-Organic Framework", *Nature*, 1999, **402**, 276-279.
- [49] K.K. Tanabe, Z. Wang, S.M. Cohen, "Systematic Functionalization of a Metal-Organic Framework Via a Postsynthetic Modification Approach", *Journal of the American Chemical Society*, 2008, **130**, 8508-8517.

- [50] D. Frarrusseng. *Metal-Organic Frameworks: Applications from Catalysis to Gas Storage*. Wiley-VCH, Weinheim, **2011**.
- [51] K. Chenoweth, A.C.T. van Duin, W.A. Goddard, III, "Reaxff Reactive Force Field for Molecular Dynamics Simulations of Hydrocarbon Oxidation", *Journal of Physical Chemistry A*, 2008, **112**, 1040-1053.
- [52] K. Schlichte, T. Kratzke, S. Kaskel, "Improved Synthesis, Thermal Stability and Catalytic Properties of the Metal-Organic Framework Compound Cu₃(Btc)(2)", *Microporous and Mesoporous Materials*, 2004, **73**, 81-88.
- [53] A. Corma, M. Iglesias, F.X. Llabrés i Xamena, F. Sánchez, "Cu and Au Metal–Organic Frameworks Bridge the Gap between Homogeneous and Heterogeneous Catalysts for Alkene Cyclopropanation Reactions", *Chemistry – A European Journal*, 2010, **16**, 9789-9795.
- [54] A. Dhakshinamoorthy, M. Alvaro, H. Chevreau, P. Horcajada, T. Devic, C. Serre, et al., "Iron(III) Metal-Organic Frameworks as Solid Lewis Acids for the Isomerization of Alpha-Pinene Oxide", *Catalysis Science & Technology*, 2012, **2**, 324-330.
- [55] S. Archmann, G. Hagen, M. Hammerle, I.M. Malkowsky, C. Kiener, R. Moos, "Sulfur Removal from Low-Sulfur Gasoline and Diesel Fuel by Metal-Organic Frameworks", *Chemical Engineering & Technology*, 2010, **33**, 275-280.
- [56] S. Achmann, G. Hagen, M. Hämmerle, I.M. Malkowsky, C. Kiener, R. Moos, "Sulfur Removal from Low-Sulfur Gasoline and Diesel Fuel by Metal-Organic Frameworks", *Chemical Engineering & Technology*, 2010, **33**, 275-280.
- [57] D. Bradshaw, A. Garai, J. Huo, "Metal-Organic Framework Growth at Functional Interfaces: Thin Films and Composites for Diverse Applications", *Chemical Society Reviews*, 2012, **41**, 2344-2381.
- [58] P. Hohenberg, W. Kohn, "Inhomogeneous Electron Gas", *Physical Review B*, 1964, **136**, B864.
- [59] W. Kohn, L.J. Sham, "Self-Consistent Equations Including Exchange and Correlation Effects", *Physical Review*, 1965, **140**, 1133.
- [60] G. Grosso, G.P. Parravicini. *Solid State Physics* Academic Press, San Diego, **2000**.
- [61] A. Szabo, N.S. Ostlund. *Modern Quantum Chemistry*. McGraw-Hill, New York, **1989**.
- [62] R.G. Parr, W.T. Yang. *Density-Functional Theory of Atoms and Molecules* Oxford University Press New York, **1989**.

- [63] D. Sholl, J.A. Stechel. *Density Functional Theory: A Practical Introduction* Wiley-Interscience New Jersey, **2009**.
- [64] R.G. Parr, "Density Functional Theory", *Annual Review of Physical Chemistry*, 1983, **34**, 631-656.
- [65] K. Capelle, "A Bird's-Eye View of Density-Functional Theory", *Brazilian Journal of Physics*, 2006, **36**, 1318-1343.
- [66] R.O. Jones, O. Gunnarsson, "The Density Functional Formalism, Its Applications and Prospects", *Reviews of Modern Physics*, 1989, **61**, 689-746.
- [67] W. Kohn, A.D. Becke, R.G. Parr, "Density Functional Theory of Electronic Structure", *Journal of Physical Chemistry*, 1996, **100**, 12974-12980.
- [68] N. Argaman, G. Makov, "Density Functional Theory: An Introduction", *American Journal of Physics*, 2000, **68**, 69-79.
- [69] H. Eschrig, W.E. Pickett, "Density Functional Theory of Magnetic Systems Revisited", *Solid State Communications*, 2001, **118**, 123-127.
- [70] A. Gorling, "Density-Functional Theory for Excited States", *Physical Review A*, 1996, **54**, 3912-3915.
- [71] M. Born, J.R. Oppenheimer, "On the Quantum Theory of Molecules ", *Annalen der Physik*, 1927, **84**.
- [72] A.C.T. van Duin, V.S. Bryantsev, M.S. Diallo, W.A. Goddard, O. Rahaman, D.J. Doren, et al., "Development and Validation of a Reaxff Reactive Force Field for Cu Cation/Water Interactions and Copper Metal/Metal Oxide/Metal Hydroxide Condensed Phases", *Journal of Physical Chemistry A*, 2010, **114**, 9507-9514.
- [73] E. Teller, "On Stability of Molecules in Thomas-Fermi Theory", *Reviews of Modern Physics*, 1962, **34**, 627-631.
- [74] J.C. Slater, "A Simplification of the Hartree-Fock Method", *Physical Review*, 1951, **81**, 385-390.
- [75] O. Gunnarsson, B.I. Lundqvist, "Exchange and Correlation in Atoms, Molecules, and Solids by Spin-Density Functional Formalism", *Physical Review B*, 1976, **13**, 4274-4298.
- [76] T. Ziegler, "Approximate Density Functional Theory as a Practical Tool in Molecular Energetics and Dynamics", *Chemical Reviews*, 1991, **91**, 651-667.

- [77] C.W. Bauschlicher, "A Comparison of the Accuracy of Different Functionals", *Chemical Physics Letters*, 1995, **246**, 40-44.
- [78] A.D. Becke, "Density-Functional Exchange-Energy Approximation with Correct Asymptotic-Behavior", *Physical Review A*, 1988, **38**, 3098-3100.
- [79] T. Petrenko, K. Ray, K.E. Wieghardt, F. Neese, "Vibrational Markers for the Open-Shell Character of Transition Metal Bis-Dithiolenes: An Infrared, Resonance Raman, and Quantum Chemical Study", *Journal of the American Chemical Society*, 2006, **128**, 4422-4436.
- [80] M. Shanmugasundaram, M. Puranik, "Computational Prediction of Vibrational Spectra of Normal and Modified DNA Nucleobases", *Journal of Raman Spectroscopy*, 2009, **40**, 1726-1748.
- [81] L.Q. Zhang, H.R. Li, "Progress of Investigations on Structures and Interactions of Ionic Liquids by Infrared Spectroscopy and Raman Spectroscopy", *Acta Physico-Chimica Sinica*, 2010, **26**, 2877-2889.
- [82] P.E.M. Siegbahn, M.R.A. Blomberg, "Density Functional Theory of Biologically Relevant Metal Centers", *Annual Review of Physical Chemistry*, 1999, **50**, 221-249.
- [83] S. Suhai, "Density-Functional Studies of the Hydrogen-Bonded Network in an Infinite Water Polymer", *Journal of Physical Chemistry*, 1995, **99**, 1172-1181.
- [84] J. Gierschner, J. Cornil, H.J. Egelhaaf, "Optical Bandgaps of Pi-Conjugated Organic Materials at the Polymer Limit: Experiment and Theory", *Advanced Materials*, 2007, **19**, 173-191.
- [85] J.Z. Wu, Z.D. Li. Density-Functional Theory for Complex Fluids. *Annual Review of Physical Chemistry* 2007:85-112.
- [86] X.F. Xu, D.P. Cao, J.Z. Wu, "Density Functional Theory for Predicting Polymeric Forces against Surface Fouling", *Soft Matter*, 2010, **6**, 4631-4646.
- [87] R. Shah, M.C. Payne, M.H. Lee, J.D. Gale, "Understanding the Catalytic Behavior of Zeolites: A First-Principles Study of the Adsorption of Methanol", *Science*, 1996, **271**, 1395-1397.
- [88] D.Y. Wu, X.M. Liu, Y.F. Huang, B. Ren, X. Xu, Z.Q. Tian, "Surface Catalytic Coupling Reaction of P-Mercaptoaniline Linking to Silver Nanostructures Responsible for Abnormal SERS Enhancement: A Dft Study", *Journal of Physical Chemistry C*, 2009, **113**, 18212-18222.

- [89] W. Liu, Q. Jiang, "Density Functional Theory Study on Electric Field Induced Structure Variations, Binding and Catalytic Properties in Several Low-Dimensional Systems", *Journal of Computational and Theoretical Nanoscience*, 2010, **7**, 2225-2261.
- [90] M. Saliccioli, M. Stamatakis, S. Caratzoulas, D.G. Vlachos, "A Review of Multiscale Modeling of Metal-Catalyzed Reactions: Mechanism Development for Complexity and Emergent Behavior", *Chemical Engineering Science*, 2011, **66**, 4319-4355.
- [91] J.L. Gong, C.B. Mullins, "Surface Science Investigations of Oxidative Chemistry on Gold", *Accounts of Chemical Research*, 2009, **42**, 1063-1073.
- [92] C.S. Yeung, W.Q. Tian, L.V. Liu, Y.A. Wang, "Chemistry of Single-Walled Carbon Nanotubes", *Journal of Computational and Theoretical Nanoscience*, 2009, **6**, 1213-1235.
- [93] G. Lanzani, R. Martinazzo, G. Materzanini, I. Pino, G.F. Tantardini, "Chemistry at Surfaces: From Ab Initio Structures to Quantum Dynamics", *Theoretical Chemistry Accounts*, 2007, **117**, 805-825.
- [94] J. Hafner, "Ab-Initio Simulations of Materials Using Vasp: Density-Functional Theory and Beyond", *Journal of Computational Chemistry*, 2008, **29**, 2044-2078.
- [95] E.E. Santiso, K.E. Gubbins, "Multi-Scale Molecular Modeling of Chemical Reactivity", *Molecular Simulation*, 2004, **30**, 699-748.
- [96] R. Car, M. Parrinello, "Unified Approach for Molecular-Dynamics and Density-Functional Theory", *Physical Review Letters*, 1985, **55**, 2471-2474.
- [97] W. Kohn, Y. Meir, D.E. Makarov, "Vanderwaals Energies in Density Functional Theory", *Physical Review Letters*, 1998, **80**, 4153-4156.
- [98] S.F. Sousa, P.A. Fernandes, M.J. Ramos, "General Performance of Density Functionals", *Journal of Physical Chemistry A*, 2007, **111**, 10439-10452.
- [99] A.J. Cohen, P. Mori-Sanchez, W. Yang, "Insights into Current Limitations of Density Functional Theory", *Science*, 2008, **321**, 792-794.
- [100] A.J. Cohen, P. Mori-Sanchez, W. Yang, "Challenges for Density Functional Theory", *Chemical Reviews*, 2012, **112**, 289-320.
- [101] D. Porezag, M.R. Pederson, A.Y. Liu, "The Accuracy of the Pseudopotential Approximation within Density-Functional Theory", *Physica Status Solidi B-Basic Research*, 2000, **217**, 219-230.
- [102] A.C.T. van Duin, S. Dasgupta, F. Lorant, W.A. Goddard, "Reaxff: A Reactive Force Field for Hydrocarbons", *Journal of Physical Chemistry A*, 2001, **105**, 9396-9409.

- [103] J. Tersoff, "Chemical Order in Amorphous-Silicon Carbide", *Physical Review B*, 1994, **49**, 16349-16352.
- [104] W.J. Mortier, K. Vangenechten, J. Gasteiger, "Electronegativity Equalization - Application and Parametrization", *Journal of the American Chemical Society*, 1985, **107**, 829-835.
- [105] S. Bashkova, A. Bagreev, D.C. Locke, T.J. Bandosz, "Adsorption of So₂ on Sewage Sludge-Derived Materials", *Environmental Science & Technology*, 2001, **35**, 3263-3269.
- [106] S. Cheung, W.Q. Deng, A.C.T. van Duin, W.A. Goddard, "Reaxff(Mgh) Reactive Force Field for Magnesium Hydride Systems", *Journal of Physical Chemistry A*, 2005, **109**, 851-859.
- [107] GRASP, Available from: <http://www.sdsc.edu/News Items/PR100903.html>
- [108] T.J. Bandosz, M. Sereych, J. Allen, J. Wood, E. Rosenberg, "Silica-Polyamine-Based Carbon Composite Adsorbents as Media for Effective Hydrogen Sulfide Adsorption/Oxidation", *Chemistry of Materials*, 2007, **19**, 2500-2511.
- [109] J.C. Fogarty, H.M. Aktulga, A.Y. Grama, A.C.T. van Duin, S.A. Pandit, "A Reactive Molecular Dynamics Simulation of the Silica-Water Interface", *Journal of Chemical Physics*, 2010, **132**, 174704.
- [110] H.M. Aktulga, J.C. Fogarty, S.A. Pandit, A.Y. Grama, "Parallel Reactive Molecular Dynamics: Numerical Methods and Algorithmic Techniques", *Parallel Computing*, 2012, **38**, 245-259.
- [111] H.M. Aktulga, S.A. Pandit, A.C.T. van Duin, A.Y. Grama, "Reactive Molecular Dynamics: Numerical Methods and Algorithmic Techniques", *Siam Journal on Scientific Computing*, 2012, **34**, C1-C23.
- [112] Y. El-Sayed, T.J. Bandosz, "Acetaldehyde Adsorption on Nitrogen-Containing Activated Carbons", *Langmuir*, 2002, **18**, 3213-3218.
- [113] A. Bagreev, T.J. Bandosz, "A Role of Sodium Hydroxide in the Process of Hydrogen Sulfide Adsorption/Oxidation on Caustic-Impregnated Activated Carbons", *Industrial & Engineering Chemistry Research*, 2002, **41**, 672-679.
- [114] A. Bagreev, S. Bashkova, T.J. Bandosz, "Adsorption of So₂ on Activated Carbons: The Effect of Nitrogen Functionality and Pore Sizes", *Langmuir*, 2002, **18**, 1257-1264.
- [115] A. Bagreev, S. Bashkova, B. Reznik, V. Zibat, T.J. Bandosz. Heterogeneity of Sewage Sludge Derived Materials as a Factor Governing Their Performance as Adsorbents of

Acidic Gases. In: RodriguezReinoso F, McEnaney B, Rouquerol J, Unger K, eds. *Characterization of Porous Solids Vi* 2002:217-224.

[116] Y. El-Sayed, T.J. Bandosz. An Igc and Ta Study of Acetaldehyde Adsorption on Activated Carbons. In: RodriguezReinoso F, McEnaney B, Rouquerol J, Unger K, eds. *Characterization of Porous Solids Vi* 2002:247-254.

[117] H. Sun, "Compass: An Ab Initio Force-Field Optimized for Condensed-Phase Applicationsoverview with Details on Alkane and Benzene Compounds", *The Journal of Physical Chemistry B*, 1998, **102**, 7338-7364.

[118] W.L. Jorgensen, D.S. Maxwell, J. Tirado-Rives, "Development and Testing of the Opls All-Atom Force Field on Conformational Energetics and Properties of Organic Liquids", *Journal of the American Chemical Society*, 1996, **118**, 11225-11236.

[119] Y. El-Sayed, T.J. Bandosz, "A Study of Acetaldehyde Adsorption on Activated Carbons", *Journal of Colloid and Interface Science*, 2001, **242**, 44-51.

[120] J.K. Brennan, T.J. Bandosz, K.T. Thomson, K.E. Gubbins, "Water in Porous Carbons", *Colloids and Surfaces a-Physicochemical and Engineering Aspects*, 2001, **187**, 539-568.

[121] A. Bagreev, D.C. Locke, T.J. Bandosz, "H2s Adsorption/Oxidation on Adsorbents Obtained from Pyrolysis of Sewage-Sludge-Derived Fertilizer Using Zinc Chloride Activation", *Industrial & Engineering Chemistry Research*, 2001, **40**, 3502-3510.

[122] S. Nose, "A Unified Formulation of the Constant Temperature Molecular-Dynamics Methods", *Journal of Chemical Physics*, 1984, **81**, 511-519.

[123] W.G. Hoover, "Canonical Dynamics - Equilibrium Phase-Space Distributions", *Physical Review A*, 1985, **31**, 1695-1697.

[124] H.J.C. Berendsen, J.P.M. Postma, W.F. Vangunsteren, A. Dinola, J.R. Haak, "Molecular-Dynamics with Coupling to an External Bath", *Journal of Chemical Physics*, 1984, **81**, 3684-3690.

[125] J.Y. Jang, R.M. Stratt, "The Short-Time Dynamics of Molecular Reorientation in Liquids. I. The Instantaneous Generalized Langevin Equation", *Journal of Chemical Physics*, 2000, **112**, 7524-7537.

[126] F. Conrad, M. Grothaus, "N/V-Limit for Langevin Dynamics in Continuum", *Reviews in Mathematical Physics*, 2011, **23**, 1-51.

[127] M. Parrinello, A. Rahman, "Polymorphic Transitions in Single-Crystals - a New Molecular-Dynamics Method", *Journal of Applied Physics*, 1981, **52**, 7182-7190.

- [128] M. Parrinello, A. Rahman, "Crystal-Structure and Pair Potentials - a Molecular-Dynamics Study", *Physical Review Letters*, 1980, **45**, 1196-1199.
- [129] B. Smit, R. Krishna, "Monte Carlo Simulations in Zeolites", *Current Opinion in Solid State & Materials Science*, 2001, **5**, 455-461.
- [130] R. Krishna, R. Baur, "Modelling Issues in Zeolite Based Separation Processes", *Separation and Purification Technology*, 2003, **33**, 213-254.
- [131] C. Volkringer, T. Loiseau, N. Guillou, G. Ferey, E. Elkaim, A. Vimont, "Xrd and Ir Structural Investigations of a Particular Breathing Effect in the Mof-Type Gallium Terephthalate Mil-53(Ga)", *Dalton Transactions*, 2009, 2241-2249.
- [132] M. Meilikhov, K. Yusenko, R.A. Fischer, "Incorporation of Metallocenes into the Channel Structured Metal-Organic Frameworks Mil-53(Al) and Mil-47(V)", *Dalton Transactions*, 2010, **39**, 10990-10999.
- [133] T. Remy, G.V. Baron, J.F.M. Denayer, "Modeling the Effect of Structural Changes During Dynamic Separation Processes on Mofs", *Langmuir*, 2011, **27**, 13064-13071.
- [134] S.J. Wang, L. Li, J.Y. Zhang, X.C. Yuan, C.Y. Su, "Anion-Tuned Sorption and Catalytic Properties of a Soft Metal-Organic Solid with Polycatenated Frameworks", *Journal of Materials Chemistry*, 2011, **21**, 7098-7104.
- [135] B. Mu, F. Li, Y.G. Huang, K.S. Walton, "Breathing Effects of Co₂ Adsorption on a Flexible 3d Lanthanide Metal-Organic Framework", *Journal of Materials Chemistry*, 2012, **22**, 10172-10178.
- [136] D. Frenkel, B. Smit. *Understanding Molecular Simulation: From Algorithms to Applications* Academic Press, **2001**.
- [137] D.P. Kroese, T. Taimre, Z.I. Botev. *Handbook of Monte Carlo Methods* Wiley, **2011**.
- [138] F.X. Coudert, A. Boutin, M. Jeffroy, C. Mellot-Draznieks, A.H. Fuchs, "Thermodynamic Methods and Models to Study Flexible Metal-Organic Frameworks", *Chemphyschem*, 2011, **12**, 247-258.
- [139] K. Kiyohara, K. Asaka, "Monte Carlo Simulation of Porous Electrodes in the Constant Voltage Ensemble", *Journal of Physical Chemistry C*, 2007, **111**, 15903-15909.
- [140] Z. Karimzadeh, S.A.A. Hosseini, F. Deyhimi, "Using Monte Carlo Simulation to Compute Osmotic Coefficients of Aqueous Solutions of Ionic Liquids", *Chemical Physics*, 2010, **371**, 55-59.

- [141] S. Schreiber, R. Hentschke, "Monte Carlo Simulation of Osmotic Equilibria", *Journal of Chemical Physics*, 2011, **135**, 134106.
- [142] J. Zang, S. Nair, D.S. Sholl, "Osmotic Ensemble Methods for Predicting Adsorption-Induced Structural Transitions in Nanoporous Materials Using Molecular Simulations", *Journal of Chemical Physics*, 2011, **134**, 184103.
- [143] J.C. Love, L.A. Estroff, J.K. Kriebel, R.G. Nuzzo, G.M. Whitesides, "Self-Assembled Monolayers of Thiolates on Metals as a Form of Nanotechnology", *Chemical Reviews*, 2005, **105**, 1103-1169.
- [144] C. Fushimi, M. Goto, A. Tsutsumi, J. Hayashi, T. Chiba, "Steam Gasification Characteristics of Coal with Rapid Heating", *Journal of Analytical and Applied Pyrolysis*, 2003, **70**, 185-197.
- [145] P.N. Abufager, P.G. Lustemberg, C. Crespos, H.F. Busnengo, "Dft Study of Dissociative Adsorption of Hydrogen Sulfide on Cu(111) and Au(111)", *Langmuir*, 2008, **24**, 14022-14026.
- [146] M.J.S. Spencer, N. Todorova, I. Yarovsky, "H₂s Dissociation on the Fe(100) Surface: An Ab Initio Molecular Dynamics Study", *Surface Science*, 2008, **602**, 1547-1553.
- [147] M.J.S. Spencer, I. Yarovsky, "Ab Initio Molecular Dynamics Study of H₂s Dissociation on the Fe(110) Surface", *Journal of Physical Chemistry C*, 2007, **111**, 16372-16378.
- [148] C.Y. Qin, J.L. Whitten, "Interaction of S, Sh and H₂s with Ag(100)", *Surface Science*, 2005, **588**, 83-91.
- [149] M.P. Hyman, B.T. Loveless, J.W. Medlin, "A Density Functional Theory Study of H₂s Decomposition on the (111) Surfaces of Model Pd-Alloys", *Surface Science*, 2007, **601**, 5382-5393.
- [150] W.-F. Huang, H.-T. Chen, M.C. Lin, "Density Functional Theory Study of the Adsorption and Reaction of H₂s on TiO₂ Rutile (110) and Anatase (101) Surfaces", *Journal of Physical Chemistry C*, 2009, **113**, 20411-20420.
- [151] H.L. Lu, W. Chen, S.J. Ding, M. Xu, D.W. Zhang, L.K. Wang, "Quantum Chemical Study of Adsorption and Dissociation of H₂s on the Gallium-Rich GaAs (001)-4 X 2 Surface", *Journal of Physical Chemistry B*, 2006, **110**, 9529-9533.
- [152] M.Y. Sun, A.E. Nelson, J. Adjaye, "Adsorption and Dissociation of H₂ and H₂s on MoS₂ and NiMoS Catalysts", *Catalysis Today*, 2005, **105**, 36-43.

- [153] D. Borisova, V. Antonov, A. Proykova, "Hydrogen Sulfide Adsorption on a Defective Graphene", *International Journal of Quantum Chemistry*, 2012, 24077.
- [154] C.T. Lee, W.T. Yang, R.G. Parr, "Development of the Colle-Salvetti Correlation-Energy Formula into a Functional of the Electron-Density", *Physical Review B*, 1988, **37**, 785-789.
- [155] J.E. Mueller, A.C.T. van Duin, W.A. Goddard, "Competing, Coverage-Dependent Decomposition Pathways for C₂Hy Species on Nickel (111)", *Journal of Physical Chemistry C*, 2010, **114**, 20028-20041.
- [156] D. Vanderbilt, "Soft Self-Consistent Pseudopotentials in a Generalized Eigenvalue Formalism", *Physical Review B*, 1990, **41**, 7892-7895.
- [157] G. Mills, H. Jonsson, G.K. Schenter, "Reversible Work Transition-State Theory - Application to Dissociative Adsorption of Hydrogen", *Surface Science*, 1995, **324**, 305-337.
- [158] G. Henkelman, B.P. Uberuaga, H. Jonsson, "A Climbing Image Nudged Elastic Band Method for Finding Saddle Points and Minimum Energy Paths", *Journal of Chemical Physics*, 2000, **113**, 9901-9904.
- [159] P. Giannozzi, S. Baroni, N. Bonini, M. Calandra, R. Car, C. Cavazzoni, et al., "Quantum Espresso: A Modular and Open-Source Software Project for Quantum Simulations of Materials", *Journal of Physics-Condensed Matter*, 2009, **21**, 395502.
- [160] R.C. Shiell, X.K. Hu, Q.J. Hu, J.W. Hepburn, "A Determination of the Bond Dissociation Energy (D₀(H-Sh)): Threshold Ion-Pair Production Spectroscopy (Tipps) of a Triatomic Molecule", *Journal of Physical Chemistry A*, 2000, **104**, 4339-4342.
- [161] J.A. Rodriguez, S. Chaturvedi, M. Kuhn, J. Hrbek, "Reaction of H₂s and S-2 with Metal/Oxide Surfaces: Band-Gap Size and Chemical Reactivity", *Journal of Physical Chemistry B*, 1998, **102**, 5511-5519.
- [162] V. Mokrushin, W. Tsang, Chemrate, Version 1.5.8, Available from: <http://mokrushin.com/ChemRate/chemrate.html>
- [163] L. Pauling. *The Nature of the Chemical Bond, and the Structure of Molecules and Crystals: An Introduction to Modern Structural Chemistry*. Cornell University Press, **1960**.
- [164] M.Z.S. Flores, P.A.S. Autreto, S.B. Legoas, D.S. Galvao, "Graphene to Graphane: A Theoretical Study", *Nanotechnology*, 2009, **20**.
- [165] Y. Yu, S. Dixon-Warren, N. Astle, "Molecular-Beam Study of the Adsorption and Desorption of Hydrogen Sulfide on Ag{111}", *Chemical Physics Letters*, 1999, **312**, 455-460.

- [166] A.J. Leavitt, T.P. Beebe, "Chemical-Reactivity Studies of Hydrogen-Sulfide on Au(111)", *Surface Science*, 1994, **314**, 23-33.
- [167] C.T. Campbell, B.E. Koel, "H₂S/Cu(111) - a Model Study of Sulfur Poisoning of Water-Gas Shift Catalysts", *Surface Science*, 1987, **183**, 100-112.
- [168] D.R. Alfonso, "First-Principles Studies of H₂S Adsorption and Dissociation on Metal Surfaces", *Surface Science*, 2008, **602**, 2758-2768.
- [169] M.K. Kostov, E.E. Santiso, A.M. George, K.E. Gubbins, M.B. Nardelli, "Dissociation of Water on Defective Carbon Substrates", *Physical Review Letters*, 2005, **95**.
- [170] B.C. Brodie, "Sur Le Poids Atomique Du Graphite", *Ann Chim Phys*, 1860, **59**, 466.
- [171] M. Seredych, T.J. Bandosz, "Mechanism of Ammonia Retention on Graphite Oxides: Role of Surface Chemistry and Structure", *Journal of Physical Chemistry C*, 2007, **111**, 15596-15604.
- [172] M. Seredych, M. van der Merwe, T.J. Bandosz, "Effects of Surface Chemistry on the Reactive Adsorption of Hydrogen Cyanide on Activated Carbons", *Carbon*, 2009, **47**, 2456-2465.
- [173] D.A. Dikin, S. Stankovich, E.J. Zimney, R.D. Piner, G.H.B. Dommett, G. Evmenenko, et al., "Preparation and Characterization of Graphene Oxide Paper", *Nature*, 2007, **448**, 457-460.
- [174] S. Stankovich, D.A. Dikin, G.H.B. Dommett, K.M. Kohlhaas, E.J. Zimney, E.A. Stach, et al., "Graphene-Based Composite Materials", *Nature*, 2006, **442**, 282-286.
- [175] D.W. Boukhvalov, M.I. Katsnelson, "Modeling of Graphite Oxide", *Journal of the American Chemical Society*, 2008, **130**, 10697-10701.
- [176] T. Cassagneau, F. Guerin, J.H. Fendler, "Preparation and Characterization of Ultrathin Films Layer-by-Layer Self-Assembled from Graphite Oxide Nanoplatelets and Polymers", *Langmuir*, 2000, **16**, 7318-7324.
- [177] H.Y. He, J. Klinowski, M. Forster, A. Lerf, "A New Structural Model for Graphite Oxide", *Chemical Physics Letters*, 1998, **287**, 53-56.
- [178] R.J.W.E. Lahaye, H.K. Jeong, C.Y. Park, Y.H. Lee, "Density Functional Theory Study of Graphite Oxide for Different Oxidation Levels", *Physical Review B*, 2009, **79**.
- [179] T. Nakajima, A. Mabuchi, R. Hagiwara, "A New Structure Model of Graphite Oxide", *Carbon*, 1988, **26**, 357-361.

- [180] T. Nakajima, Y. Matsuo, "Formation Process and Structure of Graphite Oxide", *Carbon*, 1994, **32**, 469-475.
- [181] T. Szabo, E. Tombacz, E. Illes, I. Dekany, "Enhanced Acidity and Ph-Dependent Surface Charge Characterization of Successively Oxidized Graphite Oxides", *Carbon*, 2006, **44**, 537-545.
- [182] D.R. Dreyer, S. Park, C.W. Bielawski, R.S. Ruoff, "The Chemistry of Graphene Oxide", *Chemical Society Reviews*, 2010, **39**, 228-240.
- [183] U. Hofmann, R. Holst, "The Acidic Nature and the Methylation of Graphitoxide", *Berichte der deutschen chemischen Gesellschaft*, 1939, **72**, 754-771.
- [184] G. Ruess, "Uber Das Graphitoxhydroxyd (Graphitoxyd)", *Monatsch Chem*, 1946, **76**, 381-417.
- [185] W. Scholz, H.P. Boehm, "Graphite Oxide .6. Structure of Graphite Oxide", *Zeitschrift Fur Anorganische Und Allgemeine Chemie*, 1969, **369**, 327-339.
- [186] L. Staudenmaier, "Verfahren Zur Darstellung Der Graphitsaure", *Berichte der deutschen chemischen Gesellschaft*, 1898, **31**, 1481-1487.
- [187] W.S. Hummers, R.E. Offeman, "Preparation of Graphitic Oxide", *Journal of the American Chemical Society*, 1958, **80**, 1339-1339.
- [188] A. Laio, M. Parrinello, "Escaping Free-Energy Minima", *Proceedings of the National Academy of Sciences of the United States of America*, 2002, **99**, 12562-12566.
- [189] R. Martonak, A. Laio, M. Parrinello, "Predicting Crystal Structures: The Parrinello-Rahman Method Revisited", *Physical Review Letters*, 2003, **90**, 075503.
- [190] S. Chowdhuri, A. Chandra, "Hydrogen Bonds in Aqueous Electrolyte Solutions: Statistics and Dynamics Based on Both Geometric and Energetic Criteria", *Physical review E, Statistical, nonlinear, and soft matter physics*, 2002, **66**, 041203.
- [191] M.C. Gordillo, J. Marti, "Hydrogen Bond Structure of Liquid Water Confined in Nanotubes", *Chemical Physics Letters*, 2000, **329**, 341-345.
- [192] A. Luzar, D. Chandler, "Hydrogen-Bond Kinetics in Liquid Water", *Nature*, 1996, **379**, 55-57.
- [193] L.-L. Huang, Q. Shao, L.-H. Lu, X.-H. Lu, L.-Z. Zhang, J. Wang, et al., "Helicity and Temperature Effects on Static Properties of Water Molecules Confined in Modified Carbon Nanotubes", *Physical Chemistry Chemical Physics*, 2006, **8**, 3836-3844.

- [194] D. Chen, L. Tang, J. Li, "Graphene-Based Materials in Electrochemistry", *Chemical Society Reviews*, 2010, **39**, 3157-3180.
- [195] F. Cheng, J. Chen, "Metal-Air Batteries: From Oxygen Reduction Electrochemistry to Cathode Catalysts", *Chemical Society Reviews*, 2012, **41**, 2172-2192.
- [196] M. Burghard, H. Klauk, K. Kern, "Carbon-Based Field-Effect Transistors for Nanoelectronics", *Advanced Materials*, 2009, **21**, 2586-2600.
- [197] D. Reddy, L.F. Register, G.D. Carpenter, S.K. Banerjee, "Graphene Field-Effect Transistors", *Journal of Physics D-Applied Physics*, 2011, **44**, 3313001.
- [198] X. Huang, X. Qi, F. Boey, H. Zhang, "Graphene-Based Composites", *Chemical Society Reviews*, 2012, **41**, 666-686.
- [199] X. Zhang, R. Yang, C. Wang, C.-L. Heng, "Cell Biocompatibility of Functionalized Graphene Oxide", *Acta Physico-Chimica Sinica*, 2012, **28**, 1520-1524.
- [200] B.F. Machado, P. Serp, "Graphene-Based Materials for Catalysis", *Catalysis Science & Technology*, 2012, **2**, 54-75.
- [201] G.M. Scheuermann, L. Rumi, P. Steurer, W. Bannwarth, R. Muelhaupt, "Palladium Nanoparticles on Graphite Oxide and Its Functionalized Graphene Derivatives as Highly Active Catalysts for the Suzuki-Miyaura Coupling Reaction", *Journal of the American Chemical Society*, 2009, **131**, 8262-8270.
- [202] H.-P. Jia, D.R. Dreyer, C.W. Bielawski, "Graphite Oxide as an Auto-Tandem Oxidation-Hydration-Aldol Coupling Catalyst", *Advanced Synthesis & Catalysis*, 2011, **353**, 528-532.
- [203] T.J. Bandosz, "Towards Understanding Reactive Adsorption of Small Molecule Toxic Gases on Carbonaceous Materials", *Catalysis Today*, 2012, **186**, 20-28.
- [204] M. Seredych, T.J. Bandosz, "Adsorption of Ammonia on Graphite Oxide/Al-13 Composites", *Colloids and Surfaces a-Physicochemical and Engineering Aspects*, 2010, **353**, 30-36.
- [205] C. Petit, B. Mendoza, T.J. Bandosz, "Hydrogen Sulfide Adsorption on Mofs and Mof/Graphite Oxide Composites", *Chemphyschem*, 2010, **11**, 3678-3684.
- [206] A. Bagri, C. Mattevi, M. Acik, Y.J. Chabal, M. Chhowalla, V.B. Shenoy, "Structural Evolution During the Reduction of Chemically Derived Graphene Oxide", *Nature Chemistry*, 2010, **2**, 581-587.

- [207] Z. Li, W. Zhang, Y. Luo, J. Yang, J.G. Hou, "How Graphene Is Cut Upon Oxidation?", *Journal of the American Chemical Society*, 2009, **131**, 6320-6321.
- [208] S. Fujii, T. Enoki, "Cutting of Oxidized Graphene into Nanosized Pieces", *Journal of the American Chemical Society*, 2010, **132**, 10034-10041.
- [209] W. Cai, R.D. Piner, F.J. Stadermann, S. Park, M.A. Shaibat, Y. Ishii, et al., "Synthesis and Solid-State Nmr Structural Characterization of ¹³C-Labeled Graphite Oxide", *Science*, 2008, **321**, 1815-1817.
- [210] R.Q. Snurr, J.T. Hupp, S.T. Nguyen, "Prospects for Nanoporous Metal-Organic Materials in Advanced Separations Processes", *Aiche Journal*, 2004, **50**, 1090-1095.
- [211] Z. Huang, P.S. White, M. Brookhart, "Ligand Exchanges and Selective Catalytic Hydrogenation in Molecular Single Crystals", *Nature*, 2010, **465**, 598-601.
- [212] Z. Ma, B. Moulton, "Recent Advances of Discrete Coordination Complexes and Coordination Polymers in Drug Delivery", *Coordination Chemistry Reviews*, 2011, **255**, 1623-1641.
- [213] I.D. Williams, S.S.Y. Chui, S.M.F. Lo, J.P.H. Charmant, A.G. Orpen, "A Chemically Functionalizable Nanoporous Material [Cu-3(Tma)(2)(H2o)(3)](N)", *Science*, 1999, **283**, 1148-1150.
- [214] P. Kusgens, M. Rose, I. Senkowska, H. Frode, A. Henschel, S. Siegle, et al., "Characterization of Metal-Organic Frameworks by Water Adsorption", *Microporous and Mesoporous Materials*, 2009, **120**, 325-330.
- [215] L. Grajciar, O. Bludsky, P. Nachtigall, "Water Adsorption on Coordinatively Unsaturated Sites in Cubtc Mof", *Journal of Physical Chemistry Letters*, 2010, **1**, 3354-3359.
- [216] C. Prestipino, L. Regli, J.G. Vitillo, F. Bonino, A. Damin, C. Lamberti, et al., "Local Structure of Framework Cu(I) in Hkust-1 Metallorganic Framework: Spectroscopic Characterization Upon Activation and Interaction with Adsorbates", *Chemistry of Materials*, 2006, **18**, 1337-1346.
- [217] D. Dubbeldam, C.J. Galvin, K.S. Walton, D.E. Ellis, R.Q. Snurr, "Separation and Molecular-Level Segregation of Complex Alkane Mixtures in Metal-Organic Frameworks", *Journal of the American Chemical Society*, 2008, **130**, 10884-10885.
- [218] Y.-S. Bae, K.L. Mulfort, H. Frost, P. Ryan, S. Punnathanam, L.J. Broadbelt, et al., "Separation of Co₂ from CH₄ Using Mixed-Ligand Metal-Organic Frameworks", *Langmuir*, 2008, **24**, 8592-8598.

- [219] R. Babarao, J. Jiang, S.I. Sandler, "Molecular Simulations for Adsorptive Separation of Co(2)/Ch(4) Mixture in Metal-Exposed, Catenated, and Charged Metal-Organic Frameworks", *Langmuir*, 2009, **25**, 5239-5247.
- [220] J.R. Karra, K.S. Walton, "Effect of Open Metal Sites on Adsorption of Polar and Nonpolar Molecules in Metal-Organic Framework Cu-Btc", *Langmuir*, 2008, **24**, 8620-8626.
- [221] J.R. Karra, K.S. Walton, "Molecular Simulations and Experimental Studies of Co(2), Co, and N(2) Adsorption in Metal-Organic Frameworks", *Journal of Physical Chemistry C*, 2010, **114**, 15735-15740.
- [222] N. Lamia, M. Jorge, M.A. Granato, F.A. Almeida Paz, H. Chevreau, A.E. Rodrigues, "Adsorption of Propane, Propylene and Isobutane on a Metal-Organic Framework: Molecular Simulation and Experiment", *Chemical Engineering Science*, 2009, **64**, 3246-3259.
- [223] J.C. Tan, A.K. Cheetham, "Mechanical Properties of Hybrid Inorganic-Organic Framework Materials: Establishing Fundamental Structure-Property Relationships", *Chemical Society Reviews*, 2011, **40**, 1059-1080.
- [224] K.W. Chapman, G.J. Halder, P.J. Chupas, "Pressure-Induced Amorphization and Porosity Modification in a Metal-Organic Framework", *Journal of the American Chemical Society*, 2009, **131**, 17546-17547.
- [225] F.-X. Coudert, A. Boutin, M. Jeffroy, C. Mellot-Draznieks, A.H. Fuchs, "Thermodynamic Methods and Models to Study Flexible Metal-Organic Frameworks", *Chem Phys Chem*, 2011, **12**, 247-258.
- [226] F. Gul-E-Noor, B. Jee, A. Poepl, M. Hartmann, D. Himsl, M. Bertmer, "Effects of Varying Water Adsorption on a Cu(3)(Btc)(2) Metal-Organic Framework (Mof) as Studied by (1)H and (13)C Solid-State Nmr Spectroscopy", *Physical Chemistry Chemical Physics*, 2011, **13**, 7783-7788.
- [227] M.D. Allendorf, R.J.T. Houk, L. Andruszkiewicz, A.A. Talin, J. Pikarsky, A. Choudhury, et al., "Stress-Induced Chemical Detection Using Flexible Metal-Organic Frameworks", *Journal of the American Chemical Society*, 2008, **130**, 14404-14405.
- [228] C. Petit, L.L. Huang, J. Jagiello, J. Kenvin, K.E. Gubbins, T.J. Bandosz, "Toward Understanding Reactive Adsorption of Ammonia on Cu-Mof/Graphite Oxide Nanocomposites", *Langmuir*, 2011, **27**, 13043-13051.
- [229] G.W. Peterson, G.W. Wagner, A. Balboa, J. Mahle, T. Sewell, C.J. Karwacki, "Ammonia Vapor Removal by Cu(3)(Btc)(2) and Its Characterization by Mas Nmr", *Journal of Physical Chemistry C*, 2009, **113**, 13906-13917.

- [230] C. Serre, S. Bourrelly, A. Vimont, N.A. Ramsahye, G. Maurin, P.L. Llewellyn, et al., "An Explanation for the Very Large Breathing Effect of a Metal-Organic Framework During Co₂ Adsorption", *Advanced Materials*, 2007, **19**, 2246-2251.
- [231] D.L. Chen, A.C. Stern, B. Space, J.K. Johnson, "Atomic Charges Derived from Electrostatic Potentials for Molecular and Periodic Systems", *Journal of Physical Chemistry A*, 2010, **114**, 10225-10233.
- [232] T. Watanabe, T.A. Manz, D.S. Sholl, "Accurate Treatment of Electrostatics During Molecular Adsorption in Nanoporous Crystals without Assigning Point Charges to Framework Atoms", *Journal of Physical Chemistry C*, 2011, **115**, 4824-4836.
- [233] S. Amirjalayer, M. Tafipolsky, R. Schmid, "Exploring Network Topologies of Copper Paddle Wheel Based Metal–Organic Frameworks with a First-Principles Derived Force Field", *The Journal of Physical Chemistry C*, 2011, **115**, 15133-15139.
- [234] L. Zhao, Q. Yang, Q. Ma, C. Zhong, J. Mi, D. Liu, "A Force Field for Dynamic Cu-Btc Metal-Organic Framework", *Journal of Molecular Modeling*, 2011, **17**, 227-234.
- [235] O. Rahaman, A.C.T. van Duin, V.S. Bryantsev, J.E. Mueller, S.D. Solares, W.A. Goddard, III, et al., "Development of a Reaxff Reactive Force Field for Aqueous Chloride and Copper Chloride", *Journal of Physical Chemistry A*, 2010, **114**, 3556-3568.
- [236] M.R. Weismiller, A.C.T. van Duin, J. Lee, R.A. Yetter, "Reaxff Reactive Force Field Development and Applications for Molecular Dynamics Simulations of Ammonia Borane Dehydrogenation and Combustion", *Journal of Physical Chemistry A*, 2010, **114**, 5485-5492.
- [237] S.P. Han, A.C.T. van Duin, W.A. Goddard, III, A. Strachan, "Thermal Decomposition of Condensed-Phase Nitromethane from Molecular Dynamics from Reaxff Reactive Dynamics", *Journal of Physical Chemistry B*, 2011, **115**, 6534-6540.
- [238] T.T. Jarvi, A. Kuronen, M. Hakala, K. Nordlund, A.C.T. van Duin, W.A. Goddard, III, et al., "Development of a Reaxff Description for Gold", *European Physical Journal B*, 2008, **66**, 75-79.
- [239] M.R. LaBrosse, J.K. Johnson, A.C.T. van Duin, "Development of a Transferable Reactive Force Field for Cobalt", *Journal of Physical Chemistry A*, 2010, **114**, 5855-5861.
- [240] J.E. Mueller, A.C.T. van Duin, W.A. Goddard, III, "Development and Validation of Reaxff Reactive Force Field for Hydrocarbon Chemistry Catalyzed by Nickel", *Journal of Physical Chemistry C*, 2010, **114**, 4939-4949.
- [241] K. Joshi, A.C.T. van Duin, T. Jacob, "Development of a Reaxff Description of Gold Oxides and Initial Application to Cold Welding of Partially Oxidized Gold Surfaces", *Journal of Materials Chemistry*, 2010, **20**, 10431-10437.

- [242] A.C.T. van Duin, A. Strachan, S. Stewman, Q.S. Zhang, X. Xu, W.A. Goddard, "Reaxff(Sio) Reactive Force Field for Silicon and Silicon Oxide Systems", *Journal of Physical Chemistry A*, 2003, **107**, 3803-3811.
- [243] M.F. Russo, A.C.T. van Duin, "Molecular Dynamics Simulations of Aromatic Hydrocarbon Combustion Via the Reaxff Reactive Force Field", *Abstracts of Papers of the American Chemical Society*, 2010, **240**.
- [244] C. Serre, C. Mellot-Draznieks, S. Surble, N. Audebrand, Y. Filinchuk, G. Ferey, "Role of Solvent-Host Interactions That Lead to Very Large Swelling of Hybrid Frameworks", *Science*, 2007, **315**, 1828-1831.
- [245] O.M. Yaghi, H.L. Li, "Hydrothermal Synthesis of a Metal-Organic Framework Containing Large Rectangular Channels", *Journal of the American Chemical Society*, 1995, **117**, 10401-10402.
- [246] L.J. Murray, M. Dinca, J.R. Long, "Hydrogen Storage in Metal-Organic Frameworks", *Chemical Society Reviews*, 2009, **38**, 1294-1314.
- [247] A.U. Czaja, N. Trukhan, U. Mueller, "Industrial Applications of Metal-Organic Frameworks", *Chemical Society Reviews*, 2009, **38**, 1284-1293.
- [248] G. Ferey, "Hybrid Porous Solids: Past, Present, Future", *Chemical Society Reviews*, 2008, **37**, 191-214.
- [249] S.L. James, "Metal-Organic Frameworks", *Chemical Society Reviews*, 2003, **32**, 276-288.
- [250] H.K. Chae, D.Y. Siberio-Perez, J. Kim, Y. Go, M. Eddaoudi, A.J. Matzger, et al., "A Route to High Surface Area, Porosity and Inclusion of Large Molecules in Crystals", *Nature*, 2004, **427**, 523-527.
- [251] H.-L. Jiang, Q. Xu, "Porous Metal-Organic Frameworks as Platforms for Functional Applications", *Chemical Communications*, 2011, **47**, 3351-3370.
- [252] D. Saha, S. Deng, "Ammonia Adsorption and Its Effects on Framework Stability of Mof-5 and Mof-177", *Journal of Colloid and Interface Science*, 2010, **348**, 615-620.
- [253] T.G. Glover, G.W. Peterson, B.J. Schindler, D. Britt, O. Yaghi, "Mof-74 Building Unit Has a Direct Impact on Toxic Gas Adsorption", *Chemical Engineering Science*, 2011, **66**, 163-170.
- [254] T. Watanabe, D.S. Sholl, "Molecular Chemisorption on Open Metal Sites in Cu(3)(Benzenetricarboxylate)(2): A Spatially Periodic Density Functional Theory Study", *Journal of Chemical Physics*, 2010, **133**, 094509.

- [255] Q. Yang, C. Zhong, "Molecular Simulation of Carbon Dioxide/Methane/Hydrogen Mixture Adsorption in Metal-Organic Frameworks", *Journal of Physical Chemistry B*, 2006, **110**, 17776-17783.
- [256] L. Zhang, J.I. Siepmann, "Development of the Trappe Force Field for Ammonia", *Collection of Czechoslovak Chemical Communications*, 2010, **75**, 577-591.
- [257] C. Petit, J. Burrell, T.J. Bandosz, "The Synthesis and Characterization of Copper-Based Metal-Organic Framework/Graphite Oxide Composites", *Carbon*, 2011, **49**, 563-572.
- [258] A.R. Millward, O.M. Yaghi, "Metal-Organic Frameworks with Exceptionally High Capacity for Storage of Carbon Dioxide at Room Temperature", *Journal of the American Chemical Society*, 2005, **127**, 17998-17999.
- [259] L. Czepirski, J. Jagiello, "Virial-Type Thermal Equation of Gas Solid Adsorption", *Chemical Engineering Science*, 1989, **44**, 797-801.
- [260] F.-X. Coudert, M. Jeffroy, A.H. Fuchs, A. Boutin, C. Mellot-Draznieks, "Thermodynamics of Guest-Induced Structural Transitions in Hybrid Organic-Inorganic Frameworks", *Journal of the American Chemical Society*, 2008, **130**, 14294-14302.
- [261] F.-X. Coudert, A. Boutin, M. Jeffroy, C. Mellot-Draznieks, A.H. Fuchs, "Thermodynamic Methods and Models to Study Flexible Metal-Organic Frameworks", *Chemphyschem*, 2011, **12**, 247-258.
- [262] M. Jeffroy, A.H. Fuchs, A. Boutin, "Structural Changes in Nanoporous Solids Due to Fluid Adsorption: Thermodynamic Analysis and Monte Carlo Simulations", *Chemical Communications*, 2008, 3275-3277.
- [263] F.-X. Coudert, C. Mellot-Draznieks, A.H. Fuchs, A. Boutin, "Prediction of Breathing and Gate-Opening Transitions Upon Binary Mixture Adsorption in Metal-Organic Frameworks", *Journal of the American Chemical Society*, 2009, **131**, 11329-11331.
- [264] O.M. Yaghi, G.M. Li, H.L. Li, "Selective Binding and Removal of Guests in a Microporous Metal-Organic Framework", *Nature*, 1995, **378**, 703-706.
- [265] O.M. Yaghi, M. O'Keeffe, N.W. Ockwig, H.K. Chae, M. Eddaoudi, J. Kim, "Reticular Synthesis and the Design of New Materials", *Nature*, 2003, **423**, 705-714.
- [266] J.L.C. Rowsell, E.C. Spencer, J. Eckert, J.A.K. Howard, O.M. Yaghi, "Gas Adsorption Sites in a Large-Pore Metal-Organic Framework", *Science*, 2005, **309**, 1350-1354.

- [267] M. Ranocchiari, J.A. van Bokhoven, "Catalysis by Metal-Organic Frameworks: Fundamentals and Opportunities", *Physical Chemistry Chemical Physics*, 2011, **13**, 6388-6396.
- [268] A. Phan, A.U. Czaja, F. Gandara, C.B. Knobler, O.M. Yaghi, "Metal-Organic Frameworks of Vanadium as Catalysts for Conversion of Methane to Acetic Acid", *Inorganic Chemistry*, 2011, **50**, 7388-7390.
- [269] D. Farrusseng, S. Aguado, C. Pinel, "Metal-Organic Frameworks: Opportunities for Catalysis", *Angewandte Chemie-International Edition*, 2009, **48**, 7502-7513.
- [270] L.E. Kreno, J.T. Hupp, R.P. Van Duyne, "Metal-Organic Framework Thin Film for Enhanced Localized Surface Plasmon Resonance Gas Sensing", *Analytical Chemistry*, 2010, **82**, 8042-8046.
- [271] B. Liu, C.Y. Sun, G.J. Chen, "Molecular Simulation Studies of Separation of Ch(4)/H(2) Mixture in Metal-Organic Frameworks with Interpenetration and Mixed-Ligand", *Chemical Engineering Science*, 2011, **66**, 3012-3019.
- [272] E. Atci, I. Erucar, S. Keskin, "Adsorption and Transport of Ch(4), Co(2), H(2) Mixtures in a Bio-Mof Material from Molecular Simulations", *Journal of Physical Chemistry C*, 2011, **115**, 6833-6840.
- [273] H.C. Guo, F. Shi, Z.F. Ma, X.Q. Liu, "Molecular Simulation for Adsorption and Separation of Ch(4)/H(2) in Zeolitic Imidazolate Frameworks (Vol 114c, Pg 12158, 2010)", *Journal of Physical Chemistry C*, 2010, **114**, 21891-21891.
- [274] J.J. Gutierrez-Sevillano, A. Caro-Perez, D. Dubbeldam, S. Calero, "Molecular Simulation Investigation into the Performance of Cu-Btc Metal-Organic Frameworks for Carbon Dioxide-Methane Separations", *Physical Chemistry Chemical Physics*, 2011, **13**, 20453-20460.
- [275] M. Schlesinger, S. Schulze, M. Hietschold, M. Mehring, "Evaluation of Synthetic Methods for Microporous Metal-Organic Frameworks Exemplified by the Competitive Formation of [Cu(2)(Btc)(3)(H(2)O)(3)] and [Cu(2)(Btc)(Oh)(H(2)O)]", *Microporous and Mesoporous Materials*, 2010, **132**, 121-127.
- [276] J. Liu, Y. Wang, A.I. Benin, P. Jakubczak, R.R. Willis, M.D. LeVan, "Co(2)/H(2)O Adsorption Equilibrium and Rates on Metal-Organic Frameworks: Hkust-1 and Ni/Dobdc", *Langmuir*, 2010, **26**, 14301-14307.
- [277] A. Martin-Calvo, E. Garcia-Perez, A. Garcia-Sanchez, R. Bueno-Perez, S. Hamad, S. Calero, "Effect of Air Humidity on the Removal of Carbon Tetrachloride from Air Using Cu-Btc Metal-Organic Framework", *Physical Chemistry Chemical Physics*, 2011, **13**, 11165-11174.

[278] C. Petit, B. Mendoza, D. O'Donnell, T.J. Bandoz, "Effect of Graphite Features on the Properties of Metal-Organic Framework/Graphite Hybrid Materials Prepared Using an in Situ Process", *Langmuir*, 2011, **27**, 10234-10242.

APPENDICES

APPENDIX A.

Installing the parallel version of LAMMPS package

We demonstrate the parallel installation of LAMMPS on the Linux OS (x86_64).

Required source codes/packages

- (a) LAMMPS Version July 2, 2012;
- (b) PGI C++/FORTRAN version 12.3;
- (c) FFTW version 2.1.5;
- (d) MPICH2 version 1.4.1p1;

The pre-requisites and the LAMMPS package are installed under the path /lammps.

Installation Steps

(1) Make sure the PGI C++/FORTRAN have been installed and the compiler commands are searchable, for example:

```
$ which pgf90
/opt/pgi/linux86-64/12.3/bin/pgf90
```

(2) Install FFTW for the fast Fourier transform computation:

Download FFTW from the website <http://www.fftw.org/download.html>, and save the source code to /lammps

```
$ cd /lammps
$ tar -zxvf fftw-2.1.5.tar.gz
$ cd fftw-2.1.5
$ ./configure --enable-float --prefix=/lammps/fftw215
$ make
$ make install
$ make distclean
$ ./configure --prefix=/lammps/fftw215
$ make
$ make install
```

(3) Install MPICH2 for the parallel communications.

3.1. Download mpich2-1.4.1p1.tar.gz, and save the source code to /lammps.

<http://www.mcs.anl.gov/research/projects/mpich2/downloads/index.php?s=downloads>

```
$ cd /lammps
$ tar zxvf mpich2-1.4.1p1.tar.gz
$ mkdir mpich
$ cd mpich2-1.4.1p1
$ ./configure CC=pgcc CXX=pgCC F70=pgf70 FC=pgf90 --prefix=/lammps/mpich
$ make
$ make install
```

3.2. Add the commands to the search path. If bash is the default shell, this can be done by editing the “.bash_profile” under the home directory:

```
$ vi ~/.bash_profile
```

Add the two lines below:

```
PATH=/lammps/mpich/bin:$PATH
export PATH
```

Save and make the changes effective:

```
$ . ~/.bash_profile
```

Check to see if the executable is searchable:

```
$ which mpif90
```

```
/lammps/mpich/bin/mpif90
```

(4) Install the parallel version of LAMMPS with ReaxFF library.

4.1. Download the latest version from: <http://lammps.sandia.gov/download.html>, and save to /lammps

```
$ cd /lammps
$ tar zxvf lammps.tar.gz
$ cd lammps-2Jul12
```

4.2. Compile the REAX library

```
$ cd lib/reax
$ make -f Makefile.pgf90
$ vi Makefile.lammps
```

Change the “Makefile.lammps” file, so the contains look like:

```
reax_SYSINC =
reax_SYSLIB = -lpgf90 -lpgf90rtl -lpghpf_mpi -lpghpf2
reax_SYSPATH =
```

4.3. Change the makefile “Makefile.pgi” at /lammps/lammps-2Jul12/src/MAKE

```
$ cd /lammps/lammps-2Jul12/src/MAKE
$ vi Makefile.pgi
```

The changes are mainly to specify the compiler options and the path to the libraries files:

```
# pgi = Portland Group compiler, pgCC, MPICH, FFTW
SHELL = /bin/sh
# Compiler/linker settings
# Specify flags and libraries needed for your compiler
CC =      mpicxx
CCFLAGS = -fast
DEPFLAGS = -M
LINK =    mpicxx
LINKFLAGS =
LIB =     -pthread -lpgf90 -lpghpf_mpi -lpghpf2 -lpgf90rtl -lpgftnrtl
ARCHIVE = ar
ARFLAGS = -rc
SIZE =    size

# LAMMPS-specific settings
LMP_INC = -DLAMMPS_GZIP

# MPI library, REQUIRED
# INC = path for mpi.h, MPI compiler settings
# PATH = path for MPI library
# LIB = name of MPI library
MPI_INC = -I/home/qphll/mpich/include
MPI_PATH = -L/home/qphll/mpich/lib
MPI_LIB = -lmpich

# FFT library, OPTIONAL
# INC = -DFFT setting, e.g. -DFFT_FFTW, FFT compiler settings
# PATH = path for FFT library
# LIB = name of FFT library
```

```
FFT_INC = -DFFT_FFTW -I/lammps/fftw215/include
FFT_PATH = -L/lammps/fftw215/lib
FFT_LIB = -lfftw
```

4.4. Define the packages to be installed:

```
$ cd /lammps/lammps-2Jul12/src
$ make yes-all
$ make no-gpu
$ make no-kim
$ make no-user-atc
$ make no-user-awpmd
$ make no-user-cuda
$ make no-meam
$ make no-poems
```

You may check the installed package/library using the command below:

```
$ make package-status
```

4.5. Now, the final step is:

```
$ make pgi
```

You should receive the parallel executable named “`lmp_pgi`” at the end of the process.

APPENDIX B.

An example of the temperature-programmed RMD by LAMMPS

The control file used in the temperature-programmed RMD in Chapter 5 is provided. We also give a list of ReaxFF parameters used in the graphene oxide calculations.

B.1. Control file, “in.reaxff”

```
## Initialization
units          real
dimension      3
boundary       p p p
atom_style     charge
## Atom definition
read_data      initial.dat
## ReaxFF, 1-C, 2-H, 3-O, 4-N, 5-S
pair_style     reax
pair_coeff     * *ffield.reax 1 2 3
## Settings
mass 1 12.0107
mass 2 1.00794
mass 3 15.9994
neighbor2.5 bin
neigh_modify   delay 0 every 2 check yes
# Timestep, unit: fs
timestep 0.25

compute reax all pair reax
variable eb    equal c_reax[1]
variable ea    equal c_reax[2]
variable elp   equal c_reax[3]
variable emol  equal c_reax[4]
variable ev    equal c_reax[5]
variable epen  equal c_reax[6]
variable ecoa  equal c_reax[7]
variable ehb   equal c_reax[8]
variable et    equal c_reax[9]
variable eco   equal c_reax[10]
variable ew    equal c_reax[11]
variable ep    equal c_reax[12]
variable efi   equal c_reax[13]
variable eqeq  equal c_reax[14]
## Output frequency
thermo        10
thermo_style  custom step cpu press vol temp etotal pe ke v_eb v_ea v_elp v_emol v_ev v_epen v_ecoa v_ehb
```

```
v_et v_eco v_ew v_ep v_efi v_eqeq
thermo_modify line one
restart 1000 restart.*
### Simulation-1: NVT, 10K, 25 ps.
## XYZ
dump 1 all xyz 1000 10.structure.*.xyz
dump_modify 1 sort id
```

```
## This is to set initial velocities at 10.0K, according to Maxwell-Boltzmann distribution.
velocity all create 10.0 493243 dist gaussian
fix 1 all nvt temp 10.0 10.0 100.0
fix 2 all reax/bonds 10 10.bonds.connect
run 100000
undump 1
unfix 1
unfix 2
```

```
### Simulation-2: NVT, 10 K - 2010K, 0.005 K/iteration
# XYZ
dump 21 all xyz 1000 10-2010.structure.*.xyz
dump_modify 21 sort id
fix 21 all nvt temp 10.0 2010.0 100.0
fix 22 all reax/bonds 10 10-2010.bonds.connect
run 400000
undump 21
unfix 21
unfix 22
```

```
### Simulation-3: NVT, 2010 K, 25 ps
## XYZ
dump 31 all xyz 1000 2010.structure.*.xyz
dump_modify 31 sort id
fix 31 all nvt temp 2010.0 2010.0 100.0
fix 32 all reax/bonds 10 2010.bonds.connect
run 100000
undump 31
unfix 31
unfix 32
```

```
### Simulation-4: NVT, 2010 K – 10 K, 0.005 K/iteration
## XYZ
dump 41 all xyz 1000 2010-10.structure.*.xyz
dump_modify 41 sort id
fix 41 all nvt temp 2010.0 10.0 100.0
fix 42 all reax/bonds 10 2010-10.bonds.connect
run 500000
undump 41
unfix 41
unfix 42
```

```

### Simulation-4: NVT, 2010 K – 300 K, 0.005 K/iteration
## XYZ
dump 41 all xyz 1000 2010-300.structure.*.xyz
dump_modify 41 sort id
fix 41 all nvt temp 2010.0 300.0 100.0
fix 42 all reax/bonds 10 2010-300.bonds.connect
run 342000
undump 41
unfix 41
unfix 42
### Simulation-5: NVT, 300 K, 25 ps.
## XYZ
dump 51 all xyz 1000 300.structure.*.xyz
dump_modify 51 sort id
fix 51 all nvt temp 300.0 300.0 100.0
fix 52 all reax/bonds 10 300.bonds.connect
run 100000
undump 51
unfix 51
unfix 52

```

B.2. A list of ReaxFF parameter explanations

The complete list of ReaxFF potential functions can be found elsewhere.[\[51\]](#)

Table A-1. The parameters in the bond order functions.

$P_{bo1} \sim P_{bo6}$	Bond parameters
$r_0^\sigma, r_0^\pi, r_0^{\pi\pi}$	Bond radius parameters
Val_i, Val_i^{boc}	Valences of atom i
P_{boc1}, P_{boc2}	Overcoordination parameters
$P_{boc3} \sim P_{boc5}$	1-3 bond order corrections

Table A-2. The parameters in the 1-body energy.

Val_i^e	Valence of atom i
$n_{lp-opt,i}$	The number of lone pair electrons at normal condition
P_{lp1}	Lone pair parameter
P_{lp2}	Lone pair energy parameter
$P_{ovun1} \sim P_{ovun4}$	Overcoordination parameters
P_{ovun5}	Undercoordination energy parameter
$P_{ovun6} \sim P_{ovun8}$	Undercoordination parameters

Table A-3. The parameters in the E_{bond} .

$D_e^\sigma, D_e^\pi, D_e^{\pi\pi}$	σ, π , and double π bond energy parameters
P_{be1}, P_{be2}	Bonding energy parameters

Table A-4 The parameters in the 3-body energy.

P_{val1}	Valence angle energy parameter
$P_{val2} \sim P_{val7}, P_{val9}, P_{val10}$	Valence angle parameters
P_{val8}	Valence lone pair parameter
$\Theta_{0,0}$	Equilibrium valence angle
Val_i^{angle}	Atom valence
P_{pen1}	Penalty energy parameter
P_{pen2}	Double bond/angle parameter
P_{pen3}, P_{pen4}	Double bond/angle parameter for overcoordination
P_{coa1}	3-body conjugation energy parameter
$P_{coa2} \sim P_{coa4}$	Valence angle conjugation parameters

Table A5. The parameters in the 4-body energy.

$V_1 \sim V_3$	Torsion energy parameters
P_{tor1}	Torsion parameter
P_{tor2}	Torsion bond order parameter
P_{tor3}, P_{tor4}	Torsion overcoordination parameters
P_{cot1}	4-body conjugation energy parameter
P_{cot2}	4-body conjugation parameter

Table A-6. The parameters in the hydrogen bonding energy.

P_{hb1}	Hydrogen bond energy parameter
P_{hb2}, P_{hb3}	Hydrogen bond parameters
r_{hb}^0	Hydrogen bond radius

Table A-7. The parameters in the non-covalent energy.

D_{ij}	van der Waals energy parameter
$\alpha_{ij}, r_{vdW}, \gamma_w$	van der Waals parameters
P_{vdw1}	van der Waals shielding
γ_{ij}	Coulomb parameter

B.3. ReaxFF parameters for C, H and O elements of graphene oxide.

The general parameters are denoted by the superscript †. The parameters that are not used in the calculation are left blank.

Table A-8. EEM parameters.

	$\chi(eV)$	$\eta(eV)$	$\gamma(\text{\AA}^{-1})$
C	5.8678	7.0000	0.900
H	5.3200	7.4366	1.0206
O	8.5000	8.9989	1.0503

Table A-9. Bond order parameters.

	p_{bo1}	p_{bo2}	p_{bo3}	p_{bo4}	p_{bo5}	p_{bo6}	$r_0^\sigma(\text{\AA})$	$r_0^\pi(\text{\AA})$	$r_0^{\pi\pi}(\text{\AA})$
C-C	6.8316	1.0	9.2605	0.0	-0.4591	0.4235	1.3825	1.1359	1.2104
H-H	4.0758	0.0	0.0000	0.0	0.0000	1.0000	0.7842	-0.1000	-0.1000
O-O	6.2919	1.0	7.6487	1.0	-0.1244	0.9114	1.2477	0.9088	1.0863
C-H	6.8315	0.0	0.0000	0.0	0.0000	0.7140			
C-O	5.2913	0.0	7.0303	1.0	-0.1613	1.0000			
O-H	5.0451	0.0	0.0000	0.0	0.0000	0.5514			

Table A-10. Bond order correction parameters.

	Val_i	Val_i^{boc}	P_{boc1}^\dagger	P_{boc2}^\dagger	P_{boc3}	P_{boc4}	P_{boc5}
C	4.0000	4.0000	50.0000	9.5469	34.7289	8.6991	13.3894
H	1.0000	1.0000	50.0000	9.5469	3.3517	1.9771	0.7571
O	2.0000	4.0000	50.0000	9.5469	3.3754	20.4140	0.2702

Table A-11. Bond energy parameters.

	D_e^σ (kcal / mol)	D_e^π (kcal / mol)	$D_e^{\pi\pi}$ (kcal / mol)	P_{be1}	P_{be2}
C-C	156.5953	100.0397	80.0000	-0.8157	-0.1000
H-H	145.0803	0.0000	0.0000	-0.4173	1.0000
O-O	60.1463	176.6202	51.1430	-0.2802	-0.1239
C-H	170.2316	0.0000	0.0000	-0.5931	1.0000
C-O	160.4802	105.1693	23.3059	-0.3873	-0.3174
H-O	180.4373	0.0000	0.0000	-0.8074	1.0000

Table A-12. Lone pair energy parameters.

	Val_i^e	P_{lp1}^\dagger	p_{lp2} (kcal / mol)
C	4.0000	6.0891	0.0000
H	1.0000	6.0891	0.0000
O	6.0000	6.0891	1.0003

Table A-13. Overcoordination parameters.

	Val_i	P_{ovun1}	P_{ovun2}	P_{ovun3}^\dagger	P_{ovun4}^\dagger
C-C	4.0000	0.4527	-2.8983	50.0000	0.6991
H-H	1.0000	5.2125	-15.7683	50.0000	0.6991
O-O	2.0000	0.2441	-3.6141	50.0000	0.6991
C-H		5.2267		50.0000	0.6991
C-O		0.5341		50.0000	0.6991
H-O		1.2490		50.0000	0.6991

Table A-14. Undercoordination parameters.

	P_{ovun2}	P_{ovun5}	P_{ovun6}^\dagger	P_{ovun7}^\dagger	P_{ovun8}^\dagger
C-C	-2.8983	33.2433	1.0588	12.1176	13.3056
H-H	-15.7683	0.0000	1.0588	12.1176	13.3056
O-O	-3.6141	36.9573	1.0588	12.1176	13.3056
C-H			1.0588	12.1176	13.3056
C-O			1.0588	12.1176	13.3056
H-O			1.0588	12.1176	13.3056

Table A-15. Valence angle parameters, part I.

	P_{val1}	P_{val2}	P_{val3}	P_{val4}	P_{val5}	P_{val6}
C			2.5000		2.9663	
H			2.1488		2.8793	
O			2.7025		2.9225	
C-C-C	22.0695	1.6286		1.8089		
C-C-H	14.3185	6.2977		1.1530		
H-C-H	25.3540	3.4508		3.0000		
C-H-H	0.0000	6.0000		1.0400		
C-H-C	3.4110	7.7350		1.0400		
H-H-H	27.9213	5.8635		1.0400		
C-C-O	7.3771	4.9568		1.0010		
O-C-O	39.8746	2.5403		2.1240		
H-C-O	14.2057	4.8649		1.7185		
C-O-C	44.7500	0.7952		1.0528		
C-O-O	36.6201	2.0201		3.0000		
O-O-O	30.4554	0.9953		1.0783		
C-O-H	21.7062	0.4735		1.1793		
H-O-O	23.3540	1.5057		1.3023		
H-O-H	10.4737	1.2895		1.1043		
C-H-O	25.0000	3.0000		1.0400		
O-H-O	0.0148	6.0000		1.0400		
H-H-O	9.7025	6.0000		1.0400		

Table A-16. Valence angle parameters, part II.

	P_{val7}^\dagger	P_{val8}^\dagger	P_{val9}^\dagger	P_{val10}^\dagger	Val^{angle}	$\Theta_{0,0}$
C	33.8667	1.8512	1.0563	2.0384	4.0000	
H	33.8667	1.8512	1.0563	2.0384	1.0000	
O	33.8667	1.8512	1.0563	2.0384	4.0000	
C-C-C	33.8667	1.8512	1.0563	2.0384		67.2326
C-C-H	33.8667	1.8512	1.0563	2.0384		65.2527
H-C-H	33.8667	1.8512	1.0563	2.0384		70.0840
C-H-H	33.8667	1.8512	1.0563	2.0384		0.0000
C-H-C	33.8667	1.8512	1.0563	2.0384		0.0000
H-H-H	33.8667	1.8512	1.0563	2.0384		0.0000
C-C-O	33.8667	1.8512	1.0563	2.0384		49.5561
O-C-O	33.8667	1.8512	1.0563	2.0384		77.1171
H-C-O	33.8667	1.8512	1.0563	2.0384		65.0000
C-O-C	33.8667	1.8512	1.0563	2.0384		74.3994
C-O-O	33.8667	1.8512	1.0563	2.0384		77.9854
O-O-O	33.8667	1.8512	1.0563	2.0384		80.7324
C-O-H	33.8667	1.8512	1.0563	2.0384		71.5018
H-O-O	33.8667	1.8512	1.0563	2.0384		84.9468
H-O-H	33.8667	1.8512	1.0563	2.0384		77.0645
C-H-O	33.8667	1.8512	1.0563	2.0384		0.0000
O-H-O	33.8667	1.8512	1.0563	2.0384		0.0000
H-H-O	33.8667	1.8512	1.0563	2.0384		0.0000

Table A-17. Penalty energy and 3-body conjugation parameters.

	P_{pen1}	P_{pen2}	P_{pen3}^\dagger	P_{pen4}^\dagger	P_{coa1}	P_{coa2}^\dagger	P_{coa3}^\dagger	P_{coa4}^\dagger
C-C-C	15.4141	6.929	0.3889	3.9954	0.0000	26.5405	2.6962	2.1365
C-C-H	0.0000	6.929	0.3889	3.9954	0.0000	26.5405	2.6962	2.1365
H-C-H	0.0000	6.929	0.3889	3.9954	0.0000	26.5405	2.6962	2.1365
C-H-H	0.0000	6.929	0.3889	3.9954	0.0000	26.5405	2.6962	2.1365
C-H-C	0.0000	6.929	0.3889	3.9954	0.0000	26.5405	2.6962	2.1365
H-H-H	0.0000	6.929	0.3889	3.9954	0.0000	26.5405	2.6962	2.1365
C-C-O	15.9906	6.929	0.3889	3.9954	0.0000	26.5405	2.6962	2.1365
O-C-O	-42.9758	6.929	0.3889	3.9954	-24.3902	26.5405	2.6962	2.1365
H-C-O	0.0000	6.929	0.3889	3.9954	0.0000	26.5405	2.6962	2.1365
C-O-C	0.0000	6.929	0.3889	3.9954	0.0000	26.5405	2.6962	2.1365
C-O-O	67.0264	6.929	0.3889	3.9954	0.0000	26.5405	2.6962	2.1365
O-O-O	50.0000	6.929	0.3889	3.9954	0.0000	26.5405	2.6962	2.1365
C-O-H	0.0000	6.929	0.3889	3.9954	0.0000	26.5405	2.6962	2.1365
H-O-O	0.0000	6.929	0.3889	3.9954	0.0000	26.5405	2.6962	2.1365
H-O-H	0.0000	6.929	0.3889	3.9954	0.0000	26.5405	2.6962	2.1365
C-H-O	0.0000	6.929	0.3889	3.9954	0.0000	26.5405	2.6962	2.1365
O-H-O	0.0000	6.929	0.3889	3.9954	0.0000	26.5405	2.6962	2.1365
H-H-O	0.0000	6.929	0.3889	3.9954	0.0000	26.5405	2.6962	2.1365

Table A-18. Torsion angle and 4-body conjugation parameters, part I.

	P_{tor1}	P_{tor2}^\dagger	P_{tor3}^\dagger	P_{tor3}^\dagger	V_1	V_2	V_3	P_{cot1}	P_{cot2}^\dagger
C-C-C-C	-4.7057	5.7796	10.0	1.9487	-0.2500	11.5822	0.1879	-2.2047	2.1645
C-C-C-H	-4.6391	5.7796	10.0	1.9487	-0.2500	31.2596	0.1709	-1.9002	2.1645
H-C-C-H	-5.0019	5.7796	10.0	1.9487	-0.1770	30.0252	0.4340	-2.0697	2.1645
C-C-C-O	-2.5000	5.7796	10.0	1.9487	-0.7098	22.2951	0.0060	-2.1688	2.1645
H-C-C-O	-4.0088	5.7796	10.0	1.9487	-0.3568	22.6472	0.6045	-1.0000	2.1645
O-C-C-O	-5.0913	5.7796	10.0	1.9487	-0.0528	6.8150	0.7498	-1.0000	2.1645
C-C-O-C	-2.6465	5.7796	10.0	1.9487	2.0007	25.5641	-0.0608	-1.1766	2.1645
C-C-O-H	-8.0821	5.7796	10.0	1.9487	-1.1953	42.1545	-1.0000	-1.0000	2.1645
H-C-O-C	-2.5440	5.7796	10.0	1.9487	-0.9284	34.3952	0.7285	-2.4641	2.1645
H-C-O-H	-3.5697	5.7796	10.0	1.9487	-2.5000	79.6980	1.0000	-2.7501	2.1645
C-C-O-O	-2.5000	5.7796	10.0	1.9487	-0.0179	5.0603	-0.1894	-2.0399	2.1645
H-C-O-O	-4.4000	5.7796	10.0	1.9487	-0.5583	80.0000	1.0000	-3.0000	2.1645
O-C-O-C	-3.7586	5.7796	10.0	1.9487	-2.5000	76.0427	-0.0141	-2.9000	2.1645

Table A-19. Torsion angle and 4-body conjugation parameters, part II.

	P_{tor1}	P_{tor2}^\dagger	P_{tor3}^\dagger	P_{tor3}^\dagger	V_1	V_2	V_3	P_{cot1}	P_{cot2}^\dagger
O-C-O-H	-4.1777	5.7796	10.0	1.9487	0.0345	78.9568	-0.6810	-3.0000	2.1645
O-C-O-O	-3.0293	5.7796	10.0	1.9487	-2.5000	66.3525	0.3986	-3.0000	2.1645
C-O-O-C	-3.5096	5.7796	10.0	1.9487	2.5000	-0.5332	1.0000	-2.9000	2.1645
C-O-O-H	-5.2021	5.7796	10.0	1.9487	-2.5000	3.3219	0.7180	-2.9330	2.1645
H-O-O-H	-2.6189	5.7796	10.0	1.9487	2.2500	-6.2288	1.0000	-1.0000	2.1645
C-O-O-O	-2.5000	5.7796	10.0	1.9487	0.0531	-17.3983	1.0000	-2.1584	2.1645
H-O-O-O	-2.5000	5.7796	10.0	1.9487	0.4723	-12.4144	-1.0000	-1.0000	2.1645
O-O-O-O	-2.5000	5.7796	10.0	1.9487	-2.5000	-25.0000	1.0000	-1.0000	2.1645

Table A-20. van der Waals interaction parameters.

	D_{ij}	r_{vdW}	α_{ij}	P_{vdW1}^\dagger	γ_w
C	0.1853	1.9133	9.7602	1.5591	2.1346
H	0.0420	1.4029	9.2018	1.5591	5.0518
O	0.0904	1.9236	10.2127	1.5591	7.7719

Table A-21. Coulomb interaction parameters.

	γ_{ij}
C	0.9000
H	1.0503
O	1.0206

Table A-22. Hydrogen bond parameters.

	r_{hb}^0	P_{hb1}	P_{hb2}	P_{hb3}
O-H-O	1.962	-4.4628	1.7976	3.0000

Table A-23. Taper correction parameters.

$r_c (\text{\AA})$	Tap_0	Tap_1	Tap_2	Tap_3	Tap_4	Tap_5	Tap_6	Tap_7
10.0	1.0	0.0	0.0	0.0	$-\frac{35.0}{r_c^4}$	$\frac{84.0}{r_c^5}$	$-\frac{72.0}{r_c^6}$	$\frac{20.0}{r_c^7}$